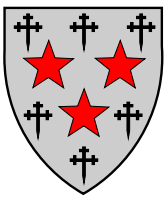
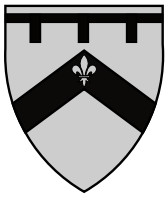
Measurement of Charmed Hadron Production in $e^{\pm}p$ Deep Inelastic Scattering with the ZEUS Detector

Philip Daniel Allfrey
Somerville College, Oxford







Thesis submitted in partial fulfilment of the requirements for the degree of Doctor of Philosophy at the University of Oxford

Trinity Term, 2007

Measurement of Charmed Hadron Production in $e^{\pm}p$ Deep Inelastic Scattering with the ZEUS Detector

Philip Daniel Allfrey
Somerville College, Oxford

Thesis submitted in partial fulfilment of the requirements for the degree of Doctor of Philosophy at the University of Oxford

Trinity Term, 2007

Abstract

Charmed hadron production has been studied in $225\,\mathrm{pb}^{-1}$ of data collected with the ZEUS detector in the HERA-II running period. Studies were made in the $D^* \to D^0\pi \to K\pi\pi$ decay channel to determine the potential for the microvertex detector to improve charm signals. Integrated cross sections were measured for the decays $D^0 \to K^0_s\pi^+\pi^-$, $D^{\pm} \to K^0_s\pi^{\pm}$, $D^{\pm}_s \to K^0_s K^{\pm}$ and $\Lambda^{\pm}_c \to \Lambda^0\pi^{\pm}$ in the kinematic region $5 < Q^2 < 1000\,\mathrm{GeV}^2$, $0.02 < y < 0.7$, $1.5 < p_T(D, \Lambda_c) < 20.0\,\mathrm{GeV}$, $|\eta(D, \Lambda_c)| < 1.6$. The D^0 cross section was additionally measured down to $p_T(D^0) > 1.0\,\mathrm{GeV}$. Differential cross sections as a function of Q^2, x, $p_T(D)$ and $\eta(D)$ were measured for the D^0, $D^{\pm}$, and $D^{\pm}_s$ channels. The measurements were compared to next-to-leading-order (NLO) QCD calculations, and good agreement found for all variables in all channels over the measured kinematic region. The strangeness-suppression factor, $\gamma_s = D^{\pm}_s/(D^{\pm} + D^0)$, was measured and found to be in good agreement with values previously measured at HERA and elsewhere, and with the DJANGOH and RAPGAP Monte Carlo. The ratio of the number of charmed baryons to mesons, $\Lambda^{\pm}_c/(D^{\pm} + D^0)$, was measured and also found to be in good agreement with Monte Carlo.

Acknowledgements

I would like to begin by thanking my supervisor, Roman Walczak, for his guidance and support which have been invaluable over the last four years. Thanks must also go to the other Oxford academics and post-docs who have helped me with my analysis, namely Robin, Bruce, Grzegorz, Claire and most recently James. The coordinators and members, past and present, of the ZEUS Heavy Flavours group have also provided useful input. My fellow students in the Oxford ZEUS group have also contributed to this thesis, both in terms of assistance with the day-to-day details of the analysis, and in providing a convivial atmosphere both inside and outside the office, so thank you Mark, Andrew, Sunil, Katherine, Aileen and Katie.

My stay in Hamburg was enlivened by the company of other UK students in my year, Catherine, Billy, John and Paul (all of whom have now completed their own doctorates), and the rest of the ZEUS UK group. My thanks must also go to Susan Ketels for her assistance with arranging accommodation and for helping with all the paperwork involved in moving to Germany. Thanks are also due to my many friends in Somerville College for enriching my life 'outside physics'.

As with any large collaboration the ZEUS experiment is only possible through the efforts of many hundreds of people in designing, building and running the detector and analysing the data, all of whom should be acknowledged. The efforts of the HERA machine group in operating the accelerator should also be acknowledged.

My financial support has been provided by a Commonwealth Scholarship, awarded jointly by the Commonwealth Scholarship Commission and the University of Oxford, and administered by the Association of Commonwealth Universities and the British Council. Without this support I would not have been able to study at Oxford. I would also like to acknowledge financial support from the Sub-Department of Particle Physics for travel to, and part of my stay in, Hamburg, as well as attendance at various summer schools.

Finally I would like to thank my family, Mum, Dad, Kristina and Richard, Emma, and Jonathan, (whom I mention by name since there were complaints after I failed to do so in my last thesis!) for their love and support, despite being halfway round the world.

Contents

1 Introduction **1**
1.1 Introduction . . . 1
1.2 Outline . . . 3

2 HERA and ZEUS **5**
2.1 HERA . . . 5
2.1.1 HERA Injection System . . . 6
2.1.2 HERA-I Operation . . . 7
2.1.3 HERA Upgrade . . . 8
2.1.4 Background Problems . . . 9
2.1.5 HERA-II Operation . . . 13
2.2 ZEUS . . . 14
2.2.1 CTD . . . 16
2.2.2 MVD . . . 19
2.2.3 Calorimeter . . . 21
2.2.4 Luminosity Monitor . . . 25
2.2.5 Trigger and Data Acquisition . . . 26

3 Electron–Proton Collisions and QCD **29**
3.1 Electron–Proton Scattering . . . 29
3.2 Kinematics . . . 29
3.3 Cross Sections and Structure Functions . . . 32
3.4 Quark Parton Model . . . 33
3.5 Photoproduction . . . 37

4 Heavy Quark Production **38**
4.1 Production Mechanisms . . . 38
4.2 QCD Evolution . . . 39
4.3 Charm Structure Function . . . 40
4.4 Fragmentation . . . 41

5 Monte Carlo and Theoretical Predictions **44**
5.1 Monte Carlo . . . 45
5.1.1 Inclusive DIS Monte Carlo . . . 46
5.1.2 Charm Monte Carlo . . . 47
5.2 HVQDIS . . . 47

6 Event Reconstruction **48**
6.1 Kinematic Variables . . . 48
6.1.1 Electron Method . . . 48
6.1.2 Jacquet–Blondel Method . . . 49
6.1.3 Double-Angle Method . . . 49
6.2 Electron Finding . . . 50
6.3 Track and Vertex Reconstruction . . . 51
6.3.1 Track Reconstruction . . . 51
6.3.2 Vertex Reconstruction . . . 52

7 $D^{*\pm} \to D^0\pi^\pm$ Studies **55**
7.1 D^* Reconstruction . . . 55
7.2 Secondary Vertex . . . 57
7.3 Decay Length Cut . . . 60

8 $D^0 \to K^0_s\pi^+\pi^-$ Decay Channel **62**
8.1 Motivation . . . 62
8.2 Trigger Selection . . . 63
8.3 Event Selection . . . 66
8.4 K^0_s Reconstruction . . . 67
8.5 D^0 Reconstruction . . . 71
8.6 Cross Section Unfolding . . . 73
8.7 Integrated Cross Section . . . 75
8.8 Systematic Errors . . . 78
8.8.1 Experimental Systematics . . . 78
8.8.2 Theoretical Systematics . . . 79
8.9 Differential Cross Sections . . . 81

9 $D^\pm \to K^0_s\pi^\pm$ and $D^\pm_s \to K^0_s K^\pm$ Decay Channels **85**
9.1 Introduction . . . 85
9.2 Charmed Hadron Reconstruction . . . 87
9.3 Discriminant Method . . . 88
9.4 Integrated Cross Sections . . . 93
9.5 Systematic Errors . . . 95
9.6 Differential Cross Sections . . . 96
9.7 Strangeness-Suppression Factor . . . 105

10 $\Lambda_c \to \Lambda^0\pi$ Decay Channel **109**
10.1 Introduction . . . 109
10.2 $\Lambda^\pm_c$ Reconstruction . . . 110
10.3 Integrated Cross Section . . . 111
10.3.1 Fit to Mass Distribution . . . 113
10.3.2 Wrong-Charge Background . . . 115
10.4 Systematic Errors . . . 116
10.5 Baryon-to-Meson Ratio . . . 117

11 Conclusions and Outlook **120**
11.1 Conclusions . . . 120
11.2 Future Work . . . 123

A Additional Plots **126**
A.1 D^0 Systematics Plots 126
A.2 $D \to K^0_s X$ Acceptance Plots 129
A.3 $D \to K^0_s X$ Systematics Plots 134

References **139**

List of Figures

2.1 HERA injection system 7
2.2 Spin rotator 9
2.3 HERA luminosity 14
2.4 The ZEUS detector 15
2.5 ZEUS coordinate system 16
2.6 CTD superlayer structure 17
2.7 CTD cell structure 18
2.8 MVD layout 20
2.9 MVD modules 21
2.10 MVD wheel 22
2.11 ZEUS Calorimeter 22
2.12 ZEUS Calorimeter tower 23
2.13 ZEUS Calorimeter module 24
2.14 Luminosity detectors 25
2.15 ZEUS three-level trigger 28

3.1 NC and CC DIS 30
3.2 DIS kinematics 34
3.3 F_2 measurements 36

4.1 Charm production mechanisms 39
4.2 Peterson fragmentation function 42
4.3 Peterson fragmentation parameter measurement 43

5.1 Elements of a Monte Carlo simulation 45

6.1 Comparison of vertexing algorithms 53
6.2 Weight function for DAF algorithm 54

7.1 D^* mass difference 57
7.2 D^0 decay length 60
7.3 D^* mass distribution with decay length cut 61

8.1 DIS control plots 68
8.2 K^0_s mass peak 71
8.3 D^0 mass peak 74
8.4 D^0 acceptances vs Q^2 75
8.5 D^0 acceptances vs x 76
8.6 D^0 acceptances vs p_T 76
8.7 D^0 acceptances vs η 77

8.8 D^0 systematics . . . 79
8.9 D^0 theoretical systematics . . . 82
8.10 D^0 differential cross sections . . . 83

9.1 Signal and background distributions for discriminant method . . . 90
9.2 Background distributions for discriminant method . . . 91
9.3 Discriminant distributions . . . 92
9.4 $K^0_s X$ mass peaks . . . 94
9.5 D^+ systematic errors . . . 98
9.6 D_s systematic errors . . . 98
9.7 D^+ theoretical systematics . . . 99
9.8 D_s theoretical systematics . . . 99
9.9 $\mathrm{d}\sigma(D^+)/\mathrm{d}p_T(D^+)$ compared to results from $D^+ \to K\pi\pi$ . . . 100
9.10 D^+ differential cross sections . . . 101
9.11 D_s differential cross sections . . . 102
9.12 γ_s systematics . . . 107

10.1 Λ^0 mass peak . . . 111
10.2 Λ_c discriminant distribution . . . 112
10.3 Λ_c mass peak . . . 113
10.4 Mass distribution for $\Lambda\pi$, $\Sigma\pi$ and $\Lambda\pi\pi^0$ decays . . . 115
10.5 Mass distribution for $\Lambda\pi$ with a fit to the $\Sigma\pi$ peak . . . 116
10.6 $\Lambda_c^\pm$ systematic errors . . . 117
10.7 $\Lambda_c^\pm$ systematic errors . . . 119

11.1 Comparison of signal-to-background ratios . . . 122

A.1 D^0 systematics for Q^2 bins . . . 127
A.2 D^0 systematics for x bins . . . 127
A.3 D^0 systematics for $p_T(D^0)$ bins . . . 128
A.4 D^0 systematics for $\eta(D^0)$ bins . . . 128
A.5 D^+ acceptances vs Q^2 . . . 130
A.6 D^+ acceptances vs x . . . 130
A.7 D^+ acceptances vs p_T . . . 131
A.8 D^+ acceptances vs η . . . 131
A.9 D_s acceptances vs Q^2 . . . 132
A.10 D_s acceptances vs x . . . 132
A.11 D_s acceptances vs p_T . . . 133
A.12 D_s acceptances vs η . . . 133
A.13 D^+ systematics for Q^2 bins . . . 135
A.14 D^+ systematics for x bins . . . 135
A.15 D^+ systematics for $p_T(D^+)$ bins . . . 136
A.16 D^+ systematics for $\eta(D^+)$ bins . . . 136
A.17 D_s systematics for Q^2 bins . . . 137
A.18 D_s systematics for x bins . . . 137
A.19 D_s systematics for $p_T(D_s)$ bins . . . 138
A.20 D_s systematics for $\eta(D_s)$ bins . . . 138

List of Tables

1.1 Fundamental forces 1
1.2 Quark properties 2

2.1 ZEUS luminosity 13

7.1 D^0 decay length cut 61

8.1 D^0 experimental systematics 80
8.2 HVQDIS systematics 81
8.3 D^0 differential cross sections 84

9.1 $K^0_s X$ systematics 97
9.2 $D^\pm$ differential cross sections 103
9.3 $D^\pm_s$ differential cross sections 104
9.4 Key to systematics used for γ_s measurement 106
9.5 Measurements of the strangeness-suppression factor 108

10.1 $\Lambda^\pm_c$ systematics 118

11.1 Summary of integrated cross sections 121

Chapter 1

Introduction

1.1 Introduction

Particle physics seeks to answer the questions "What is the world made of?" and "How does it work?" at the most fundamental level. The current answer to the first question is "two classes of elementary particles — quarks and leptons". The current answer to the second question is "quarks and leptons interact through four fundamental forces, which are mediated by the exchange of a third class of particles, gauge bosons." The details of these answers comprise the *Standard Model* of particle physics, which has been extremely successful in describing the results of experimental measurements.

The fundamental forces and their associated gauge bosons are summarised in Table 1.1. Gravity is included for completeness, but a successful quantum theory of gravity does not yet exist, so this force remains outside the Standard Model, and the graviton a hypothetical particle.

Force	Associated quantity	Gauge Boson
Electromagnetic	Electric Charge	Photon (γ)
Strong	Colour Charge	Gluon (g)
Weak	Weak Charge	$W^{\pm}$, Z^0
Gravity	Mass	Graviton (g)

Table 1.1: Summary of the four fundamental forces

The elementary particles of matter, that is those which are believed to have no

further substructure, fall into two classes - quarks and leptons. Quarks experience all the fundamental forces, leptons do not experience the strong interaction. There are six leptons which come in three *generations* consisting of a charged particle (electron, muon or tau) and an associated neutral particle (electron-neutrino, muon-neutrino, or tau-neutrino). There are six *flavours* of quark: up, down, strange, charm, bottom and top. These also form three generations, with one quark of charge $+\frac{2}{3}e$ and one of $-\frac{1}{3}e$ in each. In addition quarks carry colour charge, so each flavour exists in three different colours: red, blue or green. The masses and charges of the quarks are summarised in Table 1.2. Since the masses of the last three quarks are so much greater than the first three, they are often referred to as *heavy quarks* or *heavy flavours*. For every quark and lepton there exists an *antiparticle* with the same mass, but opposite quantum numbers.

Flavour	Mass [1]	Electric Charge
up, u	$1.5-3.0\,\mathrm{MeV}$	$+\frac{2}{3}e$
down, d	$3-7\,\mathrm{MeV}$	$-\frac{1}{3}e$
strange, s	$95\pm25\,\mathrm{MeV}$	$-\frac{1}{3}e$
charm, c	$1.25\pm0.9\,\mathrm{GeV}$	$+\frac{2}{3}e$
bottom, b	$4.20\pm0.07\,\mathrm{GeV}$	$-\frac{1}{3}e$
top, t	$174.2\pm3.3\,\mathrm{GeV}$	$+\frac{2}{3}e$

Table 1.2: Summary of the quark properties

Quarks are not observed directly or individually. Instead they are only seen as components of larger particles, known as *hadrons*. There are two types of hadron – *mesons*, which are a bound state of a quark and antiquark, and *baryons*, which are a bound state of three quarks or antiquarks. Quarks are held inside hadrons by the strong interaction, mediated by the exchange of gluons. Since gluons also carry colour charge, they can radiate more gluons or $q\bar{q}$ pairs, which can in turn radiate gluons. Hadrons are therefore filled with a 'sea' of low energy quarks, antiquarks and gluons. Since the strong interaction is carried by gluons the fact that gluons can self-interact means the force between two coloured objects gets stronger with increasing distance. This property is known as *confinement* and is the reason free quarks are not observed. The theory which describes

the behaviour of quarks and gluons is *Quantum Chromodynamics* (QCD).

Although there are no free quarks and gluons, QCD can be be investigated experimentally by, for example, scattering electrons off protons. If the electron has sufficiently high energy it is able to resolve the quarks and antiquarks inside the proton. If enough momentum is then transferred to an (anti-)quark it scatters out of the proton. However as the separation of this quark from the other coloured objects in the proton increases, the colour field lines become squeezed into a tube and the potential energy in the colour field increases, until it becomes energetically more favourable for a $q\bar{q}$ pair to be formed from the colour flux tube. This then generates two new tubes of lower energy, in which the separation between coloured objects continues to increase. These will also eventually split, and so on, with the end result that the struck quark has been converted into a number of hadrons, which are what get measured experimentally. This process is called *fragmentation*.

In this thesis cross sections for the production of hadrons from the fragmentation of a charmed quark are measured.

1.2 Outline

The remainder of this thesis is structured as follows. In Chapter 2 the HERA accelerator and the ZEUS detector, with which the data were collected, are described. Chapter 3 lays the theoretical foundation for the QCD model of the structure of the proton and for the kinematics of deep inelastic scattering (DIS). Chapter 4 deals with topics related to charm quark production. In Chapter 5 the Monte Carlo models and the NLO calculation used are described. Chapter 6 discusses how the DIS kinematic variables can be reconstructed from data, and gives details of the reconstruction of the scattered electron in NC events, and of tracks and vertices in all events. In Chapter 7 the results are shown of a study which investigated the improvement the recently installed Microvertex Detector could give for charm signals, by looking at the $D^* \rightarrow D^0\pi \rightarrow K\pi\pi$ decay for which charm decays could already be well identified. Chapter 8 presents the procedure for, and

the results of, measuring the integrated and differential cross sections for the decay $D^0 \to K^0_s\pi^+\pi^-$. Chapter 9 does likewise for the discriminant method used to obtain cross sections for $D^\pm \to K^0_s\pi^\pm$ and $D^\pm_s \to K^0_s K^\pm$, and also presents a measurement of the strangeness-suppression factor. Chapter 10 gives the results of measuring the integrated cross section for $\Lambda^\pm_c \to \Lambda^0\pi^\pm \to p^\pm\pi^\mp\pi^\pm$ and of the baryon-to-meson ratio. Finally Chapter 11 summarises and discusses the results of this thesis, and suggests how this work may be extended. The Appendix contains plots which relate to details of the extraction of differential cross sections which would otherwise overwhelm the main body of the text.

Chapter 2

HERA and ZEUS

2.1 HERA

The Hadron Elektron Ring Anlage (HERA) [2] is a particle accelerator located at the Deutsches Elektronen Synchroton (DESY) facility in Hamburg, Germany. HERA collides a beam of electrons or positrons[1] with a beam of protons, and is unique among colliding-beam experiments to date in doing so.

The electrons and protons are stored and accelerated in separate beampipes within the HERA ring, which is 6.34 km in circumference and located 10 – 20 m underground. The ring is a flattened circle in shape (see Fig 2.1); the curved sections have a radius of 797 m, while each straight section is 360 m long and contains an experimental hall. The beams are brought into collision in the North and South experimental halls, in which the H1 [3] and ZEUS [4] experiments respectively are located. The HERMES experiment [5] is located in the East Hall, and uses the polarised electron beam (Section 2.1.3) on a fixed target to investigate the spin structure of the proton. The HERA-B experiment [6] was formerly located in the West Hall, and studied CP violation in the $B^0\overline{B^0}$ system with a wire target inserted in the proton beam halo. This experiment concluded data-taking in 2003.

[1] From now on *electron* will be used to refer to both positrons and electrons, unless an explicit distinction is made.

2.1.1 HERA Injection System

Bunch Structure

The beams in HERA are not continuous but consist of bunches. HERA can hold a maximum of 210 bunches for both the protons and electrons, but in practice a smaller number is used. Typically there are 175 bunches used for collisions, 20 unpaired electron or proton bunches (*pilot bunches*) and 15 empty bunches. The pilot bunches can be used to determine beam-based backgrounds; the empty bunches can be used for determining background from cosmic rays, and also act as a safety measure in case of emergency beam dumps.

Electron Beam

The electrons (positrons) are initially accelerated to 220 MeV (450 MeV) by a linear accelerator. A single bunch is then injected into the DESY-II synchrotron where it is further accelerated to 7.5 GeV. From there the bunch is transferred to PETRA, which can hold 70 bunches at the HERA bunch spacing of 96 ns. Electron bunches are accumulated then accelerated to 12 GeV, before being injected into HERA. When the desired number of HERA bunches has been filled, the electrons are accelerated to their final energy of 27.5 GeV. The lifetime of the electron beam is of the order of 10 hours.

In both PETRA and HERA electrons are accelerated by conventional (non-superconducting) radio-frequency (RF) cavities. The limiting factor on the electron beam energy in HERA is energy loss due to synchrotron radiation in the curved sections of the ring. This is countered by a system of sixteen superconducting RF cavities. The magnetic field required to bend the electrons in the curved sections is 0.274 T. The electron beam is focused by conventional magnets.

Proton Beam

The proton beam begins life as H^- ions, which are accelerated to 50 MeV in a linear accelerator. The ions are then transferred to the DESY-III synchrotron where the elec-

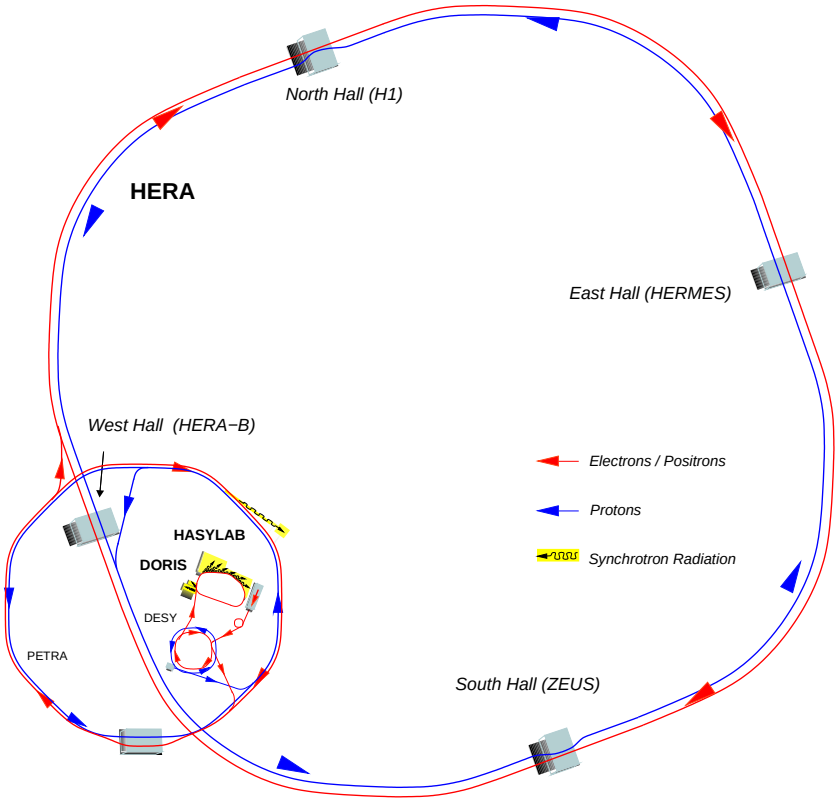


Figure 2.1: HERA injection system

trons are stripped off by passing the beam through a thin foil. The resulting protons, now in 11 bunches, are accelerated to 7.5 GeV before being transferred to PETRA-II, where up to 70 bunches are accumulated. They are then accelerated to 40 GeV before being injected into HERA. When the desired number of HERA proton bunches has been filled the protons are accelerated to 920 GeV.

The proton beam is also accelerated by RF cavities in PETRA and HERA. The limiting factor on the proton beam energy is the magnetic field required to contain the beam. Helium-cooled superconducting dipoles, producing a field of 5.3 T are used to guide the beam, and superconducting quadrupole magnets are used for focusing.

2.1.2 HERA-I Operation

The first collisions in HERA took place in 1991. Regular data-taking commenced in 1992 and continued until 2000 (with regular breaks for maintenance). During this time HERA delivered an integrated luminosity of 190 pb^{-1}, of which ZEUS gated approximately 70%

with the main detector components active. Until 1997 the energy of the proton beam was 820 GeV. Enhancements made in the 1997-8 shutdown allowed this to be increased to 920 GeV, and this energy has been used for all subsequent data-taking.[2] The centre-of-mass energy, $\sqrt{s}$, of the HERA beams is given by $\sqrt{s} = \sqrt{4E_eE_p}$ (neglecting the electron and proton masses). For 820 GeV protons this gives $\sqrt{s} \approx 300\,\text{GeV}$, and for 920 GeV protons, $\sqrt{s} \approx 318\,\text{GeV}$.

In the running period up to 2000 (hereafter referred to as HERA-I) positrons were preferentially used for the lepton beam, due to the longer beam lifetime. This difference in lifetime is partly due to the fact that when the beam consists of electrons, the residual positive ions in the beampipe are attracted towards the beamline and interact with the electrons, whereas with a positron beam the positive ions are repelled.

2.1.3 HERA Upgrade

After the conclusion of data-taking in 2000 there was a long shutdown to enable the upgrade of HERA. The main goals were to increase the peak instantaneous luminosity by a factor of five, from $\sim 1.5 \times 10^{30}\,\text{cm}^{-2}\,\text{s}^{-1}$ to $\sim 7.5 \times 10^{30}\,\text{cm}^{-2}\,\text{s}^{-1}$, and to provide a longitudinally polarised electron beam at the H1 and ZEUS interaction points.

Luminosity is related to the size of the beam at the interaction point (IP). To get a small beam size, and hence high luminosity, the final focusing magnets should be as close as possible, especially the low-β-quadrupole magnets for the proton beam. The position of these magnets is restricted by the geometry of the interaction region – the electron and proton beams must be sufficiently separated so that the magnet can physically fit. The HERA-II upgrade achieved a smaller beam size and higher luminosity by making the separator magnets three times shorter and three times stronger. This allowed the proton quadrupoles to be moved from 27 m from the IP to 11 m, which is actually inside the detector. To reduce beam-beam effects the electron beam cross section should match that of the proton beam at the IP. This required the new separator magnets to have a

[2] with the exception of the final few months of HERA running where lower energies were used, in order to measure the longitudinal structure function (Section 3.3).

The figure originally located here has been removed from this electronic version of the thesis for copyright reasons.

Figure 2.2: Diagram of the magnets comprising a spin rotator. From [8]

focusing function.

The electron beam in HERA becomes transversely polarised by the *Sokolov–Ternov effect* [7]. The electrons emit synchrotron radiation in the curved sections of the ring. A small proportion of the emitted photons cause a flip in the sign of the electron spin. The probability for *up* to *down* transitions is different to that for *down* to *up* transitions, leading to polarisation. Since 1997 a pair of *spin rotators* has been used at the HERMES interaction region to convert the transverse polarisation to longitudinal polarisation before collisions, and back again afterwards. These spin rotators comprise a series of magnets providing horizontal and vertical bending, and replace two of the regular bending magnets at the end of an curved section of the ring. The spin rotation is carried out by having a vertical bump in this magnet chain (see Fig. 2.2). In the HERA-II upgrade spin rotators were also installed around the H1 and ZEUS interaction regions

The upgrade involved rebuilding the magnet system for $\sim 65\,\mathrm{m}$ on either side of the H1 and ZEUS interaction regions.

2.1.4 Background Problems

When beam operation began again in 2001 the experimental collaborations could not take data because of large backgrounds causing high currents in the drift chambers of their detectors. After extensive investigation, three sources of background were eventually identified — synchrotron radiation, electron beam-gas background and proton beam-gas background. The following describes the background situation for the ZEUS experiment.

An increase in synchrotron radiation, although not to the extent initially observed, had been anticipated, due to the greater power of the electron bending magnets, and the fact that their location inside the detector prevented the absorption of synchrotron radiation prior to the interaction region. The synchrotron radiation fan was designed to be led through the detector and absorbed on the other side, and for this purpose a new beampipe and collimators were designed. A number of flaws in the design became apparent once HERA-II beam operations commenced.

The first was that it allowed a direct path to the interaction region for synchrotron radiation from a bending magnet 92 m away. This was remedied by the addition of a collimator 66 m from the IP to remove the part of the synchrotron radiation fan which reached the detector. A fixed collimator was originally installed, but this was later replaced with a movable collimator, which could have different apertures for beam injection and luminosity running, and also did not require the beam to be in the nominal orbit in order to function effectively.

The second problem was back-scattering from the collimators and absorbers downstream of the detector, in particular the collimators C5A at $z = -0.8\,\mathrm{m}$, C5B at $z = -1.4\,\mathrm{m}$, C5C at $z = -1.7\,\mathrm{m}$ (which were designed to protect the detector from backscattered synchrotron radiation), and the synchrotron radiation absorber at $z = -11\,\mathrm{m}$ (The ZEUS coordinate system is described in section 2.2). Synchrotron radiation backscattered from the 11 m absorber and was reflected by the C5A collimator into the interaction region. In addition at particular azimuthal angles ($\phi \approx 168^\circ$ and 192°) synchrotron radiation scattered from the absorber could pass inside the C5C collimator, but outside the C5A collimator, and thus interact with the beampipe throughout the region $z \in [-0.8, 0.5]\,\mathrm{m}$. These 'sneak-through' photons constituted approximately half the photons inside the CTD. To address these issues the C5A collimator was reduced in length from 5 cm to 0.5 cm, this being sufficient to absorb the synchrotron radiation, and thin tungsten shields extending 3.5 cm in the forward and 5.7 cm in the backward directions were added. These significantly reduced the number of photons which were scattered into the CTD. The hole for the sneak-through photons was closed by extending

the C5B collimator. The amount of synchrotron radiation reaching the C5A collimator was reduced by reducing the vertical semi-major axis of the elliptical C5C collimator by 0.6 cm. Attempts were made to coat the 11 m absorber with 100 μm of Molybdenum and 15 μm of Copper to reduce the amount of back-scattered synchrotron radiation, but were ultimately unsuccessful.

The electron-induced particle background was due to the electron beam scattering off the residual gas in the beampipe ('beam-gas interactions'). (The heating caused by the synchrotron radiation described above results in out-gassing from the beampipe and other surfaces, which increases the rate of beam-gas interactions.) The resulting energy loss caused these electrons not to follow the nominal path through the accelerator, but instead collide with the beam pipe and collimators in the interaction region, and produce electromagnetic showers. The reduction in length of the C5A collimator reduced this background by a factor of ~ 2. It was also found that one 5 m long section of the beampipe at $z = -27$ m was unpumped, leading to a pressure five times higher than the surrounding regions. An additional pump was installed to improve the vacuum, and hence reduce the amount of gas able to interact with the beam. The initial proposal was for several ion-getter pumps to be installed, however this would have required holes to be drilled in one of the proton bending magnets through which the electron beampipe passes in this section. Tests were carried out on a spare magnet to ensure that this would not significantly degrade the magnetic field. In the end an integrated non-evaporative getter (NEG) pump was installed, with the beampipe being slightly displaced vertically to accommodate it.

The proton-induced particle background was also due to beam-gas interactions. As in the electron case, the amount of showering was reduced by the reduction in thickness of the C5 collimators. Studies showed the proton beam-gas interactions occurred mostly near the interaction region, 70% before $z = -3.6$ m, with non-negligible components out to $z = -11$ m. (Note that the proton and electron beams share a common beampipe throughout this region). The proton beam-gas was also found to be strongly dependent on the quality of the vacuum, both static and dynamic. The static pressure is the

equilibrium between outgassing from the vacuum chamber and pumping; the dynamic pressure includes additional outgassing caused by higher-order mode (HOM) heating[3] or synchrotron radiation heating during beam operation. The quality of the vacuum was improved by dedicated 'bake-out' runs in which these heating effects were deliberately used to induce outgassing so that the resulting gas could be pumped out. This improved the vacuum in the region beyond $z = -3.6\,\mathrm{m}$. The background coming from the interaction region however was not improved, indicating that this background was related to the quality of the dynamic vacuum. The exact mechanism was not fully understood, however some studies suggested HOM heating was partly responsible. Since this is greater for shorter bunches, the electron beam is now accelerated as quickly as possible after injection into HERA. (Electron bunches are 3 mm long at injection, and 12 mm at 27.5 GeV.) The shape of the new C5 collimators, which are located inside the region of highest proton background, was optimised to reduce HOM heating by using shallow rises rather than steps. The pumping speed of the pumps between $z = -3.6\,\mathrm{m}$ and $z = -11\,\mathrm{m}$ was doubled, which allowed the vacuum to improve more rapidly. It was also found that the cold surfaces of the new superconducting magnets installed as part of the upgrade were acting as a cryogenic pump, and absorbing residual gas. This effect saturates at some point because of the finite surface area; periodic warming up of the magnet to release the gas regenerates this cryopumping behaviour.

In addition to dealing with the causes of the background, the symptoms were also treated – measures were taken to reduce the currents in the drift chamber, the high level of which was the reason the ZEUS detector could not operate. The gain of the chamber was reduced by setting the voltage for the sense wires to 95% of its nominal value. This reduced the pulse sizes, which reduced the current, but also reduced the efficiency for detecting hits. This loss of efficiency was compensated by lowering the pulse-height threshold for detecting a hit, and by doubling the resistance on the post-amplifier cards, to increase the pulse height.

[3]The passage of charged particle bunches past sharp edges induces electromagnetic *wakefields* in the beampipe and metallic structures inside it; these trapped or propagating modes produce currents which result in heating

The result of all these measures was that ZEUS was able to begin high-luminosity data-taking from October 2003. Although the problems with background were resolved before this thesis was begun, they are mentioned to illustrate that HERA-II is a significantly different environment from HERA-I, so it is not immediately obvious that one will obtain better results.

2.1.5 HERA-II Operation

In the HERA-II running period both positron and electron beams have been used. The goal is to obtain roughly equal amounts of luminosity with both types of lepton and both signs of polarisation (see Figure 2.3). To date ZEUS has collected the integrated luminosity shown in Table 2.1.

Luminosity (pb^{-1})		
Year	$\mathcal{L}_{e^+}$	$\mathcal{L}_{e^-}$
2003	2·08	
2004	38·51	
2005		135·6
2006	99·54	61·23
2007	46·35	

Table 2.1: Integrated luminosity collected by ZEUS

For this thesis the 2004 positron data, 2005 electron data and 2006 electron data were used, with the additional requirement that there were no problems with the data from the MVD, giving a total of $225\,\mathrm{pb}^{-1}$. The 2003 positron data were excluded because the triggers used in this analysis were not stable, the 2006-7 positron data were not used because calculation of the average beam position, alignment of the MVD (Section 2.2.2) and other calibrations had not yet been carried out.

HERA has reached a peak specific luminosity of $2.4 \times 10^{30}\,\mathrm{cm}^{-2}\,\mathrm{s}^{-1}\,\mathrm{mA}^{-2}$ and a peak instantaneous luminosity of $5 \times 10^{31}\,\mathrm{cm}^{-2}\,\mathrm{s}^{-1}$.

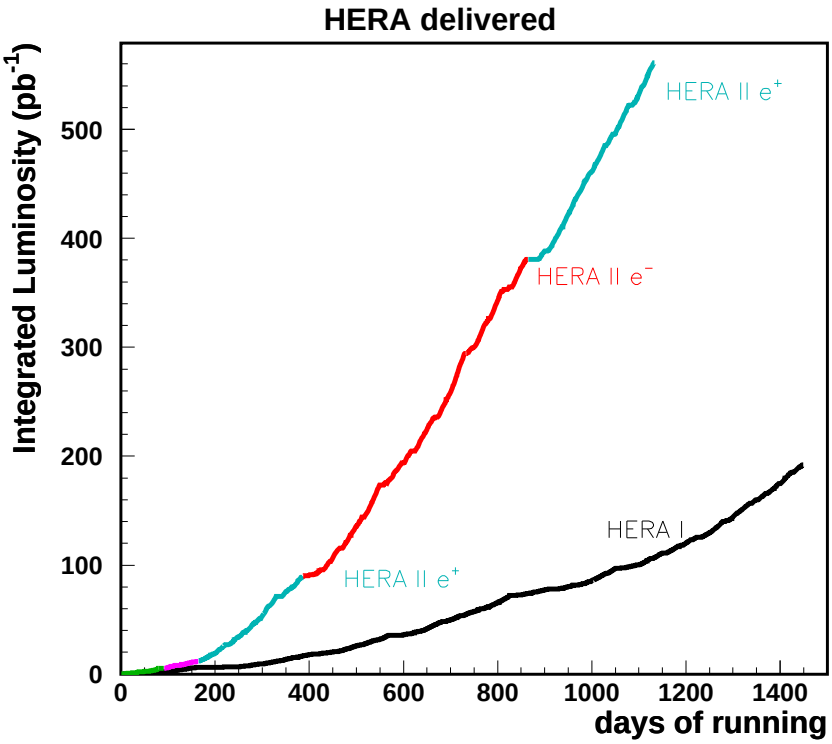


Figure 2.3: Integrated luminosity delivered by HERA

2.2 ZEUS

The ZEUS[4] detector is a large general-purpose detector designed for precision measurement of final state particles from electron–proton collisions. It was constructed and is operated by the ZEUS Collaboration, which comprises physicists and support staff from 58 institutions in 17 countries. The detector is 12 m high, 10 m wide, 19 m long, and weighs 3600 tonnes. A schematic can be seen in Figure 2.4.

In common with other high-energy physics detectors the ZEUS detector consists of concentric layers of sub-detectors, however due to the asymmetric beam energies the detector is more heavily instrumented in the forward direction. At its centre lie the tracking chambers (MVD, CTD, FTD, STT). These are enclosed by a superconducting solenoid which provides a magnetic field of 1.43 T to allow momentum determination of charged particle tracks. This is in turn enclosed by a uranium sampling calorime-

[4]The name was chosen because, in Greek mythology, Zeus is the husband of Hera. In the discussions to choose the name it was allegedly pointed out that this could stand for *Zero Experience with a Uranium Scintillator*. An acronym in ancient Greek was also subsequently devised, *Ζητησις καθ' Ευρετης Υποχειμενης Συμμετριας*, which almost forms an acronym in English as *Search to Elucidate Underlying Symmetries*. None of these acronyms is commonly used.

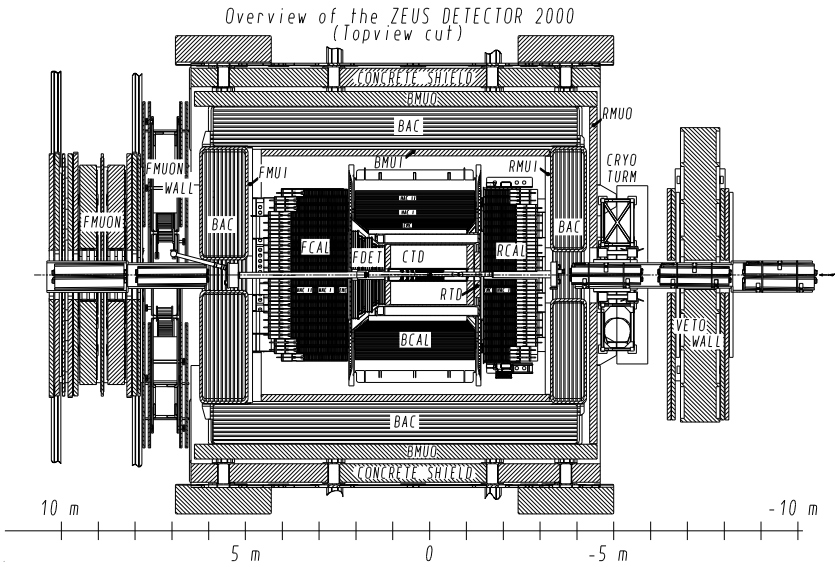


Figure 2.4: Horizontal cross section through the ZEUS detector showing the layout of the main components.

ter (FCAL, BCAL, RCAL). Between the calorimeter and the iron return yoke of the solenoid there are proportional chambers to detect muons (FMUI, BMUI, RMUI). The yoke itself is instrumented to measure the energy of particles which 'punch through' the calorimeter; the proportion of particles which do so is small however, and this Backing Calorimeter (BAC) is now mainly used as an additional muon detector. Outside the BAC and in the forward direction lie more muon chambers (FMUO, BMUO, RMUO). In the rear direction, at $z = -7.5\,\mathrm{m}$ lies the VETO wall, an iron wall equipped with scintillators, which reduces beam-related background. Finally 100 m upstream are a calorimeter and spectrometer for measuring luminosity. The ZEUS detector is described more fully elsewhere [4]; the components relevant to this analysis are described briefly below.

The ZEUS coordinate system is a right-handed Cartesian system (see Figure 2.5). The origin is at the nominal interaction point, which is close to the geometrical centre of the detector. The z-axis points in the direction of the proton beam, and thus positive z direction is often referred to as *forward* and the negative z direction as *backward*. The x-axis points towards the centre of the HERA ring. The y axis points approximately vertically upward. Polar coordinates are sometimes used. ϕ is the azimuthal angle,

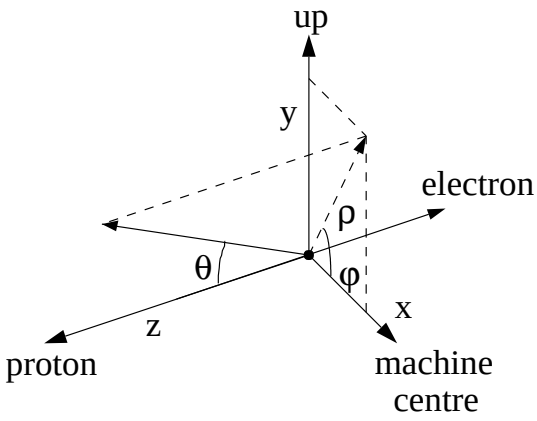


Figure 2.5: The ZEUS coordinate system (see text).

measured from the positive x-axis. The polar angle θ is measured with respect to the positive z-axis, i.e. the proton beam direction. θ is also commonly expressed in terms of the *pseudorapidity*, η, which is defined as $\eta = -\ln(\tan(\theta/2))$, thus $\eta = 0$ corresponds to a direction perpendicular to the beamline, while $\eta = \pm\infty$ are parallel to the beamline.

2.2.1 CTD

The Central Tracking Detector (CTD) [9] is a cylindrical multi-wire drift chamber, designed to measure the trajectories and momenta of charged particles produced in electron–proton collisions. Its active volume has inner and outer radii of 18.2 and 79.4 cm respectively, and extends from $z = -100\,\text{cm}$ to $z = +104\,\text{cm}$, giving polar angle coverage of $11^\circ < \theta < 168^\circ$. The CTD consists of 4608 sense wires and 19584 field wires, and is filled with a gas mixture of Ar (85%), Ethane (10%) and CO_2 (5%). A charged particle passing through the CTD will ionise the gas, and the electrons produced will drift towards the positively charged sense wires. The large electric field at the surface of the wires causes showering, amplifying the signal by a factor of $\sim 10^4$. The electrons are collected on the sense wire, and the positive ions drift to the negative field wires. This induces a pulse on the wire, which is measured by the readout electronics.

The wires are arranged in 72 concentric layers; these are grouped into 9 *superlayers* (SL) numbered outward from one to nine. Within each superlayer the wires are grouped into *cells* (see Figure 2.6). The number of cells per superlayer increases from 32 to 96

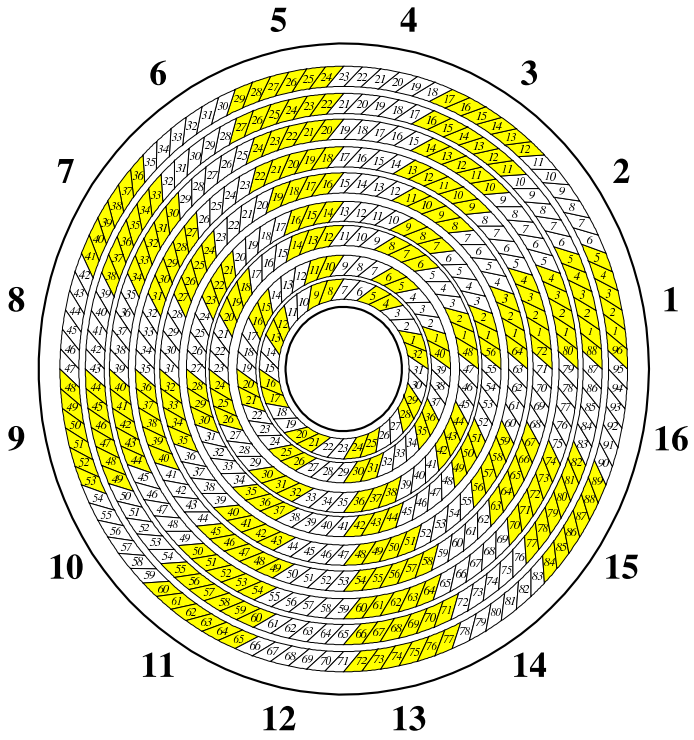


Figure 2.6: A vertical cross section through the CTD, showing cells and superlayers. The 16 sectors into which the CTD is divided for the purposes of readout electronics are also shown.

with the increasing circumference of the superlayer. Each cell contains 8 sense wires and associated field wires (see Figure 2.7). The field wires produce a uniform electric field so that the electron drift trajectories are parallel. This field combined with the magnetic field results in a Lorentz angle of $\sim 45°$; in order to have radial electron drift trajectories (which are important for breaking left–right ambiguities) the orientation of each cell is offset by 45° with respect to the radial direction.

The odd-numbered superlayers have the sense wires oriented parallel to the z-axis (*axial superlayers*), the even-numbered superlayers have the sense wires at a angle of $\sim \pm 5°$ to the beam direction (*stereo superlayers*). This allows measurement of the z coordinate as well as the $r\phi$ coordinates; the resolutions for a track which has passed through all nine superlayers are $\sim 2\,\text{mm}$ in z and $\sim 180\,\mu\text{m}$ in $r\phi$. Superlayers 1, 3 and 5 are also instrumented with the *z-by-timing* system. This determines the z position of a hit on one of the instrumented wires by measuring the difference between the arrival times of the pulses at each end of the detector. The resolution ($\sim 4\,\text{cm}$) is poorer than

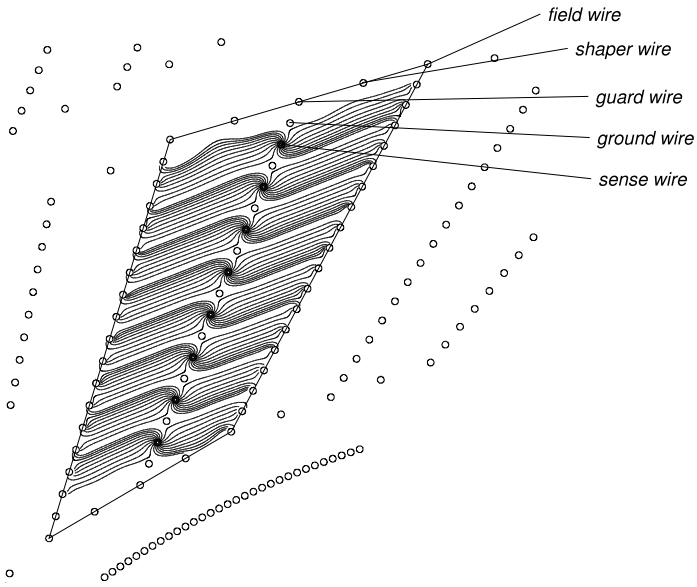


Figure 2.7: A cell in the CTD, showing layout of field and sense wires.

that obtained using the full axial and stereo information, however the z-by-timing system is able to produce a result rapidly, which makes it suitable for use in the trigger and for providing seeds for track finding.

The solenoidal magnetic field of 1.43 T causes charged particle tracks to curve, with a radius of curvature given by

$$R \propto \frac{p_T}{BQ} \tag{2.1}$$

where p_T is the component of the particle's momentum transverse to the magnetic field. This relation together with a map of the magnetic field strength throughout the detector is used to determine particle momenta. Prior to the HERA-II upgrade the momentum was determined entirely by the CTD, with a resolution [10]

$$\frac{\sigma(p_T)}{pT} = 0.0058 p_T \oplus 0.0065 \oplus \frac{0.0014}{p_T} \tag{2.2}$$

where p_T is measured in GeV, and $\oplus$ indicates contributions added in quadrature. The first term comes from the intrinsic hit resolution and the number of hits, the second and third terms come from the multiple scattering of the particle before and inside the CTD. As part of the upgrade a silicon micro-vertex detector (section 2.2.2) was

installed between the beampipe and the CTD. This affected the momentum resolution by providing more precise hit measurements (reducing the first term in Eq. 2.2), but also increasing the amount of material through which particles had to travel, and hence the amount of multiple scattering (increasing the other terms). The final resolution of the post-upgrade tracking has yet to be determined, as the track reconstruction software continues to be developed. Some early results suggest the following parametrisation: [11]

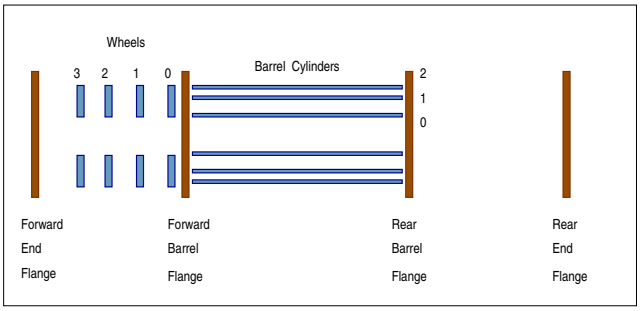
$$\frac{\sigma(p_T)}{pT} = 0.0026 p_T \oplus 0.0104 \oplus \frac{0.0019}{p_T}. \tag{2.3}$$

2.2.2 MVD

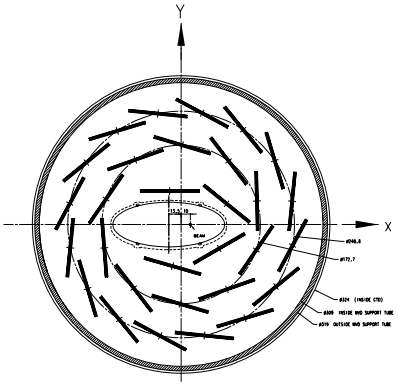
During the HERA-II upgrade a silicon microvertex detector (MVD) [12] was installed in the centre of the ZEUS detector, between the beampipe and the CTD. A drift-chamber vertex detector (the VXD) had previously been installed in the same position but was removed in the 1995/6 shutdown as high beam backgrounds prevented it from being operated continuously. The motivation for both of these detectors was to be able to identify secondary vertices coming from the decays of long-lived heavy particles, i.e. those with $c\tau \geq 100\,\mu\text{m}$. By providing additional and more precise hits the vertex detector also improves the pattern recognition and track reconstruction.

The MVD uses silicon strip sensors consisting of 300 μm of n-type silicon, with strips of p-type silicon 20 μm apart on the top surface. When a charged particle passes through the sensor, electron-hole pairs are generated in the n-type bulk. The holes drift to the p-type strips which are maintained at a negative potential. Only every sixth strip is read out (to minimise the number of readout channels), but capacitive charge sharing [13] results in a resolution better than the readout pitch.

Sensor modules are arranged on carbon-fibre support structures (*ladders*) in three concentric layers in the barrel region of the MVD, and in planar *wheels* in the forward region of the MVD, as shown in Figure 2.8. The shape of the sensor module is different for the two regions, however in both cases it consists of two half-modules joined back to



(a) A schematic showing the layout of the MVD.

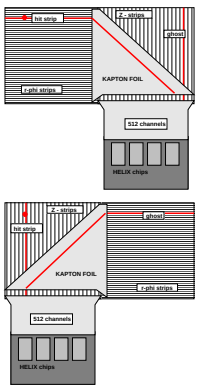


(b) A vertical cross section through the MVD showing the layout of the ladders on which the sensors are mounted.

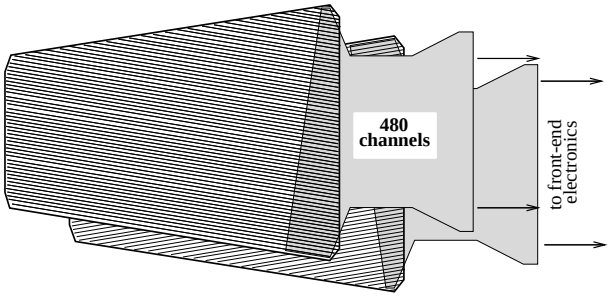
Figure 2.8:

back, with the orientation of the silicon strips in one half-module rotated relative to that in the other half-module. This allows the two-dimensional position of the hit in the sensor plane to be reconstructed. A barrel half-module consists of two 6.42 cm × 6.42 cm squares of silicon glued together side by side. Each square has 512 readout strips; the strips in one square are parallel to the beamline, those in the other square are perpendicular. (The strips in the second half-module which is combined with this to make a full module have the opposite orientation, see Figure 2.9 a.) The readout strips of one square are electrically connected to those of the other square by a triangular piece of Kapton foil. This reduces the number of readout channels per half-module to 512, but introduces an ambiguity in the hit position, which is resolved during track reconstruction. A wheel half-module is wedge-shaped and contains 480 readout strips, which are parallel to one of the long sides of the wedge. The two half-modules have strips oriented parallel to opposite sides of the wedge, creating an angle of $\sim 13^\circ$ between them.

The barrel section of the MVD, which is centred on the nominal interaction point, is 62.2 cm long and covers the polar angle range $\theta = 22^\circ$ to $\theta = 160^\circ$. It consists of 30 ladders arranged in three cylindrical layers, each ladder containing five full modules. The outer two layers have full azimuthal coverage, and are located at radii of 8.5 cm and 12.3 cm respectively. The innermost layer does not have full azimuthal coverage (see Figure 2.8) – this is due to the elliptical shape of the beampipe, and the fact that it is



(a) The two half-modules of a barrel module.



(b) The two half-modules of a wheel module.

Figure 2.9:

offset from the axis of the CTD in order to accommodate the synchrotron radiation fan within the beampipe. The ladders in this layer are at radii of $3 - 5\,\text{cm}$.

The forward section of the MVD extends the polar angle coverage down to 7°. It consists of four wheels, each made up of 14 modules as shown in Figure 2.10. Some of the modules are shorter in order to accommodate the elliptical beampipe. The wheels are located at $z = 31, 44, 57$ and $72\,\text{cm}$.

With the current level of alignment the hit resolution of the MVD is $\sim 25\,\mu\text{m}$, which translates into a resolution of $\sim 100\,\mu\text{m}$ on the ep vertex.

2.2.3 Calorimeter

The ZEUS calorimeter (CAL) [14] is a high-resolution compensating calorimeter, consisting of alternating layers of 2.6 mm plastic scintillator and 3.3 mm depleted uranium absorber. *Compensating* refers to the fact that the energy response is the same for both electrons and hadrons (for the ZEUS CAL $e/h = 1.0 \pm 0.05$ for momenta greater than 2 GeV [4]). This is achieved by the choice of materials and thickness of the layers; fewer photons are produced in the shower caused by a hadron than from an electron of the same energy, however the spallation neutrons produced by hadronic interactions in the uranium cause protons to recoil in the scintillator which produces more photons. Compensation is important for precise reconstruction of jets, where the relative sizes of the electromagnetic and hadronic components are initially unknown.

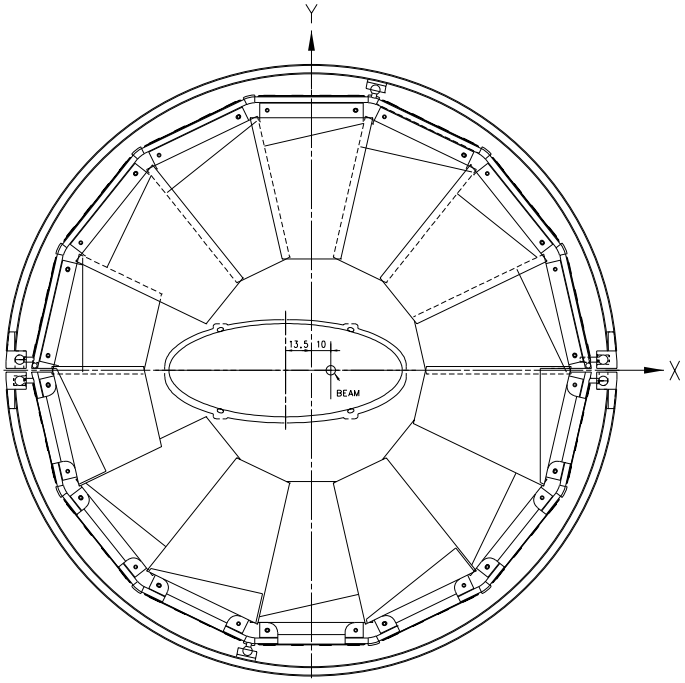


Figure 2.10: Schematic showing the layout of modules within an MVD wheel.

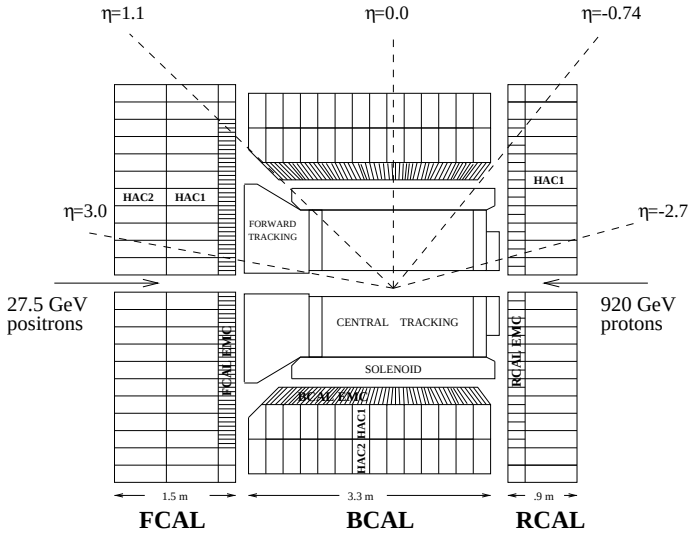


Figure 2.11: Schematic showing the sub-sections of the ZEUS calorimeter.

The calorimeter covers 99.7% of the solid angle (the beampipe prevents full 4π coverage), which is important for reconstructing final states involving "missing energy" (e.g. containing an energetic neutrino). It is divided into three sections – forward (FCAL), barrel (BCAL) and rear (RCAL), as shown in Figure 2.11. The basic sensor unit of the CAL is the cell, of which there are 5918. Each cell consists of alternating layers of uranium and scintillator, with wavelength-shifting fibres leading to photomultiplier tubes

(PMT) attached to the left and right sides. The sum of the signals of the two PMTs is related to the energy deposited in the scintillator, while the imbalance between the two signals can be used to determine the position within the cell. The sharp rising-edge of the pulse allows the time of arrival to be determined very precisely (within 1 ns for energy deposits $> 4.5\,\mathrm{GeV}$). This timing information can be used to reject events which are not consistent with coming from an *ep* collision (e.g. cosmic rays, interactions in the beam halo). It can also be used to estimate the position of the interaction vertex, with a resolution of $\sim 9\,\mathrm{cm}$. This is mostly useful for events where there are no or very few tracks within the acceptance of the tracking detectors.

Cells are grouped together to form *towers* with $20\,\mathrm{cm} \times 20\,\mathrm{cm}$ cross section. Each tower is subdivided longitudinally into an electromagnetic calorimeter (EMC) and hadronic calorimeter (HAC), as shown in figure 2.12

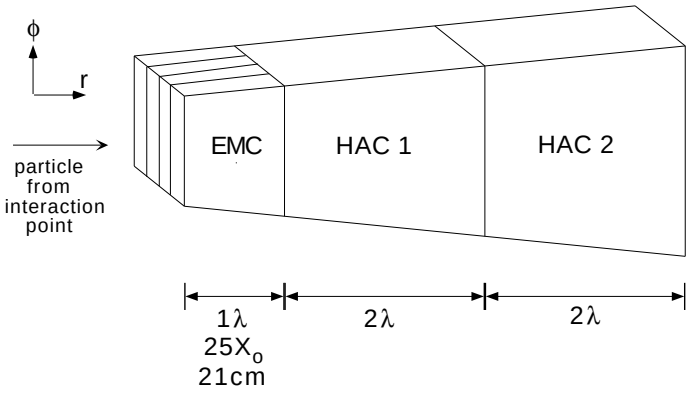


Figure 2.12: One tower from the barrel calorimeter, showing the individual EMC and HAC cells

Because of the asymmetric beam energies of HERA, the particles produced in the collisions are Lorentz-boosted in the forward direction. For this reason the FCAL and BCAL towers are deeper than those of the RCAL. In the FCAL the EMC comprises the first 25 layers of uranium and scintillator, approximately 1 interaction length (λ). The HAC is divided into two cells, HAC1 and HAC2, each of which comprises 80 layers or 3.1λ. In the BCAL the EMC comprises 21 layers, and each of the HAC cells 49 layers or 2.0λ. In the RCAL the EMC is the same as for the FCAL, but the HAC consists of a single cell of 3.1λ. The HAC cells always have the same cross section as the tower,

however the EMC is subdivided into four cells with cross section 5 cm × 20 cm in the FCAL and BCAL towers, and two cells with cross section 10 cm × 20 cm, in the RCAL. (In the parts of the FCAL and RCAL which are screened from the interaction point by the BCAL, the EMC is not subdivided and is referred to as HAC0.) Mechanically the towers are grouped into *modules*, either vertically in the case of the FCAL and RCAL (see Figure 2.13), or radially in the case of the BCAL.

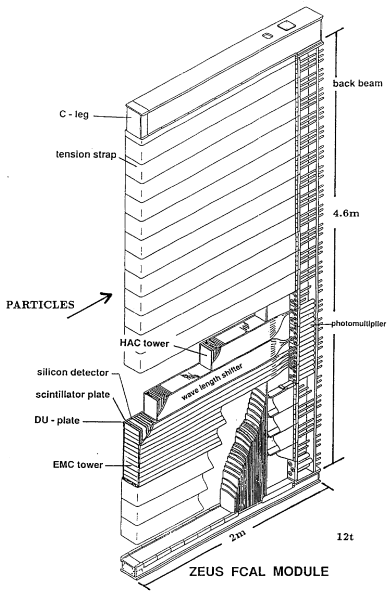


Figure 2.13: One module from the forward calorimeter, showing the arrangement of the towers

Test-beam studies have determined the energy resolution to be

$$\frac{\sigma(E)}{E} = \frac{0.18}{\sqrt{E}} \oplus 0.02 \tag{2.4}$$

for electromagnetic showers, and

$$\frac{\sigma(E)}{E} = \frac{0.35}{\sqrt{E}} \oplus 0.01 \tag{2.5}$$

for hadronic showers, with E measured in GeV.

2.2.4 Luminosity Monitor

The number of events observed in a given time for a process with cross section σ is given by

$$N = \sigma \mathcal{L}, \tag{2.6}$$

where $\mathcal{L}$ is the integrated luminosity. To obtain cross sections from experimental rate measurements it is necessary to have a precise value for the luminosity. In principle this can be determined from the properties of the beams, but in practice the rate of a process with a large and well-known cross section is often used. In the case of ZEUS luminosity is determined by measuring photons from the Bethe-Heitler bremsstrahlung process $ep \rightarrow ep\gamma$.[15]

The HERA-II upgrade necessitated an upgrade in the luminosity detector for two reasons; firstly the large increase in synchrotron radiation would have caused too much radiation damage to the existing photon calorimeter, and secondly the higher luminosity implies a higher rate of Bethe-Heitler photons, which would lead to pile-up effects and consequent loss of precision.

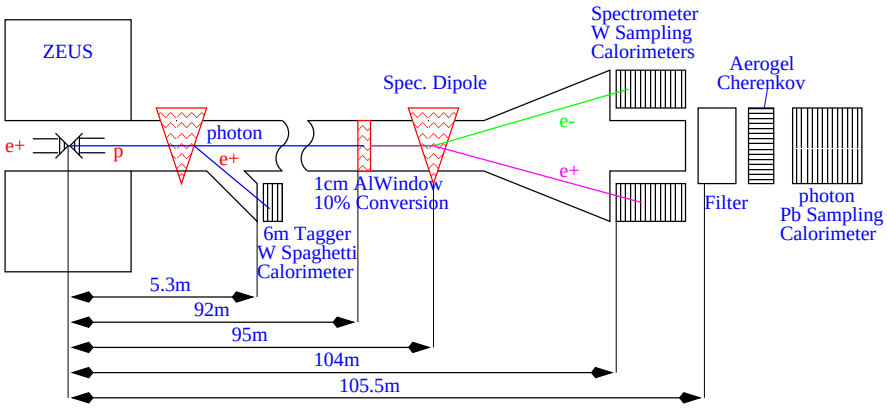


Figure 2.14: Schematic showing the location of the luminosity monitors

The current design of the luminosity detectors can be seen in Figure 2.14. There are now two independent luminosity monitors, the *calorimeter* and the *spectrometer*. In addition there is a small calorimeter located inside a quadrupole magnet $\sim$ 6 m from the interaction point, the 6 m *tagger*, which is used for cross-checking or determining the acceptance and energy calibration of the two detectors. The calorimeter determines the

Bethe-Heitler rate by counting photons above a certain energy threshold. It deals with the increased radiation by the addition of more shielding in front of the detector. Inactive shielding would degrade the energy resolution too much, so an *active filter* design was used. This consists of two sections, each with a two radiation-length, $2X_0$, thick carbon absorber followed by an aerogel Cerenkov counter. The signal in the Cerenkov counters is proportional to the energy deposited in the preceding absorber and can be used to correct the energy deposit measured in the calorimeter. Pileup effects are minimised by an appropriate choice of threshold.

The spectrometer makes use of the fact that $\sim 10\%$ of photons are converted to e^+e^- pairs when passing through the exit window in the beampipe. The leptons are separated by a dipole magnet and measured by two small calorimeters located symmetrically above and below the beampipe. Since the synchrotron radiation is largely confined to the horizontal plane it does not affect these detectors. Pileup effects and radiation damage are reduced to the few percent level by the small acceptance (including the conversion fraction) for this detector.

2.2.5 Trigger and Data Acquisition

The HERA bunch spacing of 96 ns results in a bunch-crossing frequency of 10.4 MHz. Approximately one in a hundred bunch crossings results in a detectable collision. This rate of $\sim 10-100$ kHz (depending on vacuum conditions) is dominated by proton beam-gas interactions. By contrast the rate of interesting physics events (and the rate compatible with offline data storage limitations) is a few Hz. A three-level trigger system [16] is used to obtain the necessary rate reduction.

First Level Trigger

The first level trigger (FLT) is a hardware-based trigger. The participating detector components have dedicated processors which use data with a relatively coarse resolution to calculate quantities like calorimeter sums, vertex position, regional muon information etc. This is largely done using memory look-up tables. The Global first level trigger

(GFLT) integrates the information from the components to determine whether the event is accepted or rejected. The time between bunch crossings is too short for this processing to occur, however, so the data from each component is fed into a pipeline 4.4 μs long (which corresponds to 46 bunch crossings). The component FLTs provide their results to the GFLT within $\sim 2\,\mu s$, which in turn provides its decision as the events reach the end of the pipeline. The FLT has a high efficiency for physics events, $\sim 100\%$, but a low purity, $\sim 1\%$. The typical output rate is 1 kHz.

Second Level Trigger

The second level trigger, based on a network of transputers, is both pipelined and parallel. The components' processors have access to the fully digitised data, which, together with the longer processing time, allows more complicated processing to be carried out, e.g. track reconstruction and energy clustering. These quantities are sent to the global second level trigger (GSLT) which uses them in a set of vetos, to reject background events, and a set of physics filters, designed by the physics analysis groups. An event is accepted if it passes at least one filter and is not rejected by the vetos. The GSLT decision is delivered in ~ 6 ms; the maximum output rate is 60 Hz. On a GSLT accept the data from all the components is sent directly to the event builder (EVB) which combines it into a single ADAMO [17] record, and stores it for processing by the third level trigger. In order to include the MVD in the trigger system a new global tracking trigger (GTT) [18], implemented on a farm of PCs, has been developed. Because the MVD provides only two or three hits per track it is necessary to combine this with information from the other tracking detectors. (In practice only the CTD and MVD are used in the GTT.) The GTT provides tracking and vertex information to the GSLT which is superior to that provided by the CTD-SLT, due to the higher resolution of the MVD, and the greater processing power of the PCs. Consequently the CTD-SLT has been switched off since 2005, with a small improvement in the latency of the SLT.

Third Level Trigger

The third level trigger (TLT) consists of a cluster of PCs running a version of the offline reconstruction software which has been modified to increase the speed. The TLT is the first trigger level which combines data from all components, and has more time than the preceding levels, so is able to do more sophisticated track reconstruction, jet finding, muon reconstruction etc. Vetos and physics filters are again applied, and accepted events transferred via a dedicated optical link to the DESY computer centre where they are written to tape by a tape robot. The TLT output rate is $\sim 5\,\mathrm{Hz}$. Subsequently events are reprocessed with the full offline reconstruction software and up-to-date calibrations.

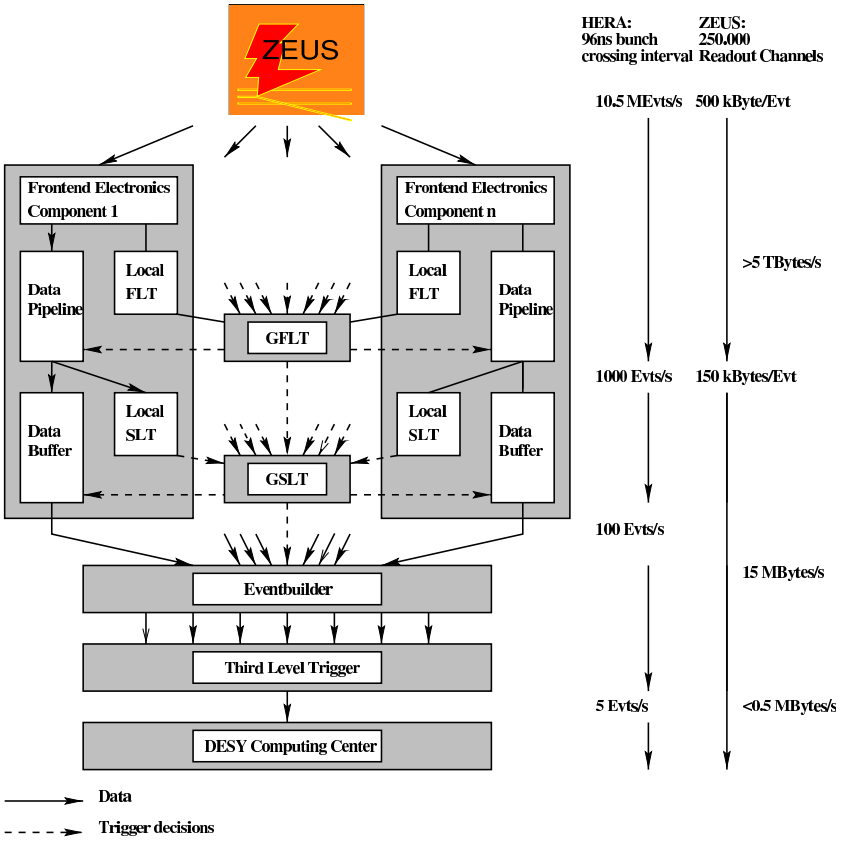


Figure 2.15: Schematic showing the architecture of the ZEUS three-level trigger system

Chapter 3

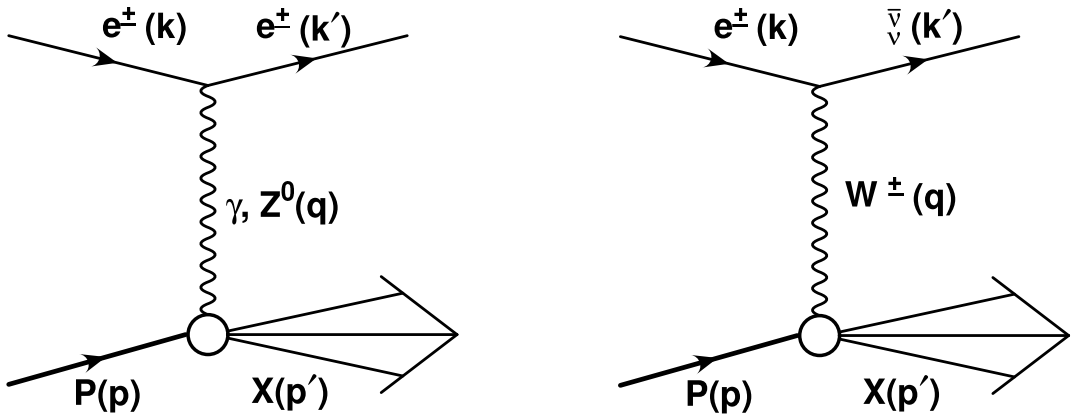
Electron–Proton Collisions and QCD

3.1 Electron–Proton Scattering

In the Standard Model the lowest order interaction between an electron and a proton involves the exchange of a single electroweak gauge boson, a γ, $W^{\pm}$ or Z^0. If the exchanged boson is a γ or Z^0, as shown in Figure 3.1(a), the process is known as a *neutral current* interaction (NC); in the case of $W^{\pm}$ exchange (Figure 3.1(b)) it is known as a *charged current* interaction (CC). If the proton remains intact the scattering is said to be *elastic*; if the proton breaks up the scattering is *inelastic*. *Deep inelastic scattering* (DIS) occurs when $Q^2 \gg \Lambda^2_{QCD}$, where Q^2 is the photon virtuality (see Section 3.2) and the QCD scale $\Lambda_{QCD} \simeq 0.2\,\text{GeV}$.

3.2 Kinematics

Four Lorentz-invariant quantities are used to describe the kinematics of electron–proton scattering. The quantities k, k', p, p' and q used below refer to the four-momenta of the interacting particles as shown in Figure 3.1.



(a) Neutral current electron–proton scattering.

(b) Charged current electron–proton scattering

Figure 3.1:

The momentum transfer from the electron to the proton system is given by

$$q = k - k' \tag{3.1}$$

Since q^2 is always negative is is convenient to introduce the positive quantity Q^2, defined as

$$Q^2 = -q^2 = -(k - k')^2 \simeq 2k \cdot k' \tag{3.2}$$

where the approximation comes from neglecting the electron mass. Q^2, known as the *virtuality* of the boson, can take any value between 0 and the centre-of-mass energy of the system.

The *inelasticity*, y, is given by

$$y = \frac{p \cdot q}{p \cdot k} \tag{3.3}$$

and in the proton rest frame corresponds to the fraction of the electron-beam energy transferred to the proton.

The *Bjorken scaling variable*, x, [19–21] is defined as

$$x = \frac{-q^2}{2p \cdot q} = \frac{Q^2}{2p \cdot q}, \tag{3.4}$$

and is so called because the proton structure function (Section 3.3) for a fixed value of x

is independent of Q^2, i.e. it exhibits scaling behaviour. In a frame in which the proton has infinite momentum x also corresponds to the fraction of the proton momentum which is involved in the interaction.

The centre-of-mass energy of the system $\sqrt{s}$ is given by

$$s = (p + k)^2 \simeq 2p \cdot k, \tag{3.5}$$

where again the approximation comes from neglecting the particle masses. If we make this approximation then s can also be expressed in terms of the three preceding variables as

$$s = \frac{Q^2}{xy}, \tag{3.6}$$

thus for a fixed centre-of-mass energy (as there is for ep collisions at HERA) only two of Q^2, x and y are necessary to completely describe the kinematics of the event.

Q^2 can also be considered as a measure of the resolving power of the exchanged boson. The wavelength, λ, is connected to the three-momentum $|\boldsymbol{q}|$ by the De Broglie relation[1] $\lambda = 1/|\boldsymbol{q}|$. From the definitions above it follows that

$$|\boldsymbol{q}| = (q_0^2 - q^2)^{\frac{1}{2}} = (q_0^2 + Q^2)^{\frac{1}{2}}. \tag{3.7}$$

where $q_0 = E - E'$. In the proton rest frame $p \cdot q = M(E - E') = Mq_0$. Substituting this into Eq. 3.4 gives

$$q_0 = \frac{Q^2}{2Mx} \tag{3.8}$$

Substituting Eq. 3.8 into Eq. 3.7 gives

$$|\boldsymbol{q}| = \left[\left(\frac{Q^2}{2Mx}\right)^2 + Q^2\right]^{\frac{1}{2}} = \left(\frac{Q}{2Mx}\right)\sqrt{Q^2 + 4M^2x^2}. \tag{3.9}$$

In the limit that $Q^2 \gg 4M^2x^2$ this then yields the following relation for the wavelength

[1]Here and elsewhere we use the convention $\hbar = c = 1$

of the virtual boson:

$$\lambda = \frac{2Mx}{Q^2}, \tag{3.10}$$

thus as Q^2 increases, the wavelength and hence the size of objects the boson can resolve decreases.

3.3 Cross Sections and Structure Functions

The expression for the electromagnetic NC cross section can be written in terms of a product of independent leptonic ($L_{\mu\nu}$) and hadronic ($W^{\mu\nu}$) tensors:

$$\mathrm{d}\sigma^{ep} \sim L_{\mu\nu} W^{\mu\nu}. \tag{3.11}$$

The leptonic tensor can be calculated in QED and at leading order has the form

$$L_{\mu\nu} = 2\left(k'_\mu k_\nu + k'_\nu k_\mu + \frac{q^2}{2} g_{\mu\nu}\right), \tag{3.12}$$

where $g_{\mu\nu}$ is the metric tensor.

The hadronic tensor parameterises the interaction at the hadronic vertex, including the non-perturbative component. In its most general form it depends on the metric tensor and the products of the proton and photon momenta. After some simplifications $W^{\mu\nu}$ can be written as

$$W^{\mu\nu} = W_1\left(-g^{\mu\nu} + \frac{q^\mu q^\nu}{q^2}\right) + W_2 \frac{1}{M^2}\left(p^\mu - \frac{p\cdot q}{q^2} q^\mu\right)\left(p^\nu - \frac{p\cdot q}{q^2} q^\nu\right), \tag{3.13}$$

where W_1 and W_2 are the *inelastic structure functions*.These are dimensionless functions of any two of the Lorentz scalars formed from the particle momenta, and describe the charge density distribution of the proton. It is conventional to write these in terms of the structure functions $F_1(x, Q^2)$ and $F_2(x, Q^2)$. (The above discussion ignores NC interactions via Z^0 exchange. If these are included a third structure function, W_3 or F_3 appears in the hadronic tensor, which accounts for the parity violating terms coming

from Z^0 exchange alone, or from $\gamma - Z^0$ interference.)

$$F_1(x, Q^2) = MW_1 \tag{3.14}$$

$$F_2(x, Q^2) = \frac{p.q}{M} W_2 \tag{3.15}$$

It is also useful to define the *longitudinal structure function*, F_L:

$$F_L = F_2 - 2xF_1. \tag{3.16}$$

The double differential electromagnetic NC cross section can then be expressed as

$$\frac{\mathrm{d}^2\sigma^{ep}}{\mathrm{d}x\mathrm{d}Q^2} = \frac{2\pi\alpha^2}{xQ^4}\Big[\Big(1 + (1-y)^2 F_2(x, Q^2)\Big) - y^2 F_L(x, Q^2)\Big] \tag{3.17}$$

3.4 Quark Parton Model

The above form for the cross section is quite general – all the physics is encoded in the structure functions. These might be expected to have a complex form, however in 1968 Bjorken predicted [20] that at high energies F_1 and F_2 should become independent of Q^2, and depend only on x (*Bjorken scaling*). He arrived at this prediction by considering the infinite momentum limit of asymptotic sum rules. The paper ended with the sentence "A more physical approach into what is going on is, without question, needed." This was provided by Feynman's *parton model* [22]. In this model the proton is composed of point-like objects called *partons*; the inelastic scattering of the electron off the proton is regarded as elastic scattering off one of the partons. The point-like nature of the partons means that increasing resolution i.e. increasing Q^2 will not affect the result.

The form of the structure functions can be obtained by working in the frame where the proton has infinite momentum. This allows the partons to be treated as massless, non-interacting particles with only longitudinal momenta. If the struck parton initially carried a fraction ξ of the proton's momentum p, then its mass after the collision is given

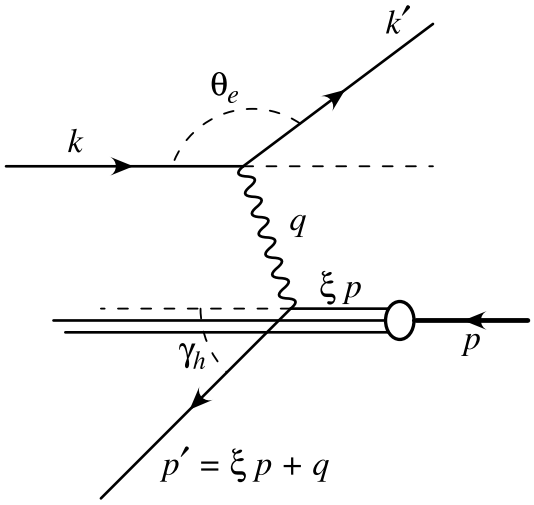


Figure 3.2: The quark–parton model description of DIS kinematics

by

$$p'^2 = (\xi p + q)^2 = \xi^2 p^2 + 2\xi p \cdot q + q^2. \tag{3.18}$$

Taking the parton to be massless gives

$$2\xi p \cdot q + q^2 = 0, \tag{3.19}$$

and hence

$$\xi = \frac{-q^2}{p \cdot q} = x. \tag{3.20}$$

We can therefore identify the Bjorken scaling variable as the fraction of the proton's momentum carried by the interacting parton (in the infinite momentum frame of the proton). The structure functions must depend on the product of the cross section for the electron to interact with a parton of a given momentum fraction, and the probability for finding a parton with that momentum. Introducing the *parton distribution functions* (PDFs), $f_i(x)$, which give the probability density for finding a parton of type i with momentum fraction in the range $(x, x + \mathrm{d}x)$, we can write the structure functions as

$$F_1(x) = \frac{1}{2} \sum_i e_i^2 f_i(x) \tag{3.21}$$

$$F_2(x) = \sum_i e_i^2 x f_i(x), \tag{3.22}$$

where e_i is the electric charge of a parton of type i, and the sum is over all allowed parton species.

Equation 3.21 also yields the *Callan-Gross* relation [23]

$$F_2 - 2xF_1 = 0, \tag{3.23}$$

which is only true for spin-1/2 particles, implying partons have spin-1/2. It also implies that the longitudinal structure function F_L is equal to zero.

The parton model therefore predicts that the proton is made up of massless, charged, spin-1/2 particles, and that the structure functions should exhibit scaling. Scaling was observed experimentally at SLAC [24] in 1969 (see Figure 3.3 for some more recent results). This provided compelling evidence for the parton model, and for the identification of partons, because of the properties predicted for them, with the quarks of Gell-Mann and Zweig, which had previously been considered more as mathematical entities which correctly described the quantum numbers of hadrons, rather than real particles. This model therefore became known as the *Quark–Parton Model* (QPM).

Subsequent experiments proved the QPM to be inadequate – the momentum obtained via a momentum sum rule from the momenta of the charged partons was only half the measured momentum of the proton. This implies that $\sim 50\%$ of the proton's momentum is carried by neutral partons. These were identified with the gluons, gauge bosons of the strong interaction. Experimental evidence for gluons was obtained at DESY by the measurement of three-jet events from e^+e^- collisions [25]. Including gluons in the QPM also allows for the possibility of gluon radiation from quarks. Such gluons can fluctuate into $q\bar{q}$ pairs, or into more gluons, which results in a sea of $q\bar{q}$ pairs at low x which can themselves interact with the electron. This leads to the violation of scaling — the constituents of the proton are no longer point-like, but as the resolution of the probe (i.e. Q^2) increases, more and more partons can be resolved. This Q^2 dependence can be seen in Figure 3.3. At high x the 'valence' quarks dominate; they cannot have lost too much momentum from gluon radiation in order to have a high value of x, so this

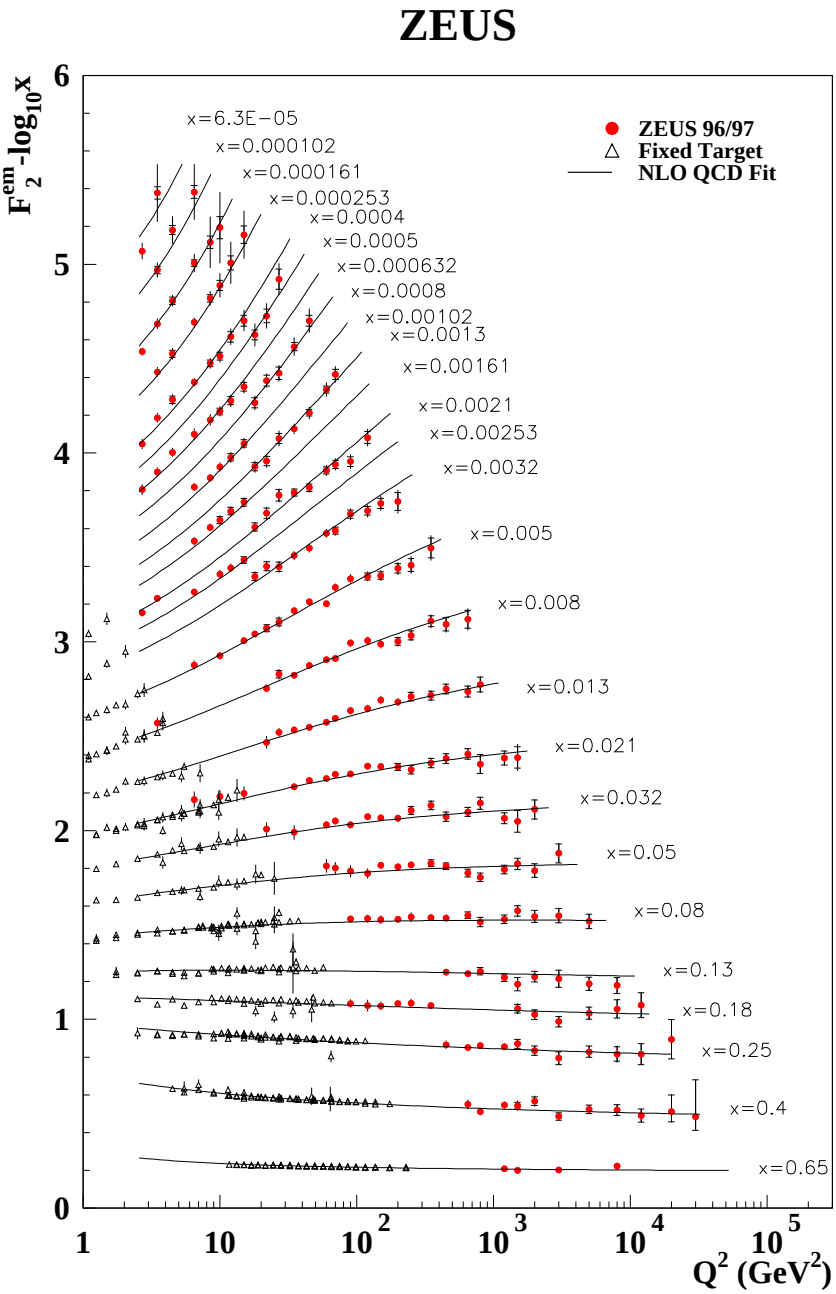


Figure 3.3: Measurements of the structure function F_2 for various x as a function of Q^2.

corresponds closely to the naïve QPM case, and scaling is observed. At low x the 'sea' quarks dominate; the quark density, and hence F_2, increases with increasing Q^2.

Another consequence of adding gluons to the QPM is that by radiating a gluon a quark gains transverse momentum. This means that the longitudinal structure function F_L is no longer zero. Measurement of F_L can therefore give information about the gluon content of the proton. This is difficult experimentally because it requires measurements

at different energies in order to disentangle F_2 and F_L, and accelerators usually operate at a fixed energy. HERA is however running at lower energies for the last few months of its operation in order to allow a measurement of F_L to be made.

3.5 Photoproduction

In DIS the virtuality Q^2 is large enough to provide a hard scale so that perturbation theory is applicable. However the *ep* cross section (Eq. 3.17) has a Q^{-4} dependence, from the photon propagator, which means that the cross section is dominated by events where Q^2 does not provide a hard enough scale. For these events an alternative scale needs to be found; in practice this is done by requiring the presence of a jet with large transverse energy, E_T. The E_T of the jet is then used as the scale of the interaction.

The low Q^2 in these events implies that the virtual photon is almost massless. In addition its lifetime, given by $t \sim \frac{E}{Q^2}$, is long compared to the hard interaction. These properties imply that the exchanged photon is almost real, hence this class of events is referred to as *photoproduction* (PHP). The results presented in this thesis are restricted to DIS as these events are easier to identify, thus PHP needs to be removed as a background. Photoproduction has a larger cross section, however, so the statistical precision of the measurements made could be improved by combining both DIS and PHP.

Photoproduction events can be divided into two classes in leading-order QCD. *Direct photoproduction* is when the photon acts as a point particle, just like in DIS. In *resolved photoproduction* the photon fluctuates into $q\bar{q}$ pairs, which may radiate gluons. It is one of these partons which interacts with the partons in the proton.

Chapter 4

Heavy Quark Production

The quarks with masses much larger than Λ_{QCD} (i.e. c, b and t) are often referred to as *heavy quarks* or *heavy flavours*. For these quarks the mass provides another hard scale for the event (in addition to Q^2 for DIS, or E_T for PHP). Measurement of charm production therefore provides another test of perturbative QCD.

Many charmed hadrons decay weakly to a strange hadron, resulting in a relatively long lifetime. This leads to secondary decay vertices displaced from the ep vertex by $\sim 100 - 300\,\mu\text{m}$, which are now resolvable by the MVD. Work is ongoing to make an inclusive measurement of charm production by tagging these secondary vertices; in the meantime charm production is measured exclusively by reconstructing particular decay modes of charmed hadrons.

4.1 Production Mechanisms

There are a number of different mechanisms by which charmed hadrons may be produced in the final state of ep interactions, including boson–gluon fusion (BGF), flavour excitation, resolved-photon contributions, beauty decays and fragmentation.

Comparison of measurements from both H1 [26] and ZEUS [27] with Monte Carlo has shown BGF (Figure 4.1(a)) to be the dominant charm production mechanism in DIS at HERA.

In flavour excitation (Figure 4.1(b)) a charm (anti-)quark from a $g \to q\bar{q}$ splitting in

the proton is given a large momentum by the photon, and consequently cannot recombine with its antiparticle. This excitation can only occur if $Q^2 \gg m_c^2$.

In photoproduction the photon can fluctuate into a $q\bar{q}$ pair which can then interact with the proton (Figure 4.1(c)). These resolved-photon contributions are not relevant to this thesis as we are considering only DIS.

Charm quarks can also result from the decay of b quarks. The beauty cross section is strongly suppressed relative to that for charm because of the greater mass and smaller charge. The suppression factor for typical Q^2 values at HERA is ~ 50.

Charm can also be produced not in the hard scatter but in the subsequent fragmentation (see Section 4.4). This was observed at LEP [28] in hadronic Z^0 decays (i.e. $Z^0 \to q\bar{q}g, g \to c\bar{c}$) at the 2% level; because of the lower energy of jets at HERA this effect is expected to be smaller.

The figure originally located here has been removed from this electronic version of the thesis for copyright reasons.

Figure 4.1: Feynman diagrams of charm production mechanisms. The thick solid line corresponds to a charm quark or antiquark. From [29].

4.2 QCD Evolution

There are a number of ways in which the charm quark is treated in the perturbative QCD calculation. If carried out to all orders these would be equivalent, but in practice only

the first few terms can be calculated, which leads to very different results in different kinematic regions.

In the Fixed Flavour Number (FFN) scheme the number of active quark flavours in the sea is fixed for all values of Q^2, usually at three (u, d, s). These quarks are assumed to be massless, and contribute to the evolution of the strong coupling constant α_s, and the proton structure function. Charm quarks can only be produced dynamically in a BGF interaction. This scheme is expected to be most accurate around $Q^2 \sim 4m_c^2$. FFN schemes also exist with charm as a fourth active flavour for all Q^2. Because this assumes the charm quark is massless it is only accurate at high Q^2.

In the Zero-Mass Variable-Flavour-Number (ZMVFN) scheme the charm quark is treated as an active (but massless) flavour in the sea only above the threshold $Q^2 > m_c^2$. This scheme provides a good description of charm production for $Q^2 \gg m_c^2$, but is obviously less accurate for $Q^2 \sim \mathcal{O}(m_c^2)$.

In the General-Mass Variable-Flavour-Number (GMVFN) scheme charm quarks are treated as massive when $Q^2 \sim m_c^2$ but as massless when $Q^2 \gg m_c^2$. This scheme can therefore provide valid predictions for the whole kinematic range. Two versions of this scheme exist, that of Aivazis, Collins, Olness and Tung (ACOT) [30] and that of Thorne and Roberts (TR) [31].

4.3 Charm Structure Function

By analogy with Eq. 3.17 we can express the charm production cross section in terms of the charm structure function of the proton, $F_2^{c\bar{c}}$:

$$\frac{\mathrm{d}^2\sigma^{c\bar{c}}}{\mathrm{d}x\mathrm{d}Q^2} = \frac{2\pi\alpha^2}{xQ^4}\Big[\Big(1 + (1-y)^2 F_2^{c\bar{c}}(x,Q^2)\Big) - y^2 F_L^{c\bar{c}}(x,Q^2)\Big]. \tag{4.1}$$

As for Eq. 3.17 this equation considers only photon exchange, so that there is no term in $xF_3^{c\bar{c}}$. The longitudinal structure function is expected to be small, with the result that $F_2^{c\bar{c}}$ can be obtained from the measured charm cross section. Since charm production at HERA is dominated by BGF the charm structure function can be related to the gluon

density of the proton. $F_2^{c\bar{c}}$ can be *factorised* into the cross section for the boson–gluon fusion process, $\hat{F}_2^g(x, Q^2/\mu_F)$ which is calculable with perturbative QCD, and the gluon density of the proton, $g(x)$:

$$F_2^{c\bar{c}}(x, Q^2) = g(x, \mu_F) \otimes \hat{F}_2^g\left(x, \frac{Q^2}{\mu_F}\right). \tag{4.2}$$

The *factorisation scale*, μ_F, is the value of Q^2 chosen to separate the non-perturbative effects contained in the gluon density from the hard scattering of the BGF interaction.

Another important scale is the *renormalisation scale*, μ_R. In perturbative QCD higher-order terms in the expansion lead to divergences in observables such as cross sections because of (e.g.) the integration over infinite momenta in virtual loops in the corresponding Feynman diagrams. This can be solved by the application of an appropriate *renormalisation scheme*, however doing so introduces a new parameter, μ_R. Since this parameter is arbitrary and unphysical, physical observables cannot depend upon it. The result of this is that certain elements of the Lagrangian, such as coupling constants, become dependent upon the scale of the interaction, i.e. $\alpha_s \to \alpha_s(Q^2)$ (for further details see [32]).

If calculations are carried out to all orders the result is independent of the renormalisation and factorisation scales, however for calculation at finite orders the result does depend on the choice of scale. Therefore 'natural' values for μ_F and μ_R are chosen (i.e. reflecting the typical momenta involved) so that the effects of uncalculated higher-order terms are small.

4.4 Fragmentation

While charm production can be calculated perturbatively, the *fragmentation* process by which hadrons are formed from the charm quark cannot. This results in the need to use phenomenological models, such as that of Peterson [33]. An outgoing charm quark can easily form a meson by picking up an antiquark of similar velocity. The resulting hadron has a fraction z of the quark's initial momentum, with a probability governed by the

fragmentation functions $D_H(z)$. The Peterson fragmentation function is given by

$$D_H(z) = \frac{N}{z(1 - 1/z - \epsilon_P/(1-z))^2}. \tag{4.3}$$

N is the normalisation factor, determined by the momentum sum rule $\sum_H \int_0^1 D_H(z)\mathrm{d}z = 1$, where the sum is over all hadrons H containing the charm quark. ϵ_P is the only free parameter in the model, and is determined from fits to experimental data. Since the momentum of the quark is not known z has to be approximated by some other combination of variables.

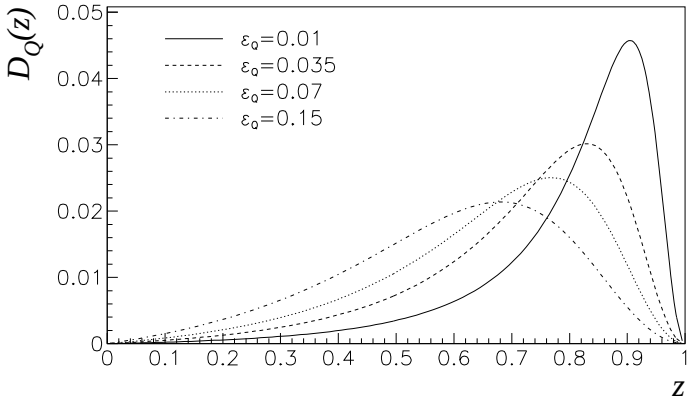


Figure 4.2: The Peterson fragmentation function, for different values of the parameter ϵ_P.

The form of the Peterson function for different values of ϵ_P is shown in Figure 4.2. The Peterson function peaks at $1 - 2\epsilon_P$ and has a width of $\mathcal{O}(\epsilon_P)$, thus a higher value of ϵ_P corresponds to a softer momentum spectrum for the hadrons. For the calculation of theoretical cross sections in this thesis a value of $\epsilon_P = 0.072 \pm 0.014$ is used [34]. This comes from a recent measurement at ZEUS, which is shown in Figure 4.3. Previous analyses have used $\epsilon_P = 0.035$ which was obtained from an NLO fit to ARGUS data [35]. This assumed that fragmentation is universal, that is, it is independent of the type of particles interacting in the hard collision. This is justified by the results of several experiments ($e^+e^-, \gamma p, e^{\pm}p$) which are in good agreement with each other (see e.g. [36, 37]).

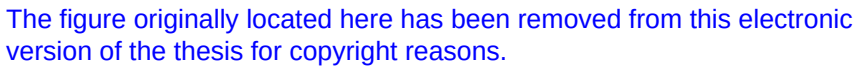


Figure 4.3: Results of a fit to the hadron momentum spectrum in ZEUS data to determine the best value of the Peterson parameter ϵ_P. [34]

Chapter 5

Monte Carlo and Theoretical Predictions

In order to be able to compare our results to theoretical predictions or results from other experiments it is necessary to compensate for all detector effects such as acceptance, efficiency and resolution. This is done in two steps: the first is to simulate the ep interaction. This is done with Monte-Carlo event generators. These simulate the hard interaction, and subsequent fragmentation and hadronisation. The output is a set of four-momenta describing the final-state particles. The second step is to pass the four-vectors through a GEANT-based [38] simulation of the ZEUS detector. This takes care of the interactions of the particles with the matter of the detector, ionisation, multiple scattering, decays of certain particles (e.g. K_s^0), etc., and gives output substantially similar to that coming from the readout electronics of the detector. As well as allowing us to correct for detector effects Monte Carlo simulations are also useful for optimising selection criteria, since they contain the "truth" information about each particle.

Once all the corrections have been applied to the experimental result, it is desirable to be able to compare this to our current theoretical understanding. For this thesis the program HVQDIS [39] is used, which gives predictions at next-to-leading order (NLO).



Figure 5.1: Schematic of a boson–gluon fusion event showing the different elements of the simulation performed by a Monte Carlo event generator (see text). ME indicates *matrix element*, PS *parton shower*. From [40]

5.1 Monte Carlo

The simulation of an event by a Monte Carlo event generator can be broken up into several steps, as illustrated for the case of boson–gluon fusion in Figure 5.1.

The matrix element for the interaction between the parton and the boson (labelled ME in the figure) is calculated perturbatively. The experimentally determined parton density function are used as input.

The parton and boson can radiate gluons or photons before and after the hard interaction. In addition the gluons can themselves radiate, as they carry colour charge. Such initial or final state radiation, or *parton showers*, labelled PS in the figure, are calculated as a perturbative correction to the hard scattering.

The partons must then be converted into hadrons (*hadronisation* or *fragmentation*). This involves soft QCD processes which cannot be calculated perturbatively; instead phenomenological models are used. Experimental measurements of branching ratios, decay probabilities and particle spectra are used for the subsequent decay of the hadrons.

The interacting partons carry only a fraction of the momentum of the proton. The rest of the proton, the *proton remnant* or *beam remnant*, carries a colour charge and so will interact with the hadrons produced in the hard interaction. The remnant's

hadronisation is therefore also taken into account.

5.1.1 Inclusive DIS Monte Carlo

DJANGOH 1.1 [41] was used to generate inclusive Neutral Current DIS events, thus simulating both signal and background. Since it showed better agreement with the data for the event variables (see Figure 8.1) than RAPGAP (Section 5.1.2), it was used as the default for calculating acceptances for the cross sections.

DJANGOH incorporates the generator LEPTO 6.5.1 [42], which simulates the lepton-parton hard interaction at leading order, and also an interface to HERACLES 4.6.1 [43], which calculates the electroweak radiative corrections.

ARIADNE 4.12 [44] is used to calculate the parton shower, using the *colour dipole model*. Emission of a gluon can be treated as radiation from the colour dipole comprised of the interacting parton and the proton remnant. The emission of a second, softer, gluon can be treated as radiation from two independent dipoles, one between the gluon and the parton, and the other between the gluon and the remnant. Emission of a third gluon can be treated as radiation from three dipoles, and so on. This process continues until the dipoles reach a certain minimum energy.

The fragmentation is carried out via the Lund string model [45] implemented in JETSET 7.408 [46]. Partons are treated as connected by *colour strings*. As the partons move apart the potential energy of the string increases, until it is energetically favourable to produce a $q\bar{q}$ pair in the middle of the string, thus breaking it in two. The daughter strings continue to fragment in this manner until they no longer have sufficient energy; a hadron is then formed from the quarks or diquarks at the ends of the string.

The DJANGOH Monte Carlo sample used was generated with a virtuality cut of $Q^2 > 4\,\mathrm{GeV}^2$ and had an integrated luminosity of $128\,\mathrm{pb}^{-1}$. Version num05t0.2 of the ZEUS detector simulation was used. A smaller sample with $Q^2 > 1.5\,\mathrm{GeV}^2$ was used to correct for the effects of Monte Carlo events with true Q^2 greater than the analysis cut of $5\,\mathrm{GeV}^2$ being reconstructed with Q^2 less than this value.

5.1.2 Charm Monte Carlo

RAPGAP 3.00/00 [47] was used to generate $c\bar{c}$ DIS events using only the boson–gluon fusion process. HERACLES 4.6.1 was again used for the radiative corrections, ARIADNE 4.03 for the parton showers, and the Lund string model for fragmentation as implemented in PYTHIA 6.221 [46]. The CTEQ5L [48] set of parameterisations of the proton structure functions was used.

RAPGAP Monte Carlo was used to obtain the signal distributions for use in the discriminant method (Section 9.3). It was also used instead of DJANGOH to extract the cross section as a systematic check.

The RAPGAP Monte Carlo sample used was generated in several different Q^2 ranges and reweighted to the $Q^2 > 4\,\mathrm{GeV}^2$ range to give a luminosity of $275\,\mathrm{pb}^{-1}$. The sample was processed with version num05t0.1 of the ZEUS detector simulation, and the same correction for low-Q^2 migrations applied as for DJANGOH.

5.2 HVQDIS

The HVQDIS program [39] calculates kinematic distributions for heavy quark production in DIS (i.e. differential cross sections) at next-to-leading order (NLO) using the fixed flavour number scheme. It does not generate individual events like a Monte Carlo generator, so detector and trigger simulations cannot be applied to its output. Instead the MC is used to correct the data, which can then be compared to HVQDIS calculations.

Chapter 6

Event Reconstruction

6.1 Kinematic Variables

As mentioned in section 3.2 for a given centre-of-mass energy the kinematics of a collision are completely defined by two of Q^2, x and y. There are a number of different methods by which these variables can be reconstructed from experimentally-measured quantities. The methods used in this thesis are described in the following sections.

6.1.1 Electron Method

If the scattered electron from a NC event is detected, Q^2, x and y can be determined from the polar angle through which it is scattered, θ, its initial and final energies, E_e and E'_e, and the initial energy of the proton, E_p, as follows [49]:

$$Q^2_{el} = 2E_e E'_e(1+\cos\theta) \tag{6.1}$$

$$x_{el} = \frac{E_e}{E_p}\frac{E'_e(1+\cos\theta)}{2E_e - E'_e(1-\cos\theta)} \tag{6.2}$$

$$y_{el} = 1 - \frac{E'_e}{2E_e}(1-\cos\theta) \tag{6.3}$$

6.1.2 Jacquet–Blondel Method

The kinematic variables can also be determined using only information from the hadronic final state. This method was proposed by Jacquet and Blondel [50] for charged current events, where there is no electron in the final state. y_{jb} is also useful for photoproduction events, where the electron is lost down the beampipe.

$$y_{jb} = \frac{\sum_i (E^i - p_z^i)}{2E_e} \tag{6.4}$$

$$Q^2_{jb} = \frac{(\sum_i p_x^i)^2 + (\sum_i p_y^i)^2}{1 - y_{jb}} \tag{6.5}$$

$$x_{jb} = \frac{Q^2}{s y_{jb}} \tag{6.6}$$

The sum runs over all final state particles except the scattered electron. Since this includes neutral as well as charged particles the sum is usually carried out using calorimeter cells (or similar). If the electron has been identified (see section 6.2) the cells associated with it are removed from the sum. If an electron is present but has not been identified the cells cannot be excluded, resulting in a value of y_{jb} close to one. This can be used to exclude events with an unidentified electron.

6.1.3 Double-Angle Method

A third method involves using the polar angle of the scattered electron, θ_e, and of the hadronic system, γ, the so-called *double angle* method [49]. γ is defined by

$$\cos\gamma = \frac{(\sum_i p_x^i)^2 + (\sum_i p_y^i)^2 - (\sum_i (E^i - p_z^i))^2}{(\sum_i p_x^i)^2 + (\sum_i p_y^i)^2 + (\sum_i (E^i - p_z^i))^2}, \tag{6.7}$$

and the kinematic variables are given by

$$Q^2_{DA} = 4E_e^2 \frac{\sin\gamma(1+\cos\theta)}{\sin\gamma + \sin\theta - \sin(\theta+\gamma)} \tag{6.8}$$

$$x_{DA} = \frac{\sin\theta(1-\cos\gamma)}{\sin\gamma + \sin\theta - \sin(\theta+\gamma)} \tag{6.9}$$

$$y_{DA} = \frac{E_e \sin\gamma + \sin\theta + \sin(\theta+\gamma)}{E_p \sin\gamma + \sin\theta - \sin(\theta+\gamma)}. \tag{6.10}$$

6.2 Electron Finding

As can be seen from the previous section, measurement of the scattered electron in a NC DIS event is important for reconstructing the kinematic variables. A number of software routines to identify the electron have been written for the ZEUS experiment; the one used in this thesis is the EM electron finder [51]. This uses a detailed parametrisation of the detector response for electrons to assign a probability that a calorimeter cluster comes from the DIS electron. Seven different variables are used (the last three are only used if the candidate lies within the tracking detector acceptance):

- The fraction of the energy in the HAC layers (excluding HAC0; see section 2.2.3)
- The fraction of EMC energy outside the two highest energy EMC cell strips (if the four EMC cells in a tower (see Figure 2.13) are numbered one to four, a *cell strip* is defined as all EMC cells in the same module with the same EMC cell number)
- The fraction of energy outside the two highest energy modules
- The energy not assigned to the candidate cluster which lies within an $\eta\phi$ cone of radius 0.8 centred on the candidate.
- The difference in polar angle between the cluster and the track pointing to the cluster, $|\theta_{Trk} - \theta_{CAL}|$
- The difference in azimuthal angle between the cluster and the track pointing to the cluster, $|\phi_{Trk} - \phi_{CAL}|$
- The difference $|1/P - 1/E|$; $1/P$ is proportional to the radius of curvature of the track, and in the relativistic limit $E \simeq p$

The distribution of each of these variables is parameterised separately for the three calorimeter sections (FCAL, BCAL, RCAL). The parametrisation is used to give a sub-probability for each variable that the cluster is the DIS electron. The sub-probabilities are then combined to give a grand probability for the cluster to be the DIS electron.

6.3 Track and Vertex Reconstruction

The trajectories of charged particles are reconstructed from the hits they make in the tracking detectors. For this thesis tracks were restricted to the central region of the detector, so only the CTD and MVD were used.[1] The reconstructed tracks are then used to determine the position of the *ep* vertex.

6.3.1 Track Reconstruction

Track reconstruction begins with the track finding, or pattern recognition, step. Track segments are formed, consisting of hits on at least three wires in a cell in the CTD, or clusters in three layers/wheels in the MVD. A track segment in the outermost superlayer is selected as a *seed*, and extrapolated inwards to find hits in the next axial superlayer. A circle fit in the xy plane is used to find the hit which best matches the existing trajectory. This hit is added, the track parameters updated, and the next hit sought. This extrapolation continues in the axial superlayers (1,3,5,7 and 9) down to superlayer 1, and into the MVD if possible. The stereo superlayers are not used initially because the xy position of hits in these layers depends on the z coordinate. Whenever an axial hit with z-by-timing information is added to the track, a rough linear fit in the sz plane is updated (s is the pathlength along the circle). Once the track reaches SL1 (or the MVD) a linear fit in the sz plane is performed, using both the z-by-timing data and the hits in the stereo layers, with the rough sz fit as the starting point. The pattern recognition then repeats for all segments in SL9, then those in SL7 and so on, for all axial superlayers. Tracks which are subsets of a longer track are excluded, and those which share more than 15% of their hits with another track are regularly pruned. A number of passes are performed in order to account for all hit topologies, and to assign to tracks hits which are left over after the strongest candidates have been formed.

Once the pattern recognition stage is complete the part of the track within the CTD is

[1] The STT has recently been integrated into the track reconstruction software from the pattern recognition stage. As it was not used in this thesis this is omitted from the following discussion, for simplicity.

fit with a five-parameter helix. The processing up to this point is done by the VCTRAK package [52], and such tracks are known as REG tracks. The tracks are then passed to the KFRECON package [11]. This uses a Kalman Filter algorithm to fit the portion of the track inside the MVD (if any), taking into account energy loss and multiple scattering in the material of the beampipe and the detector. These tracks are known as ZTT tracks.

After tracks have been assigned to vertices (see section 6.3.2) they can be refitted with the constraint that the track helix must pass through the vertex position. These refitted tracks give the most accurate estimate of the particle's trajectory.

6.3.2 Vertex Reconstruction

Once the tracks have been reconstructed they can be used to determine the location of the *ep* collision, the *primary vertex*. *Secondary vertices* can also be reconstructed from tracks which do not originate from this vertex, for example those coming from decays of particles produced in the *ep* interaction, or those coming from interactions in the material of the detector. Both VCTRAK and KFRECON have vertexing modules which can and have been used to perform the vertex finding and fitting. Recently a new algorithm based on a deterministic annealing filter (DAF) [53] has been developed for ZEUS; this has been used for the primary vertex reconstruction in this thesis. A comparison of the different vertexing algorithms can be seen in Figure 6.1.

The DAF algorithm begins by taking the tracks assigned to the primary vertex by VCTRAK. It gets the ZTT tracks corresponding to these REG tracks, and performs a fit using the method described in [54], with the addition of a weighting factor for each track (for this step the weight is set to one). The average beam position (the *beamspot*) may be used to constrain the fit. The χ^2 of the vertex fit is calculated from the (weighted) sum of the χ^2 values from the tracks. The tracks are then required to come from the vertex resulting from the fit, and their momenta and covariances updated. The result is used as the starting point for the subsequent iterations.

Four iterations are performed, each at a different value of a parameter, T, known as the temperature (it is the reduction of the temperature which leads to the name

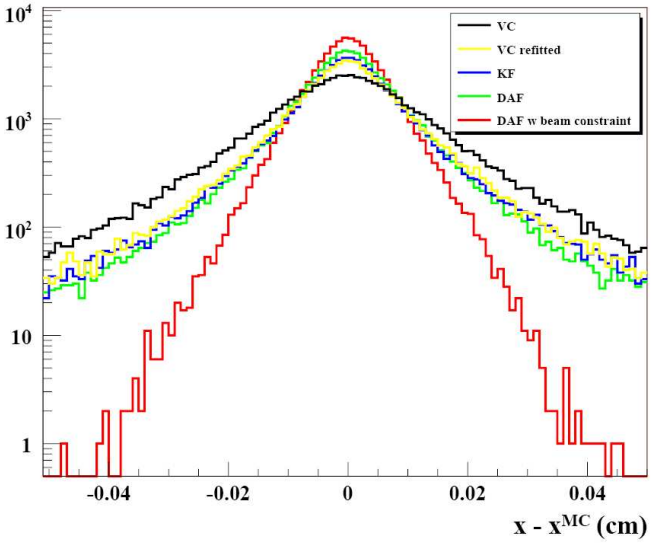


Figure 6.1: Plot showing comparison of DAF vertexing with other vertexing algorithms

annealing). Each track is assigned a weight which depends on its contribution to the χ^2 of the vertex fit and the temperature, T:

$$w(\chi^2, T) = \frac{1}{1 + \exp(\frac{\chi^2 - \chi^2_{cut}}{2T})} \tag{6.11}$$

A constrained fit is then performed as above, but using the new weights. The tracks are refit, their weights updated, and the temperature lowered. After the final temperature is reached the vertex fit is performed again.

The weight function for the values of T and χ^2_{cut} used is shown in Figure 6.2. The fact that the weights lie somewhere between zero and one means that the tracks are not definitely assigned to the vertex.

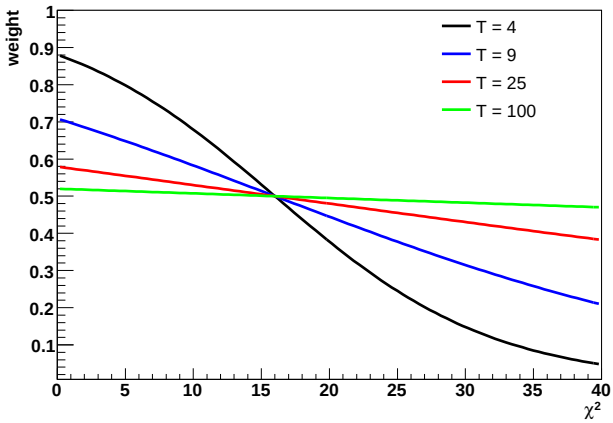


Figure 6.2: The weight function $w = 1/(1 + \exp((\chi^2 - \chi^2_{cut})/2T))$ shown for the values of T used in the DAF algorithm. $\chi^2_{cut} = 16$.

Chapter 7

$D^{*\pm} \rightarrow D^0\pi^{\pm}$ Studies

As the object of this thesis is to exploit the capabilities of the MVD to provide better measurements of charm production, a logical first step is to investigate its performance in events which have been independently determined to contain a charm hadron. This was done using the preferred HERA-I method for studying charm, the decay $D^* \rightarrow D^0\pi \rightarrow K\pi\pi$, the so-called 'golden decay mode'. This channel is favoured because, in addition to having only charged particles in the final state, the mass of the D^* is only just above the threshold for the decay to $D^0\pi$. The restricted phase space means that the invariant-mass difference $\Delta M = m_{D^*} - m_{D^0}$ gives a signal with lower combinatorial background than simply considering the D^0. As the pion has a low momentum in both the centre-of-mass and laboratory frames it is often referred to as the "slow pion", and denoted π_s.

7.1 D^* Reconstruction

D^0 candidates are found by looping over all oppositely charged track pairs which satisfy the following selection criteria:

- $p_T(\text{track}) > 0.4\,\text{GeV}$
- $|\eta(\text{track})| < 1.75$
- Tracks are assigned to the primary vertex

- The outer superlayer of each track is ≥ 3

The transverse momentum cut and primary vertex assignment[1] reduce the combinatorial background, the pseudorapidity and superlayer cut ensure the track lies within the acceptance of the CTD and is well measured. Since no particle identification is performed the tracks are assigned both the K and π masses in turn. A D^* candidate is formed by combining the D^0 candidate with another track assigned the π mass (the π_s), subject to the following criteria:

- $1.80 < m_{K\pi} < 1.92\,\text{GeV}$
- Charge of π_s is opposite to K
- $p_T(\pi_s) > 0.12\,\text{GeV}$
- $|\eta(\pi_s)| < 1.75$
- π_s track is assigned to the primary vertex
- The outer superlayer of the π_s track is ≥ 3
- $1.5 < p_T(D^*) < 15\,\text{GeV}$
- $|\eta(D^*)| < 1.5$

The ΔM spectrum obtained by this method for $120\,\text{pb}^{-1}$ of data taken in 2005 is shown in Figure 7.1. The peak corresponding to the D^* mass can be clearly seen. There are two methods for estimating the number of candidates in the peak. The first is by fitting the distribution. A functional form commonly used in ZEUS D^* analyses is

$$F = p_1 \exp\left(-0.5\, x^{1+\frac{1}{1+0.5x}}\right) + p_4(\Delta M - m_\pi)^{p_5} \tag{7.1}$$

where

$$x = \left|\frac{(\Delta M - p_2)}{p_3}\right|, \tag{7.2}$$

[1]The tracks should in fact come from a secondary vertex; see Section 7.2 for further discussion.

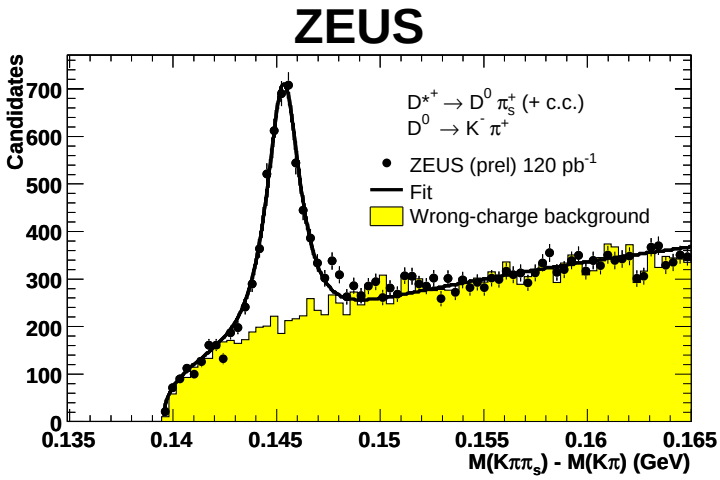


Figure 7.1: Plot showing the invariant-mass difference spectrum for the decay $D^* \rightarrow D^0\pi \rightarrow K\pi\pi$. The black dots correspond to right-charge candidates from data, the solid histogram to wrong-charge candidates (normalised to the data in the region $(0.15, 0.165)$ GeV) and the solid line is a fit to the points.

and $p_1 - p_5$ are the parameters of the fit. The first term of Eq. 7.1 is a modified Gaussian; this gives a better χ^2 for the fit than the standard Gaussian. The second method is to use background subtraction. The background is estimated by forming *wrong-charge* D* candidates. The procedure is the same as described above for right-charge candidates, with the exception that the D^0 candidate is made up of two tracks of the same charge. The wrong-charge ΔM distribution is normalised to the right-charge distribution in the region away from the peak, $(0.15, 0.165)$ GeV; the difference between the two distributions in the interval $(0.143, 0.148)$ GeV is then taken as the number of D^* candidates. The number of candidates obtained via this method for the distribution shown in Figure 7.1 is 2777 ± 90, while the fit gives 3005 ± 95 candidates.

7.2 Secondary Vertex

Having obtained a D^* sample, one can then look at whether the MVD identified the D^* candidate as originating in a charm decay. The most obvious indication of this would be the explicit reconstruction of the D^0 decay vertex. In the method described

in the preceding section, all the tracks comprising the D^* candidate are required to be associated by the vertexing algorithm[2] with the primary vertex. This requirement stems from the HERA-I analysis, when the vertex resolution was poorer. While this remains a good approximation for the π_s, since the D^* has a lifetime of only $\sim 10^{-25}$ sec, the decay products of the D^0 should be separated from the primary vertex by around $\mathcal{O}(100\,\mu\text{m})$ (the mean lifetime of the D^0 according to the PDG is $c\tau \sim 123\,\mu$m.[1]), which should be within the resolution of the MVD. However, the fact that a strong signal is obtained with the primary vertex requirement, despite the fact that the MVD hits were used in the track reconstruction, indicates that the vertexing algorithm is still assigning the tracks from charm decays to the primary vertex. The reason for this is that the algorithm is designed to give the best estimate of the primary vertex position; tracks which originate within a few hundred microns of the primary vertex are sufficiently consistent with the hypothesis that they come from the vertex, and are hence assigned to it.

To obtain the full benefit of the increased precision of the MVD it is therefore necessary to supply additional information to the vertexing algorithm, namely which tracks should come from a D^0 vertex. The vertexing package `vxlite` was used to perform this revertexing "on the fly", i.e. for each D^0 candidate during the loop over candidates. A two-track vertex was formed from the D^0 candidate decay products; the same two tracks were removed from the primary vertex, and the remaining tracks refitted to give a *reduced primary vertex*. In both cases the vertex fit used the algorithm of [54]. This procedure will always produce a secondary vertex (albeit with a very large χ^2 for incompatible tracks), so one cannot use its presence as an indication of charm. Instead one needs to look at the distance between the primary and secondary vertex, the *decay length*. The signed decay length, L, can be defined as:

$$L = (\boldsymbol{S} - \boldsymbol{P}) \cdot \boldsymbol{J} \tag{7.3}$$

where $\boldsymbol{P}$ and $\boldsymbol{S}$ are the vectors to the primary and secondary vertices, and $\boldsymbol{J}$ is the

[2]This study was carried out before the advent of the DAF vertex algorithm. The primary vertex algorithm used in this section is that of KFRECON.

momentum of the particle decaying at the secondary vertex, in this case the D^0. This definition takes the projection of the decay length onto the direction of flight of the candidate, to remove phase space effects (without this the distribution drops to zero at a decay length of zero). The dot product also defines a sign: the decay length is positive if the angle the momentum vector makes with that from the primary to the secondary vertex is less than 90°, and negative otherwise. The physical case, where the secondary vertex is the result of a particle decay, corresponds to the positive sign; random combinations of tracks are equally likely to give positive or negative decay lengths.

Figure 7.2 shows the 3D and 2D decay length distributions for the right-charge candidates in the D^* peak, ($\Delta M \in (0.143, 0.148)\,\mathrm{GeV}$), of Figure 7.1 (black circles) and also for the wrong-charge candidates under the peak (blue squares). The right-charge distribution is background-subtracted, that is, it has had the wrong-charge distribution subtracted from it. The wrong-charge distribution has been scaled to have the same number of events as the right-charge. The curves shown are a fit to the points with the sum of two gaussians. This functional form is not strictly correct; a more correct form would be the convolution of a decaying exponential (corresponding to the distribution with no measurement error) with a gaussian (corresponding to the resolution of the detector). However the double gaussian fit used provides a not unreasonable description for illustrative purposes and for obtaining an estimate of the resolution.

The wrong-charge distribution is symmetric about zero. This is expected, as it does not contain any real D^0's. The right-charge distribution is shifted in the positive direction, which suggests the presence of real particle decays, however it also has a significant number of negative entries. This is probably due to the finite resolution of the detector.

The width of the decay length distribution depends on the error on the two vertices. Therefore to have the best estimate of the decay length one needs to have the best measurement of the vertex positions. Since the orbit of the beams must remain stable from event to event for collisions to keep occurring one can obtain a more accurate estimate, compared to the (reduced) primary vertex, by averaging the primary vertex positions over several thousand events within a fill. This average beam position is often

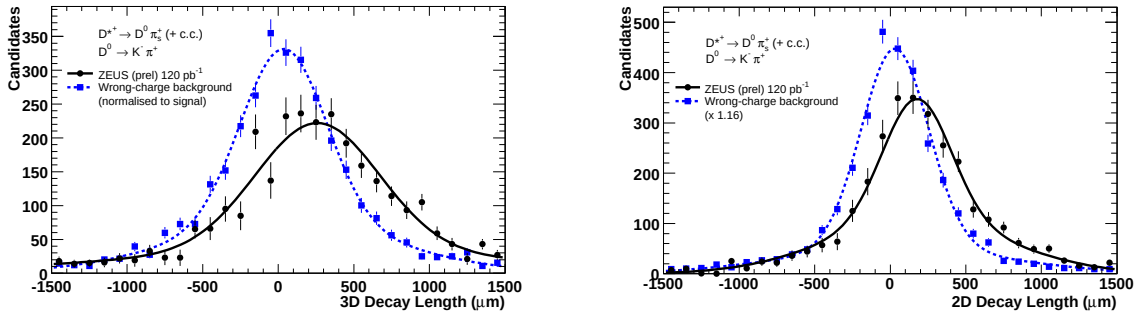


Figure 7.2: Plot showing (a) the 3D decay length of the D^0 with respect to the primary vertex (b) the decay length projected onto the xy plane.

called the *beamspot*. However the beamspot is only more accurate in the xy plane; the z coordinate of the primary vertex for the event is more accurate than the average z. This is because the bunches of electrons and positrons are $\sim 10\,\text{cm}$ long in z, but have nominal values of $120\,\mu\text{m}$ in x and $30\,\mu\text{m}$ in y. Thus to take advantage of the beamspot one must consider the projection of the decay length onto the xy plane. Using the beamspot also reduces the CPU time for the analysis as the reduced primary vertex does not need to be calculated for every D^* candidate.

7.3 Decay Length Cut

To further confirm that the excess of positive decay lengths among the right-charge D^0 candidates corresponds to real D^0's, one can look at the D^* mass-difference spectrum after applying a cut on the decay length. The signal to background ratio should improve if in fact the candidates with larger positive decay length are real. Table 7.1 shows the results of decay length cuts for the D^* candidates in the peak of Figure 7.1. The signal to background ratio increases as the minimum decay length increases, up to approximately $700\,\mu\text{m}$; this is consistent with a decrease in the background coming from random combinations of tracks from the primary vertex, which are removed as the separation of the primary and secondary vertices increases. After about $700\,\mu\text{m}$ the ratio begins to decrease. This behaviour is consistent with real D^0 decays, which fall off exponentially

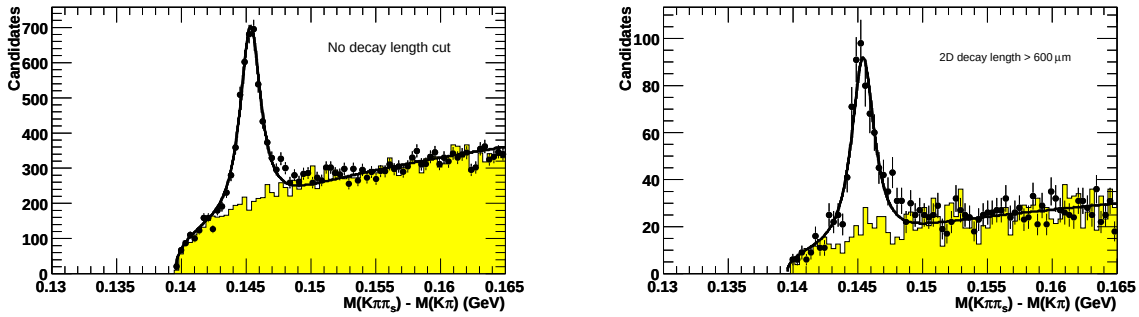


Figure 7.3: Plot showing the D^* mass difference distribution with (a) no decay length cut, and (b) a cut on the decay length projected onto the xy plane of 600 μm.

with distance. Figure 7.3 shows the D^* mass distribution with no cut, and with a cut of 600 μm. The improvement in signal to background can be clearly seen, illustrating that the MVD can indeed be used to improve the charm signal, however the factor ~ 2 improvement is balanced by a factor ~ 6 drop in the number of D^* candidates. Since this decay channel already had a strong signal it is unlikely such a decay length cut would be used here, however other channels may benefit from this or similar methods.

Decay Length Cut (μm)	No. of D^*'s	Signal/ Background
No cut	2945±93	1·01
-200	2459±84	1·08
-100	2311±79	1·16
0	2048±72	1·30
100	1731±64	1·49
200	1384±55	1·68
300	1069±47	1·78
400	835±41	1·98
500	622±35	1·97
600	496±31	2·01
700	392±28	2·05
800	302±25	1·79
900	241±23	1·63
1000	193±21	1·49
1500	71±15	0·87

Table 7.1: Number of D^* candidates found after different cuts on the decay length of the D^0 candidate.

Chapter 8

$D^0 \to K^0_S \pi^+ \pi^-$ Decay Channel

8.1 Motivation

As discussed in the previous chapter, at present additional information needs to be supplied in order to make the most of the greater precision of the MVD; in practice this means making charmed hadron candidates from tracks which satisfy kinematic requirements, and performing revertexing for each candidate. This is quite CPU intensive and is also susceptible to large combinatoric backgrounds. The optimal solution seems to be to choose a decay mode where there is some additional way of tagging the particles involved, much like the slow pion for the D^* golden decay mode. A prime candidate is decays involving a K^0_s in the final state. The K^0_s typically travels a few centimetres from the primary vertex before decaying, so can be reconstructed with relatively little background. Although the inclusive branching ratio of charmed hadrons for decay to $\overleftrightarrow{K^0}$ is high (for some hadrons as much as $\sim 50\%$) because of the high probability for a charm quark to decay to a strange one, the rates for specific channels are lower. Nevertheless they are still competitive with the commonly-studied decay channels, and indeed can provide an independent cross-check of them.

The first such channel studied was

$$D^0 \to K^0_s \pi^+ \pi^-. \tag{8.1}$$

Initially it was planned to investigate only the submode

$$D^0 \to K^0_s \rho^0 \to \pi^+\pi^-\pi^+\pi^-, \tag{8.2}$$

using the ρ to constrain the pions not coming from the K^0_s. However it proved too difficult to obtain a ρ signal above the combinatorial background, and so the more general $K^0_s\pi^+\pi^-$ mode was used instead. This had the advantage of approximately doubling the branching ratio, most of this coming from the channel

$$D^0 \to K^{*+}\pi^- \to K^0_s\pi^-\pi^+. \tag{8.3}$$

For this and the other channels studied in this thesis only DIS events were used. Although the cross section for photoproduction is larger, DIS events are easier to identify and trigger on, due to the presence of the scattered electron. Time constraints for this thesis prevented both DIS and photoproduction regimes being investigated.

8.2 Trigger Selection

Data events were required to pass the third level triggers SPP01, (SPP02 OR SPP09), or HFL02. Monte Carlo events were required to pass the same triggers in the trigger simulation. The combination of trigger slots SPP02 and SPP09 is due to the fact that in 2006 SPP02 was prescaled by a factor of ten (that is, only every tenth event which fired the trigger was accepted) as part of an effort by the collaboration to reduce the overall trigger rate and hence the data volume. At the same time as this occurred however, a new trigger, SPP09, was turned on which was not prescaled, but achieved a lower rate by increasing the so-called 'boxcut'. This cut rejects events where the DIS electron is found within a rectangular region at the centre of the RCAL. (This region also contains the hole for the beampipe.) Such electrons have a small scattering angle and hence a small Q^2. Since the cross section is proportional to $1/Q^4$ removing low-Q^2 events via the boxcut can significantly decrease the trigger rate. Taking the OR of these two triggers

and using the larger boxcut for both compensates for the prescaling of SPP02 while retaining stable trigger logic over the whole dataset used. The requirements of each of the triggers are given below.

- TLT slot SPP01:
  - FLT:
    - OR of several DIS triggers, mainly based on energy deposits in the various regions of the CAL or the presence of tracks of a given quality, with vetos from the C5 counter, 3 m and 6 m taggers or the Veto wall
  - SLT:
    - Minimum energy deposits in various parts of the CAL
    - $E - p_z > 30\,\text{GeV}$
    - Energy of SLT electron $> 5\,\text{GeV}$
  - TLT:
    - $30 < E - p_z < 100\,\text{GeV}$
    - Energy of TLT electron $> 4\,\text{GeV}$
    - TLT electron position outside the circle of radius 30 cm centred at (0,0,0)
- TLT slot SPP02:
  - FLT:
    - OR of several DIS triggers, mainly based on energy deposits in the various regions of the CAL or the presence of tracks of a given quality, with vetos from the C5 counter, 3 m and 6 m taggers or the Veto wall
  - SLT:
    - Minimum energy deposits in various parts of the CAL
    - $E - p_z > 30\,\text{GeV}$
    - Energy of SLT electron $> 5\,\text{GeV}$

  - TLT:
    - $30 < E - p_z < 100\,\text{GeV}$
    - Energy of TLT electron $> 4\,\text{GeV}$
    - TLT electron position outside the rectangular region $(-12, 12)\times(-12, 12)$ cm centred at (0,0,0) (the *boxcut*)

- TLT slot SPP09:
  - FLT:
    - OR of several DIS triggers, mainly based on energy deposits in the various regions of the CAL or the presence of tracks of a given quality, with vetos from the C5 counter, 3 m and 6 m taggers or the Veto wall
  - SLT:
    - Minimum energy deposits in various parts of the CAL
    - $E - p_z > 30\,\text{GeV}$
    - Energy of SLT electron $> 5\,\text{GeV}$
  - TLT:
    - $30 < E - p_z < 100\,\text{GeV}$
    - Energy of TLT electron $> 4\,\text{GeV}$
    - TLT electron position outside the rectangular region $(-15, 15)\times(-15, 15)$ cm centred at (0,0,0)

- TLT slot HFL02:
  - FLT:
    - OR of several DIS triggers, mainly based on energy deposits in the various regions of the CAL or the presence of tracks of a given quality, with vetos from the C5 counter, 3 m and 6 m taggers or the Veto wall
  - SLT:

        * OR of several DIS triggers with various cuts on:
        * $E - p_z$
        * Energy of SLT electron
        * Vertex position
        * Minimum energy deposits in various regions of the CAL
        * Transverse energy of the the event
        * Track momentum
    - TLT:
        * Requires DIS electron
        * OR of Heavy Flavour meson triggers with loose cuts based on p_T of tracks

8.3 Event Selection

The following standard cuts were applied offline to select DIS events.

- $|Z_{vtx}| < 50\,\mathrm{cm}$
- EM electron candidate with grand probability > 0.001
- Electron energy $E_e > 10\,\mathrm{GeV}$
- $40 < E - p_z < 70$
- $y_{\mathrm{JB}} > 0.02$
- $y_{el} < 0.95$
- $5 < Q^2_{DA} < 1000\,\mathrm{GeV}^2$
- $0.02 < y_{DA} < 0.7$

The vertex cut ensures the majority of the decay products lie within the fiducial volume of the detector, and also excludes events triggered by showers from the C5 collimator. The electron candidate probability ensures that there is a strong electron candidate in

the event (recall that the grand probability is the combination of several variables, so the cut should not be interpreted as requiring the candidate to have a probability greater than 0.1% of being an electron.) The electron energy cut restricts the candidates to a region where the electron finder has high efficiency. The $E - p_z$ distribution is peaked at 55 GeV (twice the lepton beam energy), but has a tail towards lower values caused by photoproduction events and events with initial state radiation. The lower cut removes such events, the upper cut removes a small number of poorly reconstructed events. The y_{JB} cut eliminates events triggered by noise in the calorimeter. The y_{el} cut removes photoproduction events where another particle has been misidentified as a DIS electron. Since Q^2 is related to the angle of the scattered electron, the minimum value which can be reconstructed is determined by the size of the opening for the beam pipe. In HERA-II this minimum Q^2 has further increased because of the greater amount of dead material in the path of low-angle electrons. The Q^2_{DA} and y_{DA} cuts are part of the definition the kinematic region of interest, the remainder of the definition being the transverse momentum and pseudorapidity of the charmed hadron. Figure 8.1 shows the comparison of the data to both the DJANGOH and RAPGAP Monte Carlo for all the above variables and also x_{DA}. DJANGOH gives a better description of the data, so was chosen as the default Monte Carlo for acceptance corrections. RAPGAP was used instead as a systematic check.

8.4 K_s^0 Reconstruction

The K_s^0 candidates are reconstructed in the decay mode

$$K_s^0 \to \pi^+\pi^-. \tag{8.4}$$

All pairs of oppositely-charged tracks satisfying $p_T > 0.15\,\mathrm{GeV}$ and $|\eta| < 1.75$ with an outer superlayer ≥ 3 are considered. If the minimum distance of closest approach between the two helices is less than 0.4 cm the `vxlite` package is used to make a vertex from them (using the algorithm of [54]). If the χ^2/NDF of the resulting fit is less than

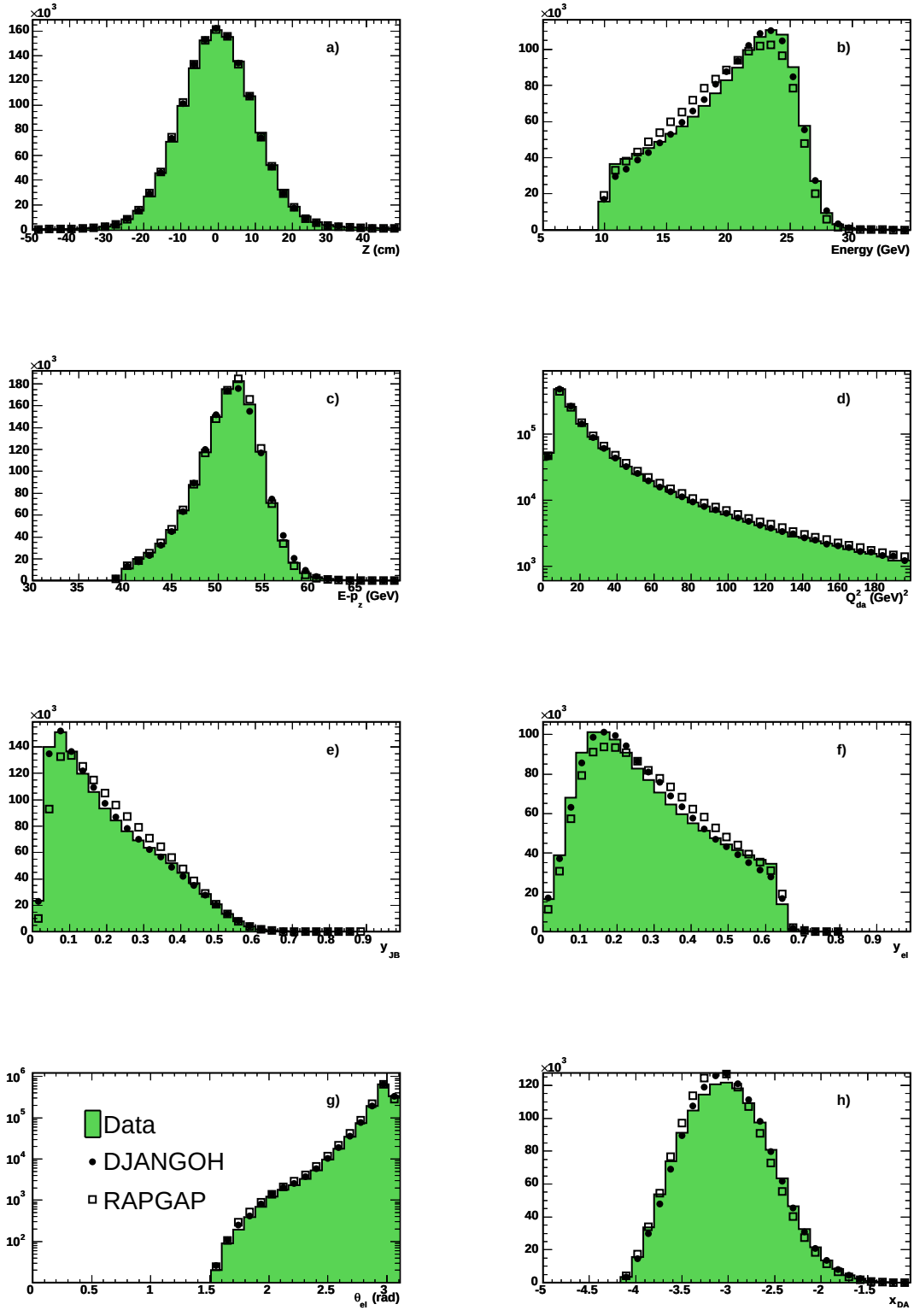


Figure 8.1: Plots comparing the data (solid histogram) to DJANGOH MC (filled circles) and RAPGAP MC (open squares) for a)Z vertex, b)Electron energy, c)$E - p_z$, d)Q^2_{DA}, e)y_{JB}, f)y_{el}, g)Electron angle, and h)x_{DA}. The Monte Carlo distributions are normalised to have the same number of events as the data.

5, the pion mass is assigned to both tracks and the invariant mass of the two-track combination calculated. The invariant mass is also calculated for the $\overleftrightarrow{\Lambda}$ hypothesis, i.e. that the tracks instead come from the decay

$$\overleftrightarrow{\Lambda} \to p^{\pm}\pi^{\mp}. \tag{8.5}$$

The proton mass is assigned to the track with the larger momentum, and the pion mass to that with the smaller momentum,[1] thus the (anti-)proton track's charge determines whether this candidate would be a Λ (positive charge) or $\overline{\Lambda}$ (negative charge). Finally the invariant mass is also calculated assigning the electron mass to both tracks; this corresponds to the hypothesis that the tracks come from the conversion of a photon to an e^+e^- pair. The two-track combination is then taken as a K_s^0 candidate if it satisfies the following invariant mass cuts:

- $0.47 < M(\pi\pi) < 0.52\,\text{GeV}$
- $M(p\pi) > 1.121\,\text{GeV}$
- $M(ee) > 0.05\,\text{GeV}$

A few further cleaning cuts are applied. The 2D distance of closest approach of each track to the beamspot must be greater than 0.05 cm, and the 2D DCA for the K_s^0 vertex from the beamspot is required to be greater than 0.2 cm. This reduces the number of combinations which include tracks coming from the primary vertex. (In HERA-I analyses the secondary vertices coming from the VCTRAK vertexing were used as the starting point for K_s^0 candidates; as noted previously these vertices were at least a few centimetres from the primary vertex as any track closer than this was assigned to the primary vertex. The MVD therefore allows us to reconstruct K_s^0's closer to the primary vertex, with a corresponding increase in efficiency.)

[1] Because the mass of the proton is much greater than that of the pion, it receives a greater momentum in the lab frame than the pion when the momentum of the Λ is greater than $\sim 0.3\,\text{GeV}$. Because of the momentum cuts on the pion and proton tracks this means the proton will have the larger momentum for all reconstructed $\overleftrightarrow{\Lambda}$.

A cut is also made on the collinearity. The collinearity angle is defined as the angle between the momentum vector of the K_s^0 (which is the vector sum of the momenta of the two tracks) and the vector from the K_s^0 production vertex to the K_s^0 decay vertex. For a real K_s^0 these should be almost parallel. In this thesis the beamspot (or in three dimensions the beamspot plus the z coordinate of the primary vertex) was used for the K_s^0 production vertex. Although this is not strictly correct, Monte Carlo studies showed that the effect for a collinearity cut was negligible. The K_s^0 candidate was required to satisfy $cos(\theta_{coll,2D}) > 0.99\,\text{rad}$ and $\theta_{coll,3D} < 0.3\,\text{rad}$.

The distance from the nominal centre of the detector to the secondary vertex is required to be less than 20 cm. Virtually all of the K_s^0's coming from the interaction region will have decayed by this point; the cut serves to reduce background from tracks coming from interactions in the material of the detector, and from poorly reconstructed tracks.

Finally the K_s^0 candidate itself is required to have a pseudorapidity in the range $|\eta| < 1.6$. No p_T cut is made on the K_s^0 in order to be able to measure the D^0 cross section down to very low p_T.

The K_s^0 mass distribution obtained after these cuts is shown in Figure 8.2. The data are fitted with the sum of two gaussians and a first-order polynomial, where the use of two gaussians is motivated by the expectation that momentum resolutions of the tracks will differ depending on whether or not they contain MVD hits. From the fit there are $918\,879 \pm 3100$ events in the peak, which is located at $(0.49504 \pm 0.00001)\,\text{GeV}$ and has a width of $(0.00558 \pm 0.00001)\,\text{GeV}$ (the mass and width are quoted for the dominant of the two gaussians). This value for the K_s^0 mass is slightly lower than the PDG value of $(0.497648 \pm 0.000022)\,\text{GeV}$ (although the weighted mean of the two gaussians is a little closer, at 0.49688 GeV). This is related to the momentum scale calibration, which in turn is related to how well the magnetic field is known. The current estimate of the uncertainty on the magnetic field measurement is $\pm 0.3\%$, which translates to a mass shift of $\pm 0.0015\,\text{GeV}$. The observed difference for the K_s^0 mass is thus $1-2\sigma$, which is not particularly significant. The measured values for the D^0 mass and also the $D^\pm$ and

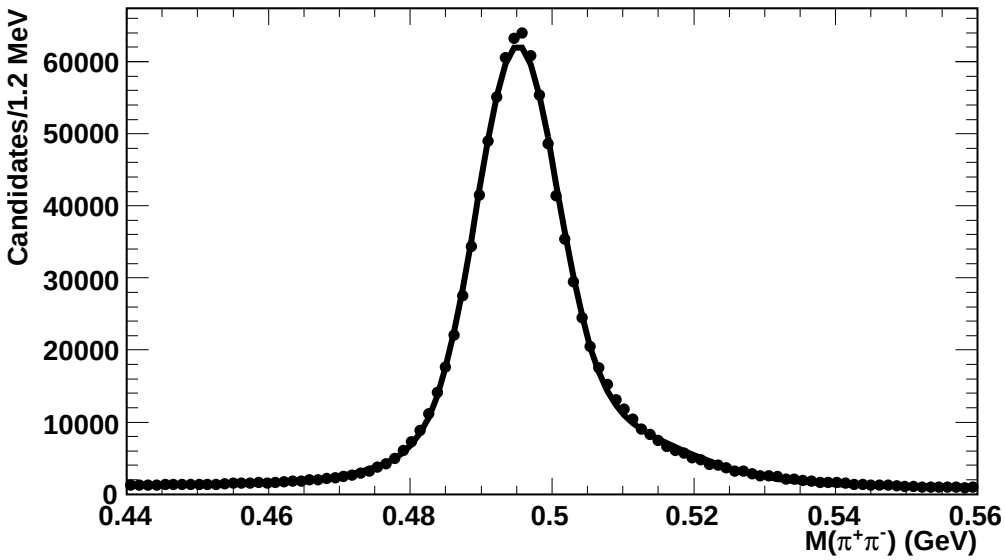


Figure 8.2: K^0_s mass peak. The points are the data, the solid line is a fit to the sum of two gaussians and a first order polynomial.

$D^\pm_s$ masses in Chapter 9 are likewise slightly lower than the PDG value, though they agree within twice the experimental uncertainty.

8.5 D^0 Reconstruction

All the D^0 decay modes which lead to a $K^0_s\pi\pi$ final state give rise to a single vertex from which all three particles originate. This is either because the D^0 decays directly to $K^0_s\pi\pi$, or because the decay goes via a resonance which decays strongly (K^*, ρ, ω), and thus travels a negligible distance. Since the K^0_s is neutral, this vertex therefore appears to be a two-track vertex. This means the two pion candidates can be reconstructed by a similar procedure to that used for the K^0_s candidates.

The $\pi\pi$ candidates are found by looping over all pairs of oppositely charged tracks which satisfy the following conditions:

- $p_T > 0.15\,\mathrm{GeV}$

- $|\eta| < 1.75$
- Outer superlayer ≥ 3
- Number of MVD hits ≥ 1

Unlike the K_s^0 decay products, these pions should all originate within the beampipe, hence must pass through the MVD.

If the distance of closest approach between the two tracks is less than 0.4 cm a vertex is formed from this track pair. If the χ^2/NDF of the vertex fit is less than 5, the invariant mass of the pair is calculated assuming the pion mass for both tracks. If the invariant mass satisfies $0.279 < M(\pi\pi) < 1.4\,\text{GeV}$ the pair of tracks is kept. The invariant mass cut corresponds to the constraints imposed by the masses of the particles involved.

D^0 candidates are then formed by looping over all the K_s^0 candidates, and for each K_s^0 candidate looping over all the $\pi\pi$ candidates. If any of the tracks are common to both candidates that combination is rejected. The four-momenta of the K_s^0 and the $\pi\pi$ pair are combined to give the invariant mass of the D^0 candidate. This candidate must then satisfy the following criteria:

- $1.7 < M(D^0) < 2.1\,\text{GeV}$.
- $\cos(\theta^*) < 0.8$ where θ^* is the angle between the K_s^0 momentum boosted into the D^0 rest frame and the D^0 momentum in the laboratory frame.
- $\cos(\theta_{coll,3D}) > 0.99$, where $\theta_{coll,3D}$ is the angle between the K_s^0 momentum vector and the vector joining the $\pi\pi$ vertex to the K_s^0 vertex.
- $d_\perp < 0.4\,\text{cm}$, where $d_\perp$ is the distance of closest approach of the K_s^0 trajectory (approximated as linear) to the $\pi\pi$ vertex.
- $1.0 < p_T(D^0) < 20.0\,\text{GeV}$
- $|\eta(D^0)| < 1.6$

θ^* is isotropic for real $D^0 \rightarrow K^0 s\pi^+\pi^-$ decays, but for the combinatorial background the distribution is strongly peaked at 1. As for the pions from a K_s^0 decay, the decay

products of the D^0 are subject to constraints on their collinearity which are not shared by random combinations. The $d_\perp$ cut also uses kinematic constraints to remove events where the K^0_s is not compatible with coming from the same location as the $\pi\pi$ pair. The p_T and η cuts for the D^0 together with the Q^2 and y cuts for the event define the kinematic region within which the cross sections will be measured. It was originally hoped to be able to go down to $p_T = 0$, however there proved to be too much background to obtain a signal at very low p_T. A lower limit of 1.0 GeV is still an improvement on previous D^0 measurements, which typically require a minimum p_T of 1.5 GeV.

The mass distribution of the reconstructed D^0 candidates is shown in Figure 8.3. The data are fitted with the function

$$f(x) = p_1 \exp\left(-\frac{1}{2}\left(\frac{x - p_2}{p_3}\right)^2\right) + p_4 + p_5 x + p_6 x^2, \tag{8.6}$$

with $p_1 - p_6$ being free parameters. The D^0 mass peak is located at (1.860 ± 0.002) GeV, with a width of (0.023 ± 0.003) GeV and contains 5812 ± 573 events.

8.6 Cross Section Unfolding

The differential cross section in an observable Y is given by

$$\frac{\mathrm{d}\sigma}{\mathrm{d}Y} = \frac{N}{A \cdot \mathcal{L} \cdot B \cdot \Delta Y}, \tag{8.7}$$

where N is the number of decays of interest (here $D^0 \to K^0_s\pi\pi$) in a bin of width ΔY, B is the branching ratio for the decay, $\mathcal{L}$ is the integrated luminosity and A is the acceptance (see below). The integrated cross section over the whole kinematic region may similarly be found from

$$\sigma = \frac{N}{A \cdot \mathcal{L} \cdot B}. \tag{8.8}$$

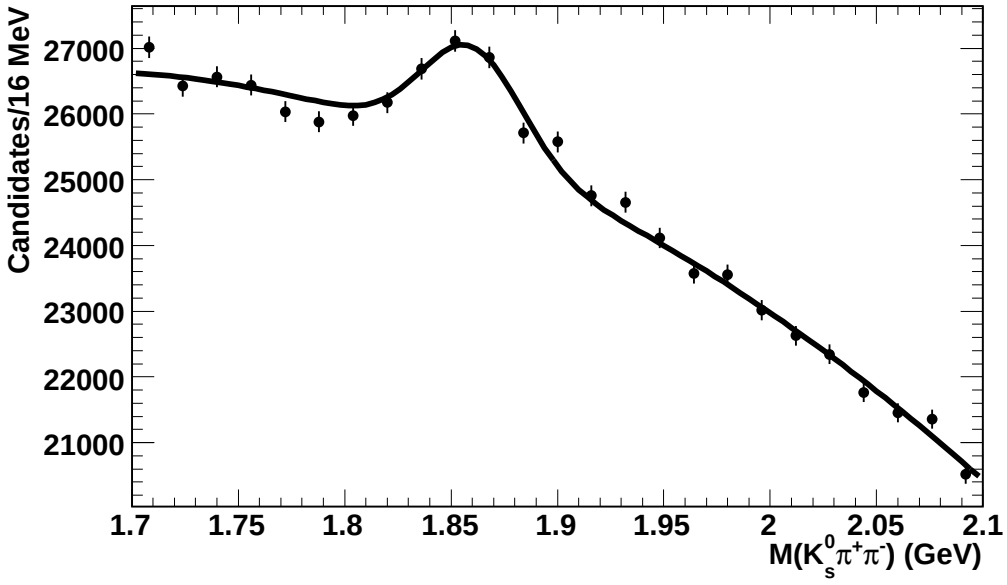


Figure 8.3: Plot of invariant mass for $D^0 \to K^0_s\pi\pi$ candidates. The line is a gaussian plus second-order-polynomial fit.

The acceptance is determined from Monte Carlo using the formula

$$A = \frac{Efficiency}{Purity} = \frac{N_{rec}}{N_{gen}}, \tag{8.9}$$

with

$$\text{Efficiency} = \frac{N_{rec} \cap N_{gen}}{N_{gen}}, \ \text{Purity} = \frac{N_{rec} \cap N_{gen}}{N_{rec}}. \tag{8.10}$$

N_{rec} is the number of events reconstructed in the desired channel in a given bin, N_{gen} is the number of Monte Carlo events which were generated in this bin. The acceptance takes into account migrations between bins, the efficiency of the selection and reconstruction, and also QED radiative effects, since these are included in the Monte Carlo used to calculate the acceptance.

The efficiency for the D^0 over the kinematic region is 8.9%, the purity is 98%, giving an acceptance of 9%.

The efficiencies, purities and acceptances for the bins in which the differential cross

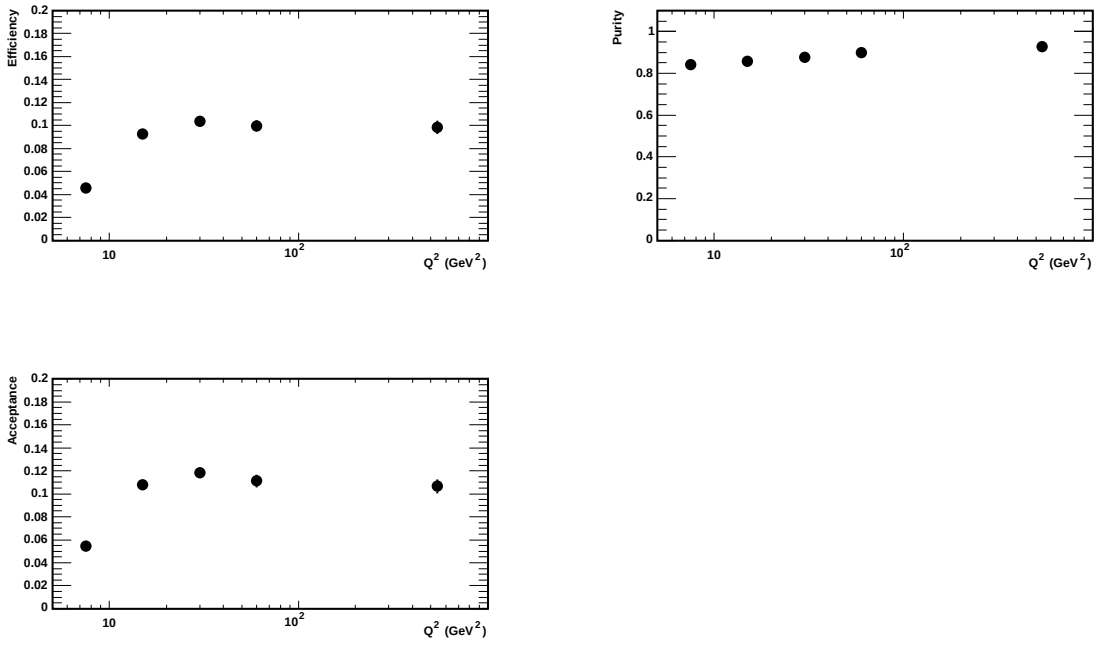


Figure 8.4: Plots showing the efficiency, purity and acceptance for reconstructing $D^0 \to K^0_s\pi\pi$ in bins of Q^2

sections are measured are shown in Figures 8.4 – 8.7. These are similar to the total values, although the purities for the middle two x bins are only around 40%. This indicates that either the bins are too narrow and are suffering from migrations, or that x is not being well reconstructed.

8.7 Integrated Cross Section

The integrated cross section for the decay $D^0 \to K^0_s\pi^+\pi^- \to \pi^+\pi^-\pi^+\pi^-$ was measured in the kinematic region $5 < Q^2 < 1000\,\mathrm{GeV}^2$, $0.02 < y < 0.7$, $1.0 < p_T(D^0) < 20.0\,\mathrm{GeV}$, $|\eta(D^0)| < 1.6$ to be

$$\sigma(D^0) = 14.34 \pm 1.41\,(\mathrm{stat.})^{+1.52}_{-2.65}\,(\mathrm{syst.}) \pm 0.94(\mathrm{BR})\ \mathrm{nb}$$

The central value together with the statistical error was determined from a fit to the mass spectrum shown in Figure 8.3, where the fitting function had the form given in

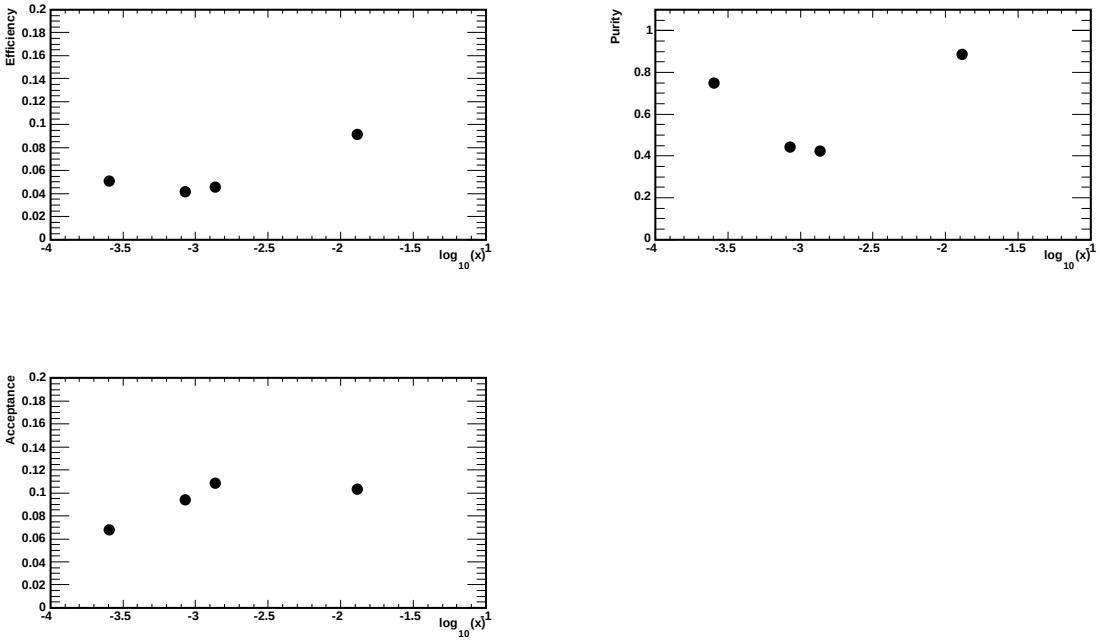


Figure 8.5: Plots showing the efficiency, purity and acceptance for reconstructing $D^0 \rightarrow K^0_s\pi\pi$ in bins of x

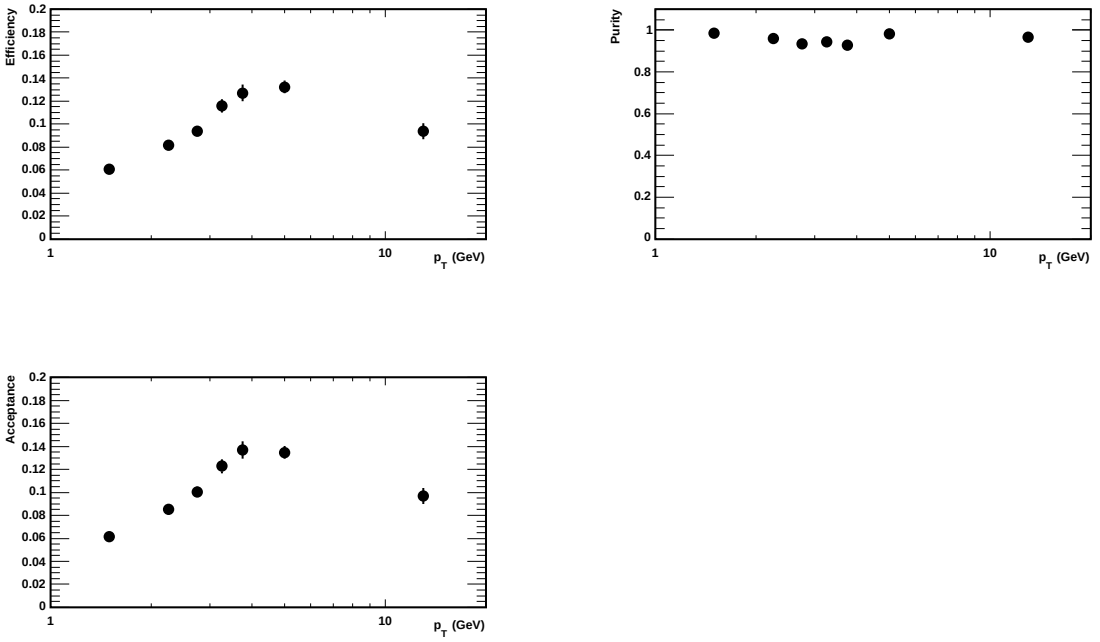


Figure 8.6: Plots showing the efficiency, purity and acceptance for reconstructing $D^0 \rightarrow K^0_s\pi\pi$ in bins of p_T

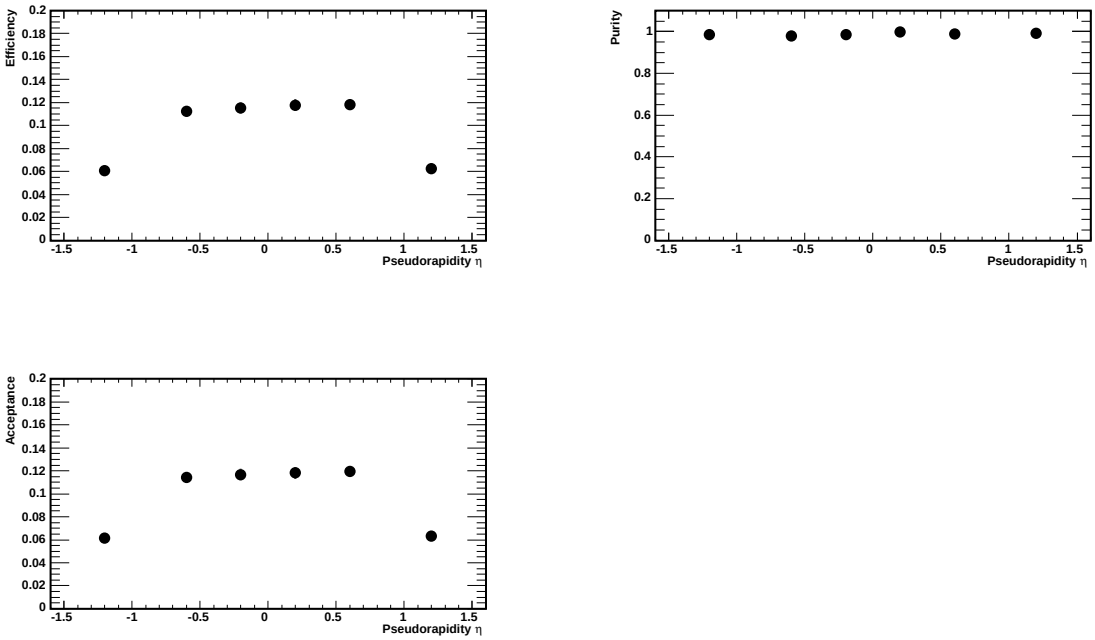


Figure 8.7: Plots showing the efficiency, purity and acceptance for reconstructing $D^0 \rightarrow K^0_s\pi\pi$ in bins of η

Equation 8.6. The systematic errors are discussed in the following section. The uncertainty labelled BR is the error on the cross section due to the uncertainty in the measured branching ratio taken from [1]. The branching ratio used was

$$\begin{aligned} B(D^0 \rightarrow K^0_s\pi^+\pi^- \rightarrow \pi^+\pi^-\pi^+\pi^-) &= B(D^0 \rightarrow K^0_s\pi^+\pi^-) \times B(K^0_s \rightarrow \pi^+\pi^-) \\ &= (2.01 \pm 0.13)\% \end{aligned}$$

The NLO prediction from HVQDIS for the cross section in the same kinematic region is

$$\sigma^{NLO}(D^0) = 14.60\,^{+1.55}_{-1.56}\,(\text{syst.})\ \text{nb}$$

This is in good agreement with the data.

For calculation of quantities such as the strangeness-suppression factor (Section 9.7) or baryon to meson ratio (Section 10.5) it is necessary to restrict the kinematic region to that used to measure the other charmed hadrons. This involves raising the lower bound

on $p_T(D^0)$ from 1.0 GeV to 1.5 GeV. In this new kinematic region the integrated cross section is measured to be

$$\sigma(D^0) = 11.38 \pm 0.95\,(\text{stat.})^{+1.05}_{-1.62}\,(\text{syst.}) \pm 0.75(\text{BR})\ \text{nb}$$

The NLO prediction from HVQDIS for the cross section in the same kinematic region is

$$\sigma^{NLO}(D^0) = 11.20\,^{+1.22}_{-1.15}\,(\text{syst.})\ \text{nb}.$$

8.8 Systematic Errors

The measured cross section is dependent on the selection cuts and procedure used to obtain the signal. The theoretical prediction is similarly dependent on its inputs. In order to evaluate the sensitivity of the cross section to these effects, each of the cuts or inputs is varied by an appropriate amount, the extraction of the cross section repeated, and the fractional difference from the nominal cross section obtained. The upper systematic error is obtained by adding in quadrature all the positive fractional differences, the lower systematic error is obtained similarly from the negative fractional differences. Systematic errors were evaluated both for the integrated cross section and for each bin of the differential cross sections.

8.8.1 Experimental Systematics

The variations of the selection cuts used to estimate the systematic errors for the data are shown in Table 8.1. Most of these cuts have been described in sections 8.3 and 8.4, however some require further explanation.

Systematics 7 – 10 vary the calorimeter energy up and down in the Monte Carlo only, to account for the uncertainty in the calibration of the calorimeter energy scale. The last two entries in the table are not in fact selection cuts. Systematic 42 uses RAPGAP instead of DJANGOH to calculate the acceptance. Systematic 43 adds the uncertainty on the experimental measurement of the ZEUS luminosity in quadrature with the other

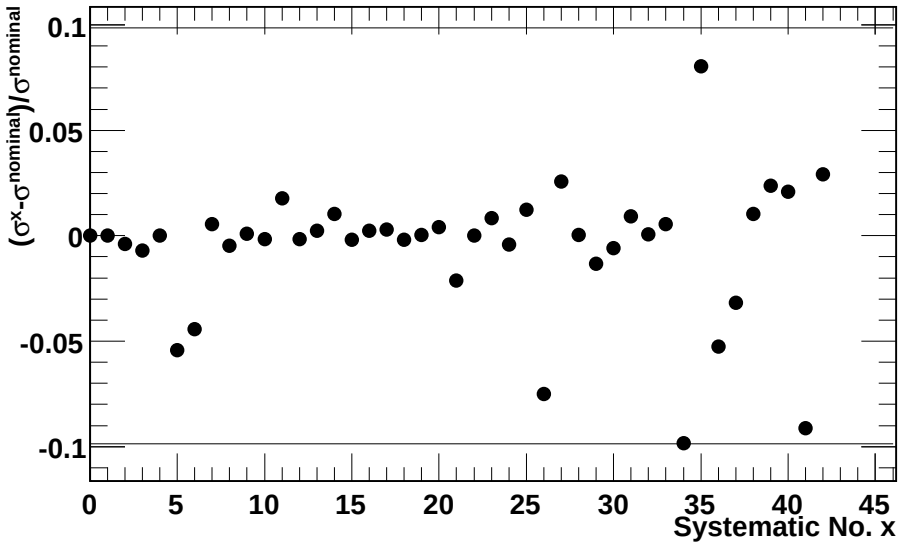


Figure 8.8: Percentage differences in the D^0 cross section caused by each systematic check. See Table 8.1 for the key. The horizontal lines correspond to the statistical error on the nominal cross section.

systematic errors. The percentage changes in the cross sections caused by each of these systematics can be seen in Figure 8.8.

The systematics which give large effects are raising the p_T requirement on the pion tracks (systematic 26), requiring the tracks to have hits in the MVD (systematic 34), tightening the cut on the invariant mass of the $\pi^+\pi^-$ pair which does not comprise the K^0_s (systematic 35), and decreasing the allowed distance between the K^0_s trajectory and the $\pi^+\pi^-$ vertex (systematic 41).

8.8.2 Theoretical Systematics

The variations of the HVQDIS inputs used to estimate the systematic errors for the NLO prediction are shown in Table 8.2.

The value of $\epsilon = 0.072 \pm 0.014$ for the Peterson parameter is taken from a recent measurement made at ZEUS [34]. Previous analyses have used a value of $\epsilon = 0.035 \pm 0.014$ obtained from fits to ARGUS data [35]. The charm mass is changed consistently in

#	**Nominal value**	**Variation**
1	$y_{electron} < 0.95$	$y_{el} < 0.90$
2	$y_{JB} > 0.02$	$y_{JB} > 0.03$
3	$40 < E - p_z < 70\,\text{GeV}$	$42 < E - pz < 65\,\text{GeV}$
4	$\|Z_{vtx}\| < 50\,\text{cm}$	$\|Z_{vtx}\| < 45\,\text{cm}$
5	$E_e > 10\,\text{GeV}$	$E_e > 11\,\text{GeV}$
6	15 cmBox cut	16 cmBox cut
7	Electron energy scale (MC only)	$E_e \times 0.98$
8	Electron energy scale (MC only)	$E_e \times 1.02$
9	Hadronic energy scale (MC only)	Energy$\times$0.97
10	Hadronic energy scale (MC only)	Energy$\times$1.03
11	$0.47 < M(K_s^0) < 0.52\,\text{GeV}$	$0.46 < M(K_s^0) < 0.53\,\text{GeV}$
12	$0.47 < M(K_s^0) < 0.52\,\text{GeV}$	$0.48 < M(K_s^0) < 0.51\,\text{GeV}$
13	Impact parameter $> 0.05\,\text{cm}$	Imp par $> 0.04\,\text{cm}$
14	Impact parameter $> 0.05\,\text{cm}$	Imp par $> 0.06\,\text{cm}$
15	K_s^0 vertex: $x^2 + y^2 < 400\,\text{cm}^2$	$x^2 + y^2 < 361\,\text{cm}^2$
16	K_s^0 vertex: $x^2 + y^2 < 400\,\text{cm}^2$	$x^2 + y^2 < 441\,\text{cm}^2$
17	K_s^0 3D collinearity $coll_{3D} < 0.3\,\text{rad}$	$coll_{3D} < 0.35\,\text{rad}$
18	K_s^0 3D collinearity $coll_{3D} < 0.3\,\text{rad}$	$coll_{3D} < 0.25\,\text{rad}$
19	K_s^0 2D collinearity: $\cos(coll_{2D}) > 0.99$	$\cos(coll_{2D}) > 0.985$
20	K_s^0 2D collinearity: $\cos(coll_{2D}) > 0.99$	$\cos(coll_{2D}) > 0.995$
21	K_s^0 tracks:$DCA < 0.4\,\text{cm}$	DCA$< 0.3\,\text{cm}$
22	K_s^0 tracks:$DCA < 0.4\,\text{cm}$	DCA$< 0.5\,\text{cm}$
23	K_s^0 vertex: $\chi^2 < 5$	$\chi^2 < 4$
24	K_s^0 2D distance to beamspot: $d > 0.2\,\text{cm}$	$d > 0.15\,\text{cm}$
25	K_s^0 2D distance to beamspot: $d > 0.2\,\text{cm}$	$d > 0.25\,\text{cm}$
26	p_T of π, p from $K_s^0 > 0.15\,\text{GeV}$	$pT > 0.175\,\text{GeV}$
27	$\|\eta\|$ of π, p from $K_s^0 < 1.75$	$\|\eta\| < 1.6$
28	K_s^0: $\|\eta\| < 1.6$	$\|\eta\| < 1.5$
29	K_s^0: $\|\eta\| < 1.6$	$\|\eta\| < 1.75$
30	Λ exclusion for K_s^0: $M(p\pi) > 1.121\,\text{GeV}$	$M(p\pi) > 1.12\,\text{GeV}$
31	Λ exclusion for K_s^0: $M(p\pi) > 1.121\,\text{GeV}$	$M(p\pi) > 1.122\,\text{GeV}$
32	Conversions: $M(e^+e^-) > 0.05\,\text{GeV}$	$M(e^+e^-) > 0.04\,\text{GeV}$
33	Conversions: $M(e^+e^-) > 0.05\,\text{GeV}$	$M(e^+e^-) > 0.06\,\text{GeV}$
34	Number MVD hits > 0	$n_{MVD} \geq 4$
35	For the pions not from K_s^0 $0.279 < M(\pi\pi) < 1.4\,\text{GeV}$	$0.289 < M(\pi\pi) < 1.39\,\text{GeV}$
36	Angle of K_s^0 in D^0 rest frame wrt D^0 in lab frame: $\cos(\theta^*) < 0.8$	$\cos(\theta^*) < 0.85$
37	Angle of K_s^0 in D^0 rest frame wrt D^0 in lab frame: $\cos(\theta^*) < 0.8$	$\cos(\theta^*) < 0.75$
38	K_s^0 collinearity wrt $\pi^+\pi^-$ vertex $\cos(\theta_{coll}) > 0.99$	$\cos(\theta_{coll}) > 0.985$
39	K_s^0 collinearity wrt $\pi^+\pi^-$ vertex $\cos(\theta_{coll}) > 0.99$	$\cos(\theta_{coll}) > 0.995$
40	Dist. of K_s^0 trajectory to $\pi^+\pi^-$ vertex $< 0.4\,\text{cm}$	dca$< 0.5\,\text{cm}$
41	Dist. of K_s^0 trajectory to $\pi^+\pi^-$ vertex $< 0.4\,\text{cm}$	dca$< 0.3\,\text{cm}$
42	MC used for extraction: DJANGOH	RAPGAP
43	Luminosity	3.5% error

Table 8.1: List of variations of selection criteria used to estimate the systematic uncertainty. See Sections 8.3 and 8.4 for explanations of the cuts.

HVQDIS and in the input PDF. The uncertainty on the ZEUS PDF, which comes from the uncertainty on the measured data on which the fit is based, is taken into account by using the versions of the PDF corresponding to the upper and lower limits of the fit. In a QCD calculation to all orders the prediction should not depend on the renormalisation and factorisation scales, however for calculation to finite orders it does. The variation in scales is supposed to cover the uncertainty due to the uncalculated higher-order terms. The scales used here follow previous ZEUS analyses. The hadronisation fraction is varied up and down by the experimental error on the measured value taken from [36].

The percentage changes in the predicted cross section can be seen in Figure 8.9. The largest differences come from changing the charm mass.

#	**Nominal value**	**Variation**
1	Peterson Fragmentation Parameter $\epsilon = 0.072$	$\epsilon = 0.058$
2	Peterson Fragmentation Parameter $\epsilon = 0.072$	$\epsilon = 0.086$
3	Charm quark mass $m_c = 1.35$ GeV	$m_c = 1.2\,\text{GeV}$
4	Charm quark mass $m_c = 1.35$ GeV	$m_c = 1.5\,\text{GeV}$
5	Proton PDF (ZEUS NLO Fit)	lower experimental limit on fit
6	Proton PDF (ZEUS NLO Fit)	upper experimental limit on fit
7	Renormalisation and factorisation scales $\mu_F = \mu_R = \mu = \sqrt{Q^2 + 4m_c^2}$	$\mu = \max(2m_c,\, 0.5\sqrt{Q^2 + 4m_c^2})$
8	Renormalisation and factorisation scales $\mu_F = \mu_R = \mu = \sqrt{Q^2 + 4m_c^2}$	$\mu = 2\sqrt{Q^2 + 4m_c^2}$
9	Hadronisation fraction $f(c \to D^0) = 0.557$	$f(c \to D^0) = 0.534$
10	Hadronisation fraction $f(c \to D^0) = 0.557$	$f(c \to D^0) = 0.58$

Table 8.2: List of variations of input parameters to the HVQDIS program used to calculate the NLO cross section. See text for details.

8.9 Differential Cross Sections

Differential cross sections have been measured as a function of Q^2, x, $p_T(D^0)$ and $\eta(D^0)$ in the same kinematic region as the integrated cross section. These are shown in Figure 8.10, where they are compared to the NLO predictions from HVQDIS. The contribution to the cross section of charm coming from beauty decays, as given by the RAPGAP Monte

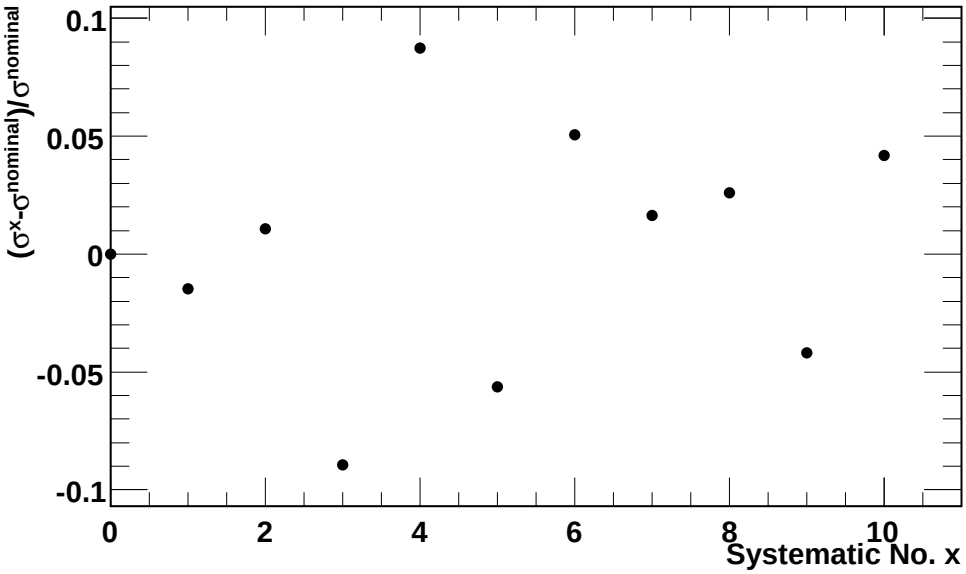


Figure 8.9: Percentage differences in the NLO prediction for the D^0 cross section caused by changing the input parameters. See Table 8.2 for the key.

Carlo, is also shown.[2] The measured values, along with the HVQDIS predictions, and their uncertainties are tabulated in Table 8.3, which also indicates the binning used. Uncertainties on the luminosity and branching ratio (for data) and the hadronisation fraction (for NLO) are not included, as any change in these values would just result in a global scaling of all bins by the same factor. These uncertainties are however included in the integrated cross section. Plots showing the percentage changes in the cross section as a result of the systematic checks can be found in Appendix A.1.

The differential cross section in η is more or less flat over the kinematic region of interest, those in x and p_T span two orders of magnitude, while $\mathrm{d}\sigma/\mathrm{d}Q^2$ spans three orders of magnitude. Despite this the NLO predictions provide a good description of the data for all variables, agreeing to within 2σ in all bins, and within 1σ in most bins.

[2]RAPGAP was used instead of the DJANGOH as there existed a higher-statistics sample, and the contribution from this source is small.

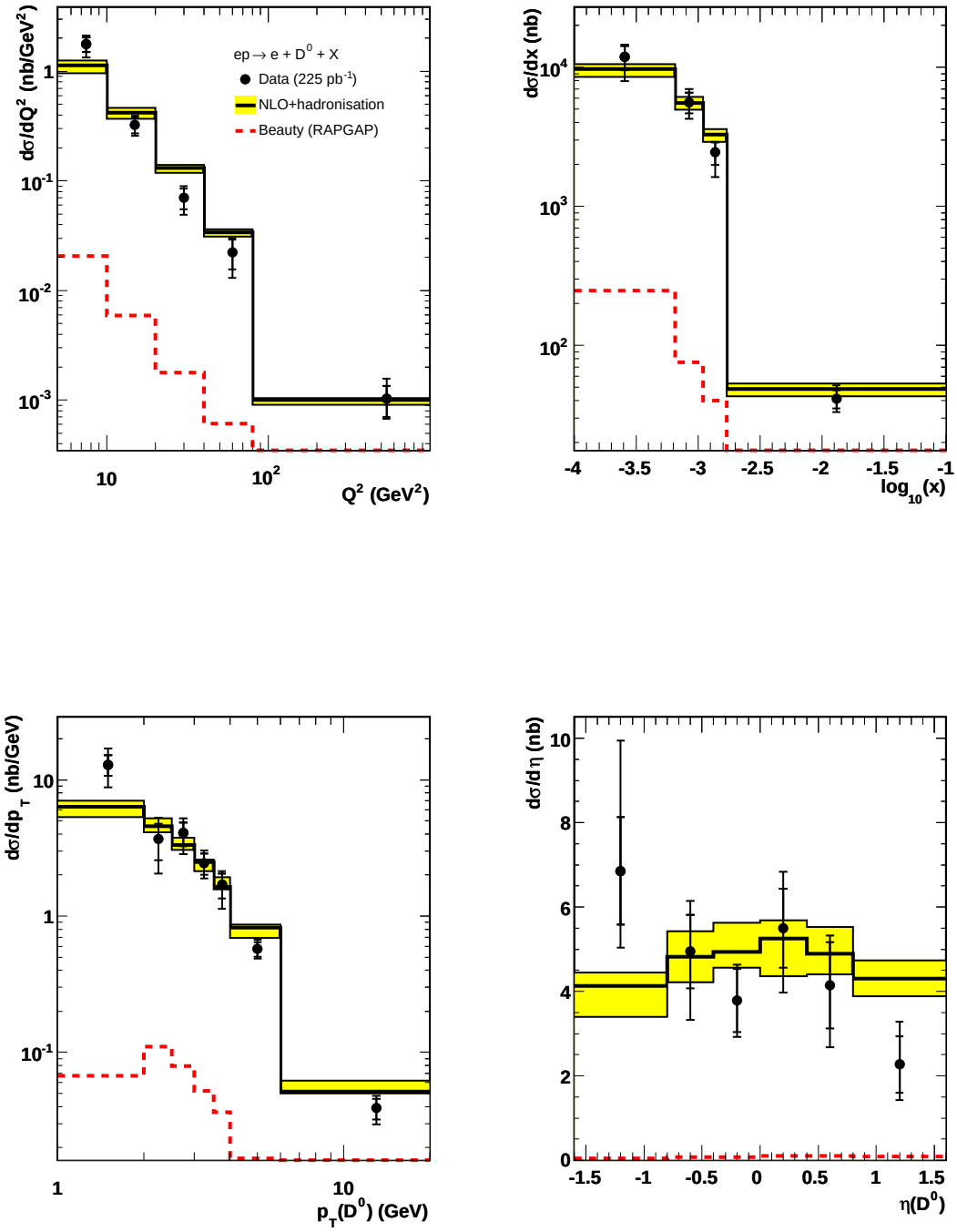


Figure 8.10: D^0 differential cross sections: $\mathrm{d}\sigma/\mathrm{d}Q^2$, $\mathrm{d}\sigma/\mathrm{d}x$, $\mathrm{d}\sigma/\mathrm{d}p_T(D^0)$, and $\mathrm{d}\sigma/\mathrm{d}\eta(D^0)$. The inner error bars are statistical only, the outer bars are the statistical and systematic errors added in quadrature. The solid band corresponds to the systematic uncertainties on the HVQDIS NLO prediction as described in Section 8.8.2. The dashed line indicates the contribution from beauty decays as predicted by RAPGAP Monte Carlo. Uncertainties on the luminosity measurement and branching ratio are not included.

Q^2 bin (GeV^2)	$\mathrm{d}\sigma/\mathrm{d}Q^2$	Δ_{stat} ($\mathrm{nb}/\mathrm{GeV}^2$)	Δ_{syst}	$\mathrm{d}\sigma^{NLO}/\mathrm{d}Q^2$ ($\mathrm{nb}/\mathrm{GeV}^2$)	$\Delta^{NLO}_{\mathrm{syst}}$
5, 10	1.76	± 0.27	$^{+0.23}_{-0.33}$	1.13	$^{+0.12}_{-0.16}$
10, 20	0.324	± 0.053	$^{+0.041}_{-0.043}$	0.416	$^{+0.046}_{-0.047}$
20, 40	0.070	± 0.015	$^{+0.013}_{-0.015}$	0.1312	$^{+0.0093}_{-0.013}$
40, 80	0.0222	± 0.0067	$^{+0.0038}_{-0.0063}$	0.0341	$^{+0.0019}_{-0.0030}$
80, 1000	0.00103	± 0.00033	$^{+0.00043}_{-0.00012}$	0.001004	$^{+0.000042}_{-0.000091}$
x bin	$\mathrm{d}\sigma/\mathrm{d}x$	Δ_{stat} (nb)	Δ_{syst}	$\mathrm{d}\sigma^{NLO}/\mathrm{d}x$ (nb)	$\Delta^{NLO}_{\mathrm{syst}}$
0.0001, 0.00065	11931	± 2365	$^{+1037}_{-3174}$	9766	$^{+801}_{-1238}$
0.00065, 0.0011	5607	± 944	$^{+1022}_{-977}$	5536	$^{+563}_{-595}$
0.0011, 0.0017	2441	± 447	$^{+150}_{-683}$	3269	$^{+340}_{-373}$
0.0017, 0.1	41.4	± 6.1	$^{+8.4}_{-5.5}$	48.6	$^{+4.8}_{-5.7}$
$p_T(D^0)$ bin (GeV)	$\mathrm{d}\sigma/\mathrm{d}p_T(D^0)$	Δ_{stat} (nb/GeV)	Δ_{syst}	$\mathrm{d}\sigma^{NLO}/\mathrm{d}p_T(D^0)$ (nb/GeV)	$\Delta^{NLO}_{\mathrm{syst}}$
1.0, 2.0	12.9	± 2.3	$^{+3.3}_{-3.4}$	6.33	$^{+0.69}_{-1.00}$
2.0, 2.5	3.67	± 1.10	$^{+1.13}_{-1.19}$	4.55	$^{+0.66}_{-0.45}$
2.5, 3.0	4.07	± 0.80	$^{+0.81}_{-0.94}$	3.33	$^{+0.42}_{-0.29}$
3.0, 3.5	2.44	± 0.43	$^{+0.40}_{-0.36}$	2.49	$^{+0.093}_{-0.35}$
3.5, 4.0	1.70	± 0.36	$^{+0.25}_{-0.44}$	1.64	$^{+0.29}_{-0.07}$
4.0, 6.0	0.574	± 0.070	$^{+0.063}_{-0.055}$	0.821	$^{+0.045}_{-0.13}$
6.0, 20	0.0389	± 0.0066	$^{+0.0059}_{-0.0064}$	0.051	$^{+0.010}_{-0.0016}$
$\eta(D^0)$ bin	$\mathrm{d}\sigma/\mathrm{d}\eta(D^0)$	Δ_{stat} (nb)	Δ_{syst}	$\mathrm{d}\sigma^{NLO}/\mathrm{d}\eta(D^0)$ (nb)	$\Delta^{NLO}_{\mathrm{syst}}$
-1.6, -0.8	6.86	± 1.28	$^{+2.81}_{-1.29}$	4.12	$^{+0.32}_{-0.72}$
-0.8, -0.4	4.94	± 0.87	$^{+0.82}_{-1.36}$	4.82	$^{+0.60}_{-0.60}$
-0.4, 0.0	3.79	± 0.75	$^{+0.40}_{-0.45}$	4.93	$^{+0.69}_{-0.38}$
0.0, 0.4	5.50	± 0.93	$^{+0.97}_{-1.21}$	5.26	$^{+0.42}_{-0.89}$
0.4, 0.8	4.15	± 1.02	$^{+0.60}_{-1.05}$	4.90	$^{+0.62}_{-0.49}$
0.8, 1.6	2.27	± 0.67	$^{+0.77}_{-0.51}$	4.31	$^{+0.44}_{-0.41}$

Table 8.3: Values of D^0 differential cross sections. The lefthand column gives the binning, the middle three columns are the measured values with their associated uncertainties, the rightmost two columns are the NLO predictions from HVQDIS, with their uncertainties. Uncertainties on the luminosity and branching ratio (for data) and the hadronisation fraction (for NLO) are not included.

Chapter 9

$D^{\pm} \to K^0_S \pi^{\pm}$ and $D^{\pm}_S \to K^0_S K^{\pm}$ Decay Channels

9.1 Introduction

Having studied the decay of the D^0 into a final state with a K^0_s it is natural to consider the charged D meson decaying similarly. The strictly analogous channel to the D^0 case is $D^{\pm} \to K^0_s \pi^{\pm} \pi^0$, however the π^0 does not leave a track so is difficult to reconstruct. Instead the channel

$$D^{\pm} \to K^0_s \pi^{\pm} \tag{9.1}$$

was used. The experimental signature for this is a two-track vertex plus another track. At the time this analysis was started the $\mathrm{d}E/\mathrm{d}x$ calibrations and parametrisations for HERA-II data had not been completed, which meant that this quantity could not be used to perform particle identification. Therefore when constructing D^+ candidates kaons or protons might be selected instead of pions for the "other" track. This would lead to backgrounds in the $D^{\pm}$ channel from the corresponding $D^{\pm}_s$ and $\Lambda^{\pm}_c$ decays:

$$D^{\pm}_s \to K^0_s K^{\pm} \tag{9.2}$$

$$\Lambda^{\pm}_c \to K^0_s p^{\pm}. \tag{9.3}$$

Since these channels also provide a measurement of charm production, and use the same reconstruction algorithm it was decided to study them as well. For convenience the shorthand $D \to K^0_s X$ will be used to refer to these three channels taken together.[1]

The initial idea was to use each X track only once, treating all three channels simultaneously thereby reducing the combinatorial background in all channels. The assignment of a particle species for the X track was to be based on its decay length and the invariant mass. The decay lengths are sufficiently different ($D^\pm$: $c\tau = 312\,\mu\text{m}$, $D^\pm_s$: $c\tau = 150\,\mu\text{m}$, Λ_c: $c\tau = 60\,\mu\text{m}$ [1]) as are the invariant masses ($M(D^\pm) = 1869\,\text{GeV}$, $M(D^\pm_s) = 1968\,\text{GeV}$, $M(\Lambda_c) = 2286\,\text{GeV}$ [1]), however both variables gave problems. Since the K^0_s is neutral the D decay vertex, and hence the decay length, had to be calculated by finding the intersection of the X track with the extrapolated K^0_s trajectory, which was determined from the vector sum of the momentum of its two decay products. Unfortunately Monte Carlo studies showed that this gave results which were only accurate to within a couple of centimetres. Also, trying to weight the invariant mass of the candidates with a set of gaussians centred at the nominal values ended up simply imposing these Gaussian peaks on the final invariant mass spectrum.

A set of kinematic cuts was then used to try to obtain a signal for each channel individually. This also failed to give a signal. A method based on that used by the DELPHI collaboration in [55] was eventually used. This combines the signal and background distributions for several variables to produce a number between zero and one (the *discriminant*) indicating the likelihood for the given candidate to have come from the decay of interest. True decays give a value peaked at one, background events give values covering the whole range, peaked near zero and falling off near one. This method is explained in more detail in Section 9.3.

[1] The decays $D^\pm \to K^0_s K^\pm$ and $D^\pm_s \to K^0_s \pi^\pm$ are also possible, but are Cabibbo-suppressed, hence they are neglected in this thesis.

9.2 Charmed Hadron Reconstruction

DIS events are selected in the manner described in sections 8.2 and 8.3. The K_s^0 in the final state is reconstructed using the same procedure as in Section 8.4. The charmed hadron candidates (the "D") are formed by successively combining the K_s^0 candidate with all other tracks in the event (the "X" track) which satisfy certain criteria:

- $p_T(X) > 0.15\,\mathrm{GeV}$
- $|\eta(X)| < 1.75$
- Inner superlayer of X track ≤ 1
- Outer superlayer of X track ≥ 3
- $0 <$ dca of X track to K_s^0 trajectory $< 2\,\mathrm{cm}$
- $0 <$ dca of X track to beamspot $< 0.4\,\mathrm{cm}$

The distance of closest approach of the X track to the K_s^0 trajectory is calculated assuming the X track is also linear. This is a reasonable approximation for the typical momenta involved, and in Monte Carlo studies gave better separation between signal and background than the previous method of treating the X track as a helix. The linear approximation also allows the distance of closest approach to be calculated analytically.

The restriction on the distance of the track from the beamspot is designed to select only tracks coming from the interaction region. While tracks from charm decays should have a non-zero impact parameter, a cut of 0.4 cm should (and in Monte Carlo does) include all signal events.

The invariant mass of the D is then calculated from the four-momenta of the K_s^0 candidate and X track, assigning the pion, kaon and proton mass to the X track in turn, to produce $D^{\pm}$, $D_s^{\pm}$ and $\Lambda_c^{\pm}$ candidates respectively. A candidate for any of these three channels is kept if it satisfies

- $1.7 < M(D) < 2.5\,\mathrm{GeV}$

- $1.5 < p_T(D) < 20.0\,\mathrm{GeV}$
- $|\eta(D)| < 1.6$

where M is the invariant mass for that channel. Note that one $K^0_s X$ combination may simultaneously be a candidate for more than one of the decay channels. There was initially no lower limit on the p_T in an attempt to go as low in p_T as possible, however after applying the discriminant cut (section 9.3) very few events survived with a p_T less than 1.5 GeV, so a cut was imposed at this value.

9.3 Discriminant Method

The mass spectra of the candidates obtained by the method described in the previous section do not exhibit a clear peak. Additional cuts are required to isolate the signal. As mentioned in Section 9.1 a few methods were tried before adopting one used by DELPHI [55], which is as follows.

Let the quantity R be defined as

$$R = \prod_i \frac{S_i(x_i)}{B_i(x_i)} \tag{9.4}$$

where x_i is the value of the i^{th} variable for the candidate, $S_i(x_i)$ is the value of the signal distribution for the i^{th} variable at the value x_i, $B_i(x_i)$ is the corresponding quantity for the i^{th} background distribution, and the product runs over the variables used. Each of the S_i and B_i is normalised to one. Then the *discriminant* is defined as

$$X = \frac{R}{R+1} \tag{9.5}$$

The optimal variables to use in this method are those for which the distributions for signal and background are clearly separated, or cover the same range but have different shapes. Then for a true decay the value of $S_i(x_i)$ will be large and $B_i(x_i)$ small, and vice versa for a fake decay. Thus if appropriate variables are chosen the discriminant will be

concentrated near one for true decays, and at lower values for fake decays.

The variables used for the discriminant in this analysis were

- $p(K_s^0)/p(D)$
- $p_T(D)$
- $p_T(X)/E_T^{\theta>10^\circ}$
- $p_T(D)/E_T^{\theta>10^\circ}$
- $\cos(\theta^*(X))$

where $E_T^{\theta>10^\circ}$ is the transverse energy of the event, excluding the energy in a cone of 10° around the beamline in the forward direction. Excluding this region removes the proton remnant (if any) thereby giving a better estimate of the energy involved in the interaction. The distributions of these variables obtained from Monte Carlo for signal and background in the $D^\pm$ case are shown in Figure 9.1. One can see that the shapes for signal and background in these variables are sufficiently different to be useful in the discriminant.

In order to trust the discriminant method to identify true decays in the data the Monte Carlo must give a good description of the input variables. The distribution of each of the five variables for background events is compared to data (which is mostly background) in Figure 9.2. The level of agreement is reasonable.

The distributions of the discriminant for the three cases, D^+, D_s and Λ_c are shown in Figure 9.3. As desired the signal distribution shows a peak at 1. The background distributions are more or less flat, with a small rise towards 1 and in some cases a peak at zero. The background for the Λ_c however has a larger peak at 1. This means that cutting on the discriminant will not be as effective at enhancing the signal.

Figure 9.4 shows the mass distributions obtained when requiring the discriminant to be greater than 0.85 for D^+, 0.9 for D_s and 0.9 for Λ_c. These cuts were determined by considering where the signal distribution rises above the background distribution in Figure 9.3. Clear peaks can be seen for the D^+ and D_s. The D^+ mass peak is located at

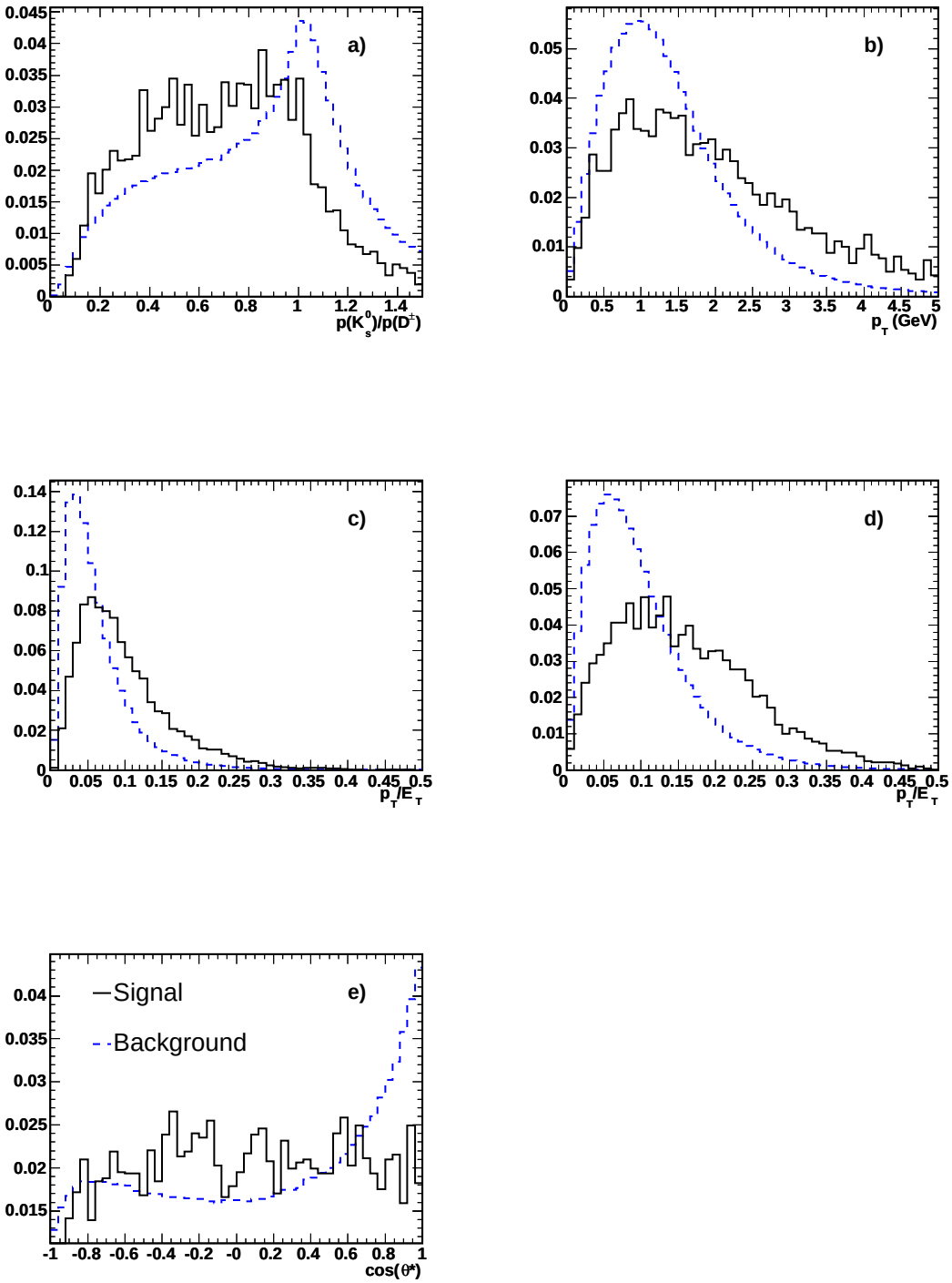


Figure 9.1: Plots comparing the signal (solid line) and background (dashed line) distributions, obtained from Monte Carlo, which are used in the discriminant method. These plots are only for the $D^{\pm}$ case and show a)$p(K^0_s)/p(D^{\pm})$, b)$p_T(D^{\pm})$, c)$p_T(\pi)/E_T^{\theta>10^\circ}$, d)$p_T(D)/E_T^{\theta>10^\circ}$, e)$\cos(\theta^*(X))$. The signal and background are normalised to the same area.

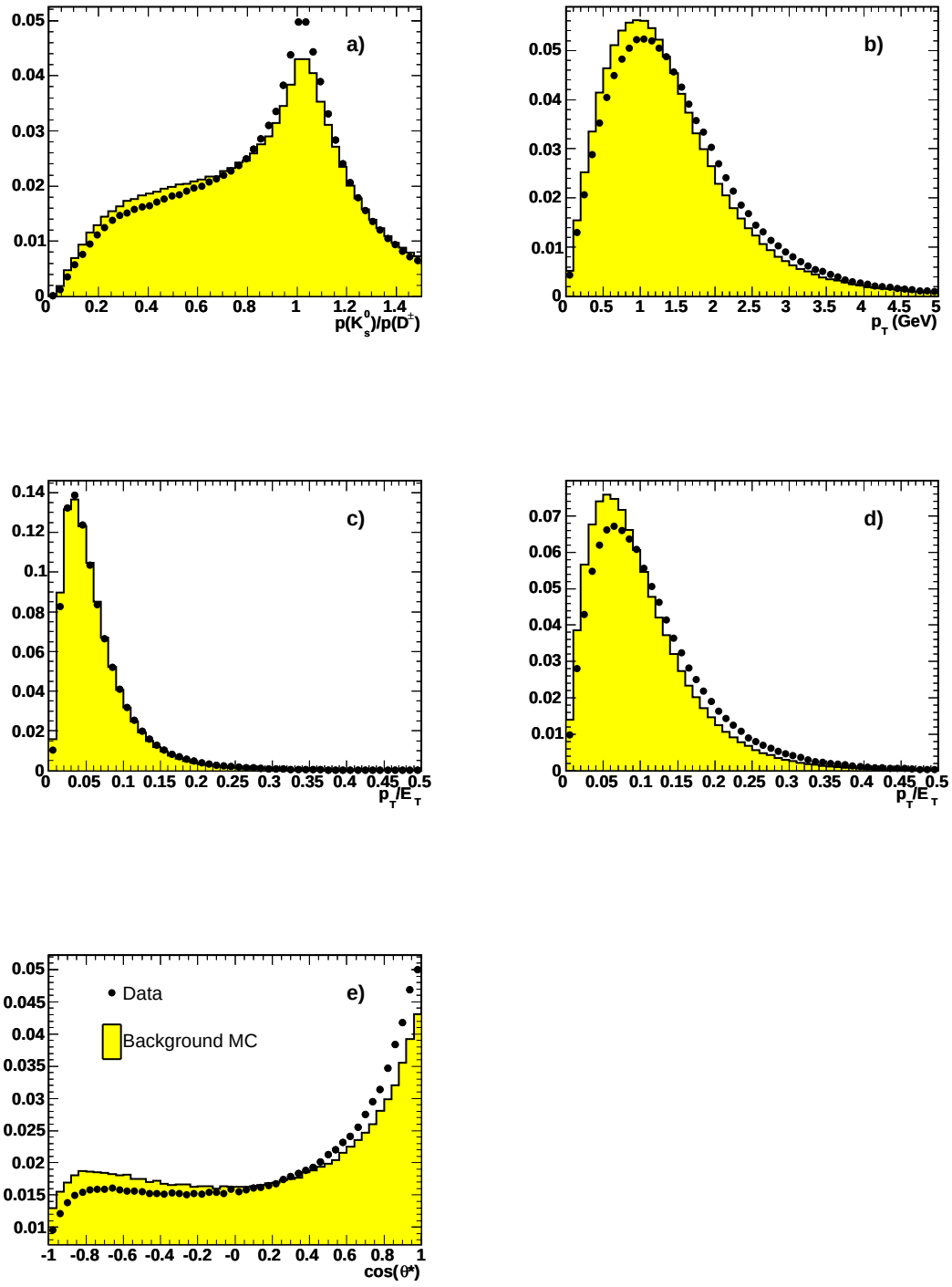


Figure 9.2: Plots comparing the background distributions for data (circles) and DIS MC (solid histograms). These plots are only for the $D^\pm$ case and show a)$p(K^0_s)/p(D^\pm)$, b)$p_T(D^\pm)$, c)$p_T(\pi)/E_T^{\theta>10^\circ}$, d)$p_T(D^\pm)/E_T^{\theta>10^\circ}$, e)$\cos(\theta^*(X))$. The data and background are normalised to the same area.

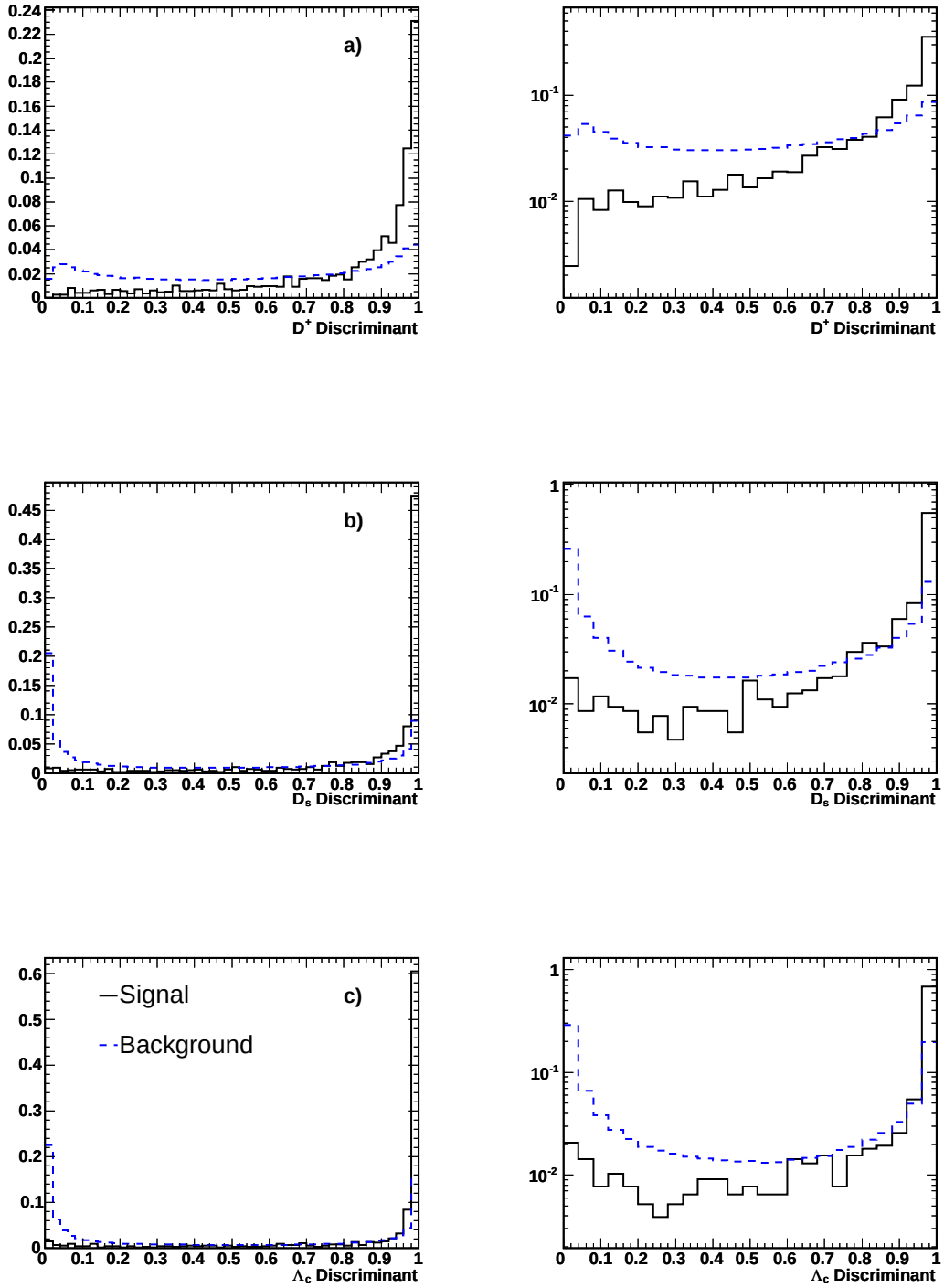


Figure 9.3: Plots comparing the discriminant distributions for true decays (solid lines) of a)D^+, b)D_s, c)Λ_c and background candidates (dashed lines) in MC. The left hand column contains plots with a linear scale, the right hand column contains the corresponding plots with a logarithmic scale. The signal and background distributions are normalised to the same area.

(1.862 ± 0.003) GeV, with a width of (0.022 ± 0.003) GeV and contains 1138 ± 157 events. The D_s mass peak is located at (1.962 ± 0.003) GeV, with a width of (0.018 ± 0.003) GeV and contains 890 ± 141 events. Despite many attempts it did not prove possible to observe a signal in the Λ_c channel. The remainder of this chapter will therefore focus only on the D^+ and D_s channels.

9.4 Integrated Cross Sections

The integrated cross sections for D^+ and D_s in the kinematic region $5 < Q^2 < 1000\,\mathrm{GeV}^2$, $0.02 < y < 0.7$, $1.5 < p_T(D) < 20.0\,\mathrm{GeV}$, $|\eta(D)| < 1.6$ were determined using the same unfolding procedure as described in section 8.6 for the D^0. The central value together with the statistical error for each cross section was determined from a fit to the mass spectrum shown in Figure 9.4, where the fitting function had the form

$$f(x) = p_1 \exp\left(-\frac{1}{2}\left(\frac{x - p_2}{p_3}\right)^2\right) + p_4 + p_5 x, \tag{9.6}$$

with $p_1 - p_5$ being free parameters. The branching ratios used were

$$\begin{aligned} B(D^+ \to K^0_s\pi^+ \to \pi^+\pi^-\pi^+) &= B(D^+ \to K^0_s\pi^+) \times B(K^0_s \to \pi^+\pi^-) \\ &= (1.02 \pm 0.04)\% \\ B(D^+_s \to K^0_s K^+ \to \pi^+\pi^- K^+) &= B(D^+_s \to K^0_s K^+) \times B(K^0_s \to \pi^+\pi^-) \\ &= (1.52 \pm 0.31)\%. \end{aligned}$$

The cross section obtained for the D^+ was

$$\sigma(D^+) = 3.90 \pm 0.54\,(\mathrm{stat.})^{+0.97}_{-0.61}\,(\mathrm{syst.}) \pm 0.16(\mathrm{BR})\ \mathrm{nb}$$

The overall efficiency was 12.7%, the purity 98.4% and the acceptance 12.9%. The NLO

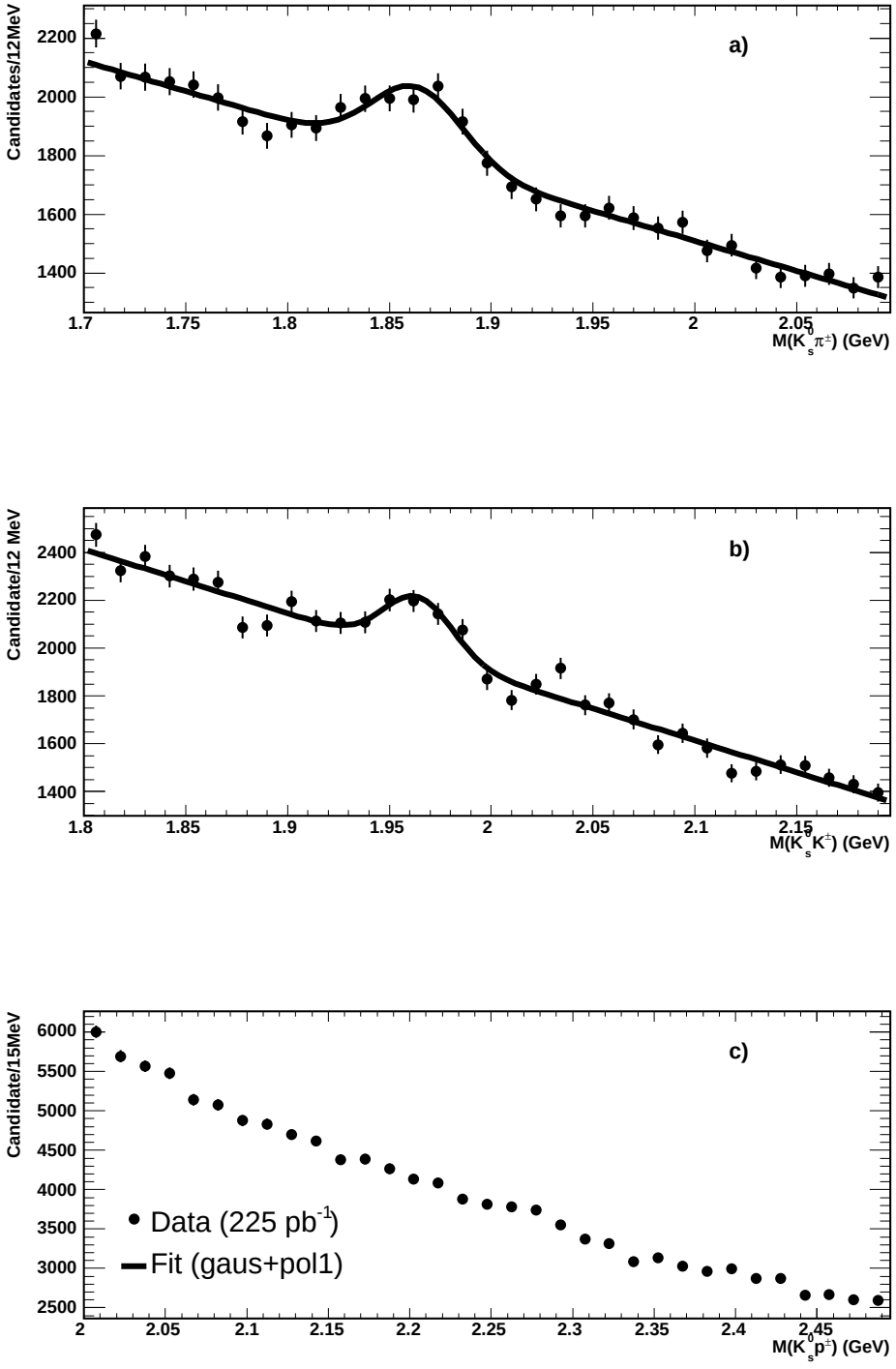


Figure 9.4: $K^0_s X$ mass spectra for a)D^+, b)D_s, c)Λ_c with discriminant cuts of 0.85, 0.9 and 0.9 respectively. The solid line corresponds to a gaussian plus first-order-polynomial fit.

prediction from HVQDIS for the cross section in the same kinematic region is

$$\sigma^{NLO}(D^+) = 4.56\,^{+0.47}_{-0.45}\,(\text{syst.})\ \text{nb}$$

This is slightly higher than the central value from the data, however the two agree within errors.

The cross section obtained for the D_s was

$$\sigma(D_s) = 1.86 \pm 0.30\,(\text{stat.})^{+0.43}_{-0.42}\,(\text{syst.}) \pm 0.38(\text{BR})\ \text{nb}$$

The overall efficiency was 13.8%, the purity 98.7% and the acceptance 14.0%. The NLO prediction from HVQDIS for the cross section in the same kinematic region is

$$\sigma^{NLO}(D_s) = 2.03\,^{+0.21}_{-0.20}\,(\text{syst.})\ \text{nb.}$$

Again the data and NLO prediction agree within errors.

9.5 Systematic Errors

The same procedure as described in Section 8.8 for the D^0 was used to estimate the systematic uncertainty on the measured and NLO cross sections.

The systematic checks performed for the data are detailed in Table 9.1. Systematics 1 to 33 are the same as for the D^0, with the exception of numbers 19 and 20, where a harder collinearity cut is used for the D^+/D_s, since the additional cut on collinearity with respect to a $\pi^+\pi^-$ vertex cannot be applied. Systematics 34 to 40 vary the kinematic cuts on the X track. The value of the discriminant cut is varied up and down by 0.05. As for the D^0 the cross section extraction is repeated using RAPGAP instead of DJANGOH (systematic 43), and the uncertainty on the luminosity measurement is added in quadrature to the other uncertainties (systematic 45). The remaining systematic relates to the possibility of misreconstruction of a true D^+ as a D_s (so-called *reflections*)

and vice versa. Since such events are concentrated in the peak region they may lead to the cross section being overestimated. Monte Carlo studies indicated that the number of D^+'s or D_s's obtained from the fit to the mass spectrum was higher than the true number by approximately the error on the number of reconstructed events. However when such reflections were explicitly subtracted and the fit to the mass distribution repeated, the number of reconstructed events was found to be lower, again by approximately the error on the number of events returned by the fit. Therefore rather than explicitly subtracting the reflections a contribution equal to the statistical error on the cross section was added in quadrature to the downward systematic uncertainty.

The same set of variations for HVQDIS as for the D^0 were used, with the exception that hadronisation fraction was 0.226 ± 0.010 for the D^+ and 0.101 ± 0.009 for the D_s. The results of these systematic checks can be seen in Figures 9.7 and 9.8. As for the D^0 the largest effects come from varying the charm mass. For the D_s the uncertainty on the hadronisation fraction also gives an effect of comparable size.

The results of these systematic checks can be seen in Figures 9.5 and 9.6. The largest effects come from varying the discriminant cut, using RAPGAP instead of DJANGOH, and the uncertainty assigned to cover the effect of reflections.

9.6 Differential Cross Sections

Differential cross sections have been measured for the D^+ and D_s as a function of Q^2, x, $p_T(D)$ and $\eta(D)$ in the same kinematic region as the integrated cross section. These are shown in Figures 9.10 and 9.11, where they are compared to the NLO predictions from HVQDIS. The contribution to the cross section of charm coming from beauty decays, as given by the RAPGAP Monte Carlo, is also shown. The measured values, along with the HVQDIS predictions, and their uncertainties are tabulated in Tables 9.2 and 9.3, which also indicate the binning used. Uncertainties on the luminosity and branching ratio (for data) and the hadronisation fraction (for NLO) are not included, as any change in these values would just result in a global scaling of all bins by the same factor. These

#	Nominal value	Variation
1	$y_{electron} < 0.95$	$y_{el} < 0.90$
2	$y_{JB} > 0.02$	$y_{JB} > 0.03$
3	$40 < E - p_z < 70\,\text{GeV}$	$42 < E - pz < 65\,\text{GeV}$
4	$\lvert Z_{vtx}\rvert < 50\,\text{cm}$	$\lvert Z_{vtx}\rvert < 45\,\text{cm}$
5	$E_e > 10\,\text{GeV}$	$E_e > 11\,\text{GeV}$
6	Boxcut 15 cm	Boxcut 16 cm
7	Electron energy scale (MC only)	$E_e \times 0.98$
8	Electron energy scale (MC only)	$E_e \times 1.02$
9	Hadronic energy scale (MC only)	Energy×0.97
10	Hadronic energy scale (MC only)	Energy×1.03
11	$0.47 < M(K_s^0) < 0.52\,\text{GeV}$	$0.46 < M(K_s^0) < 0.53\,\text{GeV}$
12	$0.47 < M(K_s^0) < 0.52\,\text{GeV}$	$0.48 < M(K_s^0) < 0.51\,\text{GeV}$
13	Impact parameter $> 0.05\,\text{cm}$	Imp par $> 0.04\,\text{cm}$
14	Impact parameter $> 0.05\,\text{cm}$	Imp par > 0.06 cm
15	K_s^0 vertex: $x^2 + y^2 < 400\,\text{cm}^2$	$x^2 + y^2 < 361\,\text{cm}^2$
16	K_s^0 vertex: $x^2 + y^2 < 400\,\text{cm}^2$	$x^2 + y^2 < 441\,\text{cm}^2$
17	K_s^0 3D collinearity $coll_{3D} < 0.3\,\text{rad}$	$coll_{3D} < 0.35\,\text{rad}$
18	K_s^0 3D collinearity $coll_{3D} < 0.3\,\text{rad}$	$coll_{3D} < 0.25\,\text{rad}$
19	K_s^0 2D collinearity: $\cos(coll_{2D}) > 0.995$	$\cos(coll_{2D}) > 0.99$
20	K_s^0 2D collinearity: $\cos(coll_{2D}) > 0.995$	$\cos(coll_{2D}) > 0.999$
21	K_s^0 tracks:$DCA < 0.4\,\text{cm}$	DCA$< 0.3\,\text{cm}$
22	K_s^0 tracks:$DCA < 0.4\,\text{cm}$	DCA$< 0.5\,\text{cm}$
23	K_s^0 vertex: $\chi^2 < 5$	$\chi^2 < 4$
24	K_s^0 2D distance to beamspot: $d > 0.2\,\text{cm}$	$d > 0.15\,\text{cm}$
25	K_s^0 2D distance to beamspot: $d > 0.2\,\text{cm}$	$d > 0.25\,\text{cm}$
26	p_T of π, p from $K_s^0 > 0.15\,\text{GeV}$	$p_T > 0.175\,\text{GeV}$
27	$\lvert\eta\rvert$ of π, p from $K_s^0 < 1.75$	$\lvert\eta\rvert < 1.6$
28	$\lvert\eta(K_s^0)\rvert < 1.6$	$\lvert\eta\rvert < 1.5$
29	$\lvert\eta(K_s^0)\rvert < 1.6$	$\lvert\eta\rvert < 1.75$
30	Λ exclusion for K_s^0: $M(p\pi) > 1.121\,\text{GeV}$	$M(p\pi) > 1.12\,\text{GeV}$
31	Λ exclusion for K_s^0: $M(p\pi) > 1.121\,\text{GeV}$	$M(p\pi) > 1.122\,\text{GeV}$
32	Conversions: $M(e^+e^-) > 0.05\,\text{GeV}$	$M(e^+e^-) > 0.04\,\text{GeV}$
33	Conversions: $M(e^+e^-) > 0.05\,\text{GeV}$	$M(e^+e^-) > 0.06\,\text{GeV}$
34	Distance from K_s^0 trajectory to X track: $0 < \text{dca} < 2\,\text{cm}$	$0 < \text{dca} < 2.5\,\text{cm}$
35	Distance from K_s^0 trajectory to X track: $0 < \text{dca} < 2\,\text{cm}$	$0 < \text{dca} < 1.5\,\text{cm}$
36	Impact parameter of X track $< 0.4\,\text{cm}$	Imp par $< 0.35\,\text{cm}$
37	Impact parameter of X track $< 0.4\,\text{cm}$	Imp par $< 0.45\,\text{cm}$
38	$p_T(X\text{track}) > 0.15\,\text{GeV}$	$p_T(X) > 0.125\,\text{GeV}$
39	$p_T(X\text{track}) > 0.15\,\text{GeV}$	$p_T(X) > 0.175\,\text{GeV}$
40	$\lvert\eta\rvert$ of X track < 1.75	$\lvert\eta\rvert < 1.6$
41	Discriminant cut 0.85 (D^+), 0.9 (D_s)	Cut - 0.05
42	Discriminant cut 0.85 (D^+), 0.9 (D_s),	Cut + 0.05
43	MC used for extraction: DJANGOH	RAPGAP
44	D^+ and D_s reflections	-1σ
45	Luminosity	3.5% error

Table 9.1: List of variations of selection criteria used to estimate the systematic uncertainty. See sections 9.2 and 9.3 for explanations of the cuts.

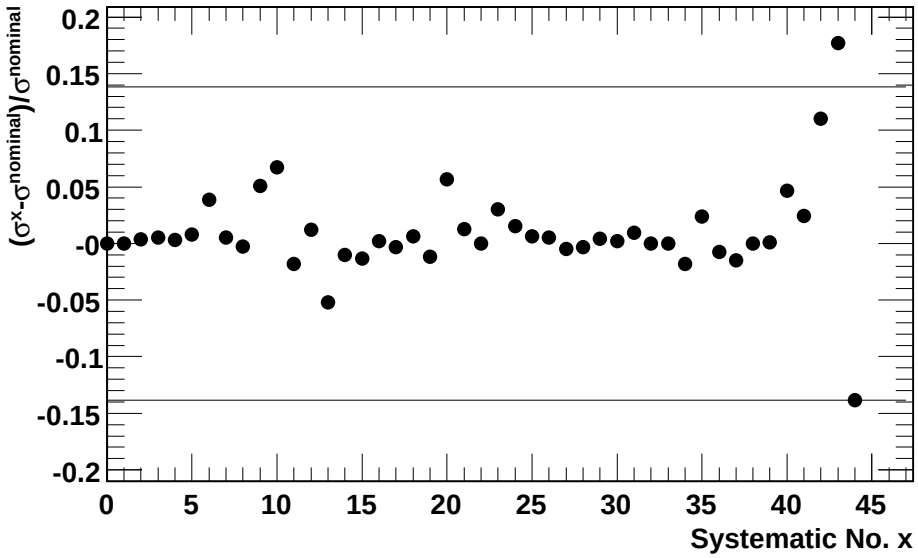


Figure 9.5: Percentage differences in the D^+ cross section caused by each systematic check. See Table 9.1 for the key. The horizontal lines correspond to the statistical error on the nominal cross section.

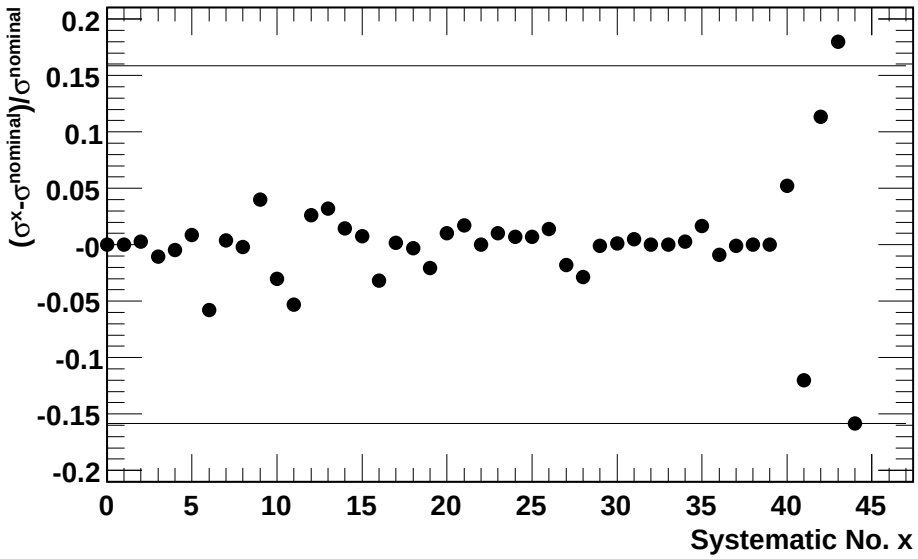


Figure 9.6: Percentage differences in the D_s cross section caused by each systematic check. See Table 9.1 for the key. The horizontal lines correspond to the statistical error on the nominal cross section.

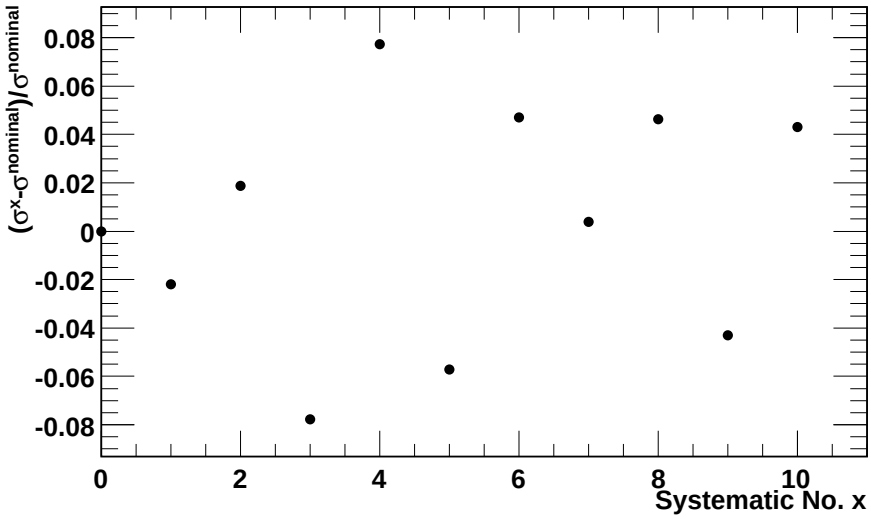


Figure 9.7: Percentage differences in the NLO prediction for the D^+ cross section caused by changing the input parameters. See Table 8.2 for the key.

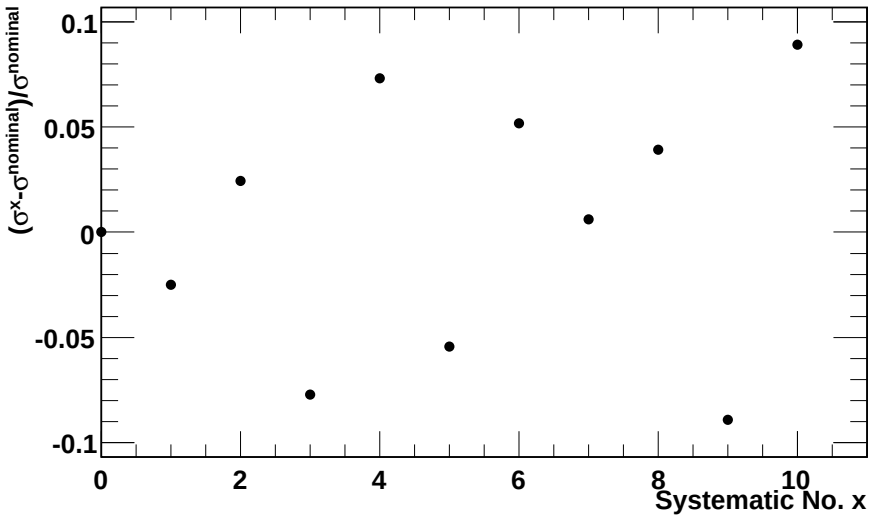


Figure 9.8: Percentage differences in the NLO prediction for the D_s cross section caused by changing the input parameters. See Table 8.2 for the key.

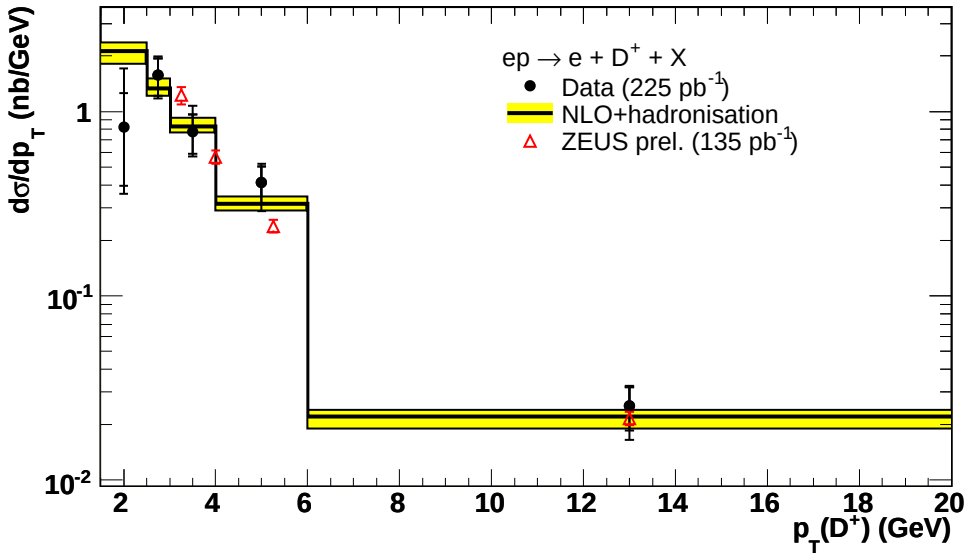


Figure 9.9: Comparison of the D^+ differential cross section in p_T obtained in this analysis (solid circles) to the results of [56] (open triangles). See Figure 9.10 for an explanation of the symbols.

uncertainties are however included in the integrated cross section. Plots of the bin-by-bin efficiency, acceptance and purity for each variable for both decays can be found in Appendix A.2. Plots showing the percentage changes in the cross section as a result of the systematic checks can be found in Appendix A.3.

The NLO predictions provide a good description of the data for all variables over the whole kinematic region. Note that the lower p_T limit of 1.5 GeV represents an extension of the kinematic region compared to previous ZEUS analyses, which have typically used a lower bound of 2 or 3 GeV for both the D^+ and D_s.

A measurement has recently been made of the D^+ cross section in HERA-II data using the $D^+ \to K\pi\pi$ decay channel [56]. The lower limit on the p_T of the D^+ was 3 GeV, which means that only the differential cross section in p_T can be directly compared to the results obtained in this thesis. This comparison is shown in Figure 9.9. The two sets of results are consistent with each other.

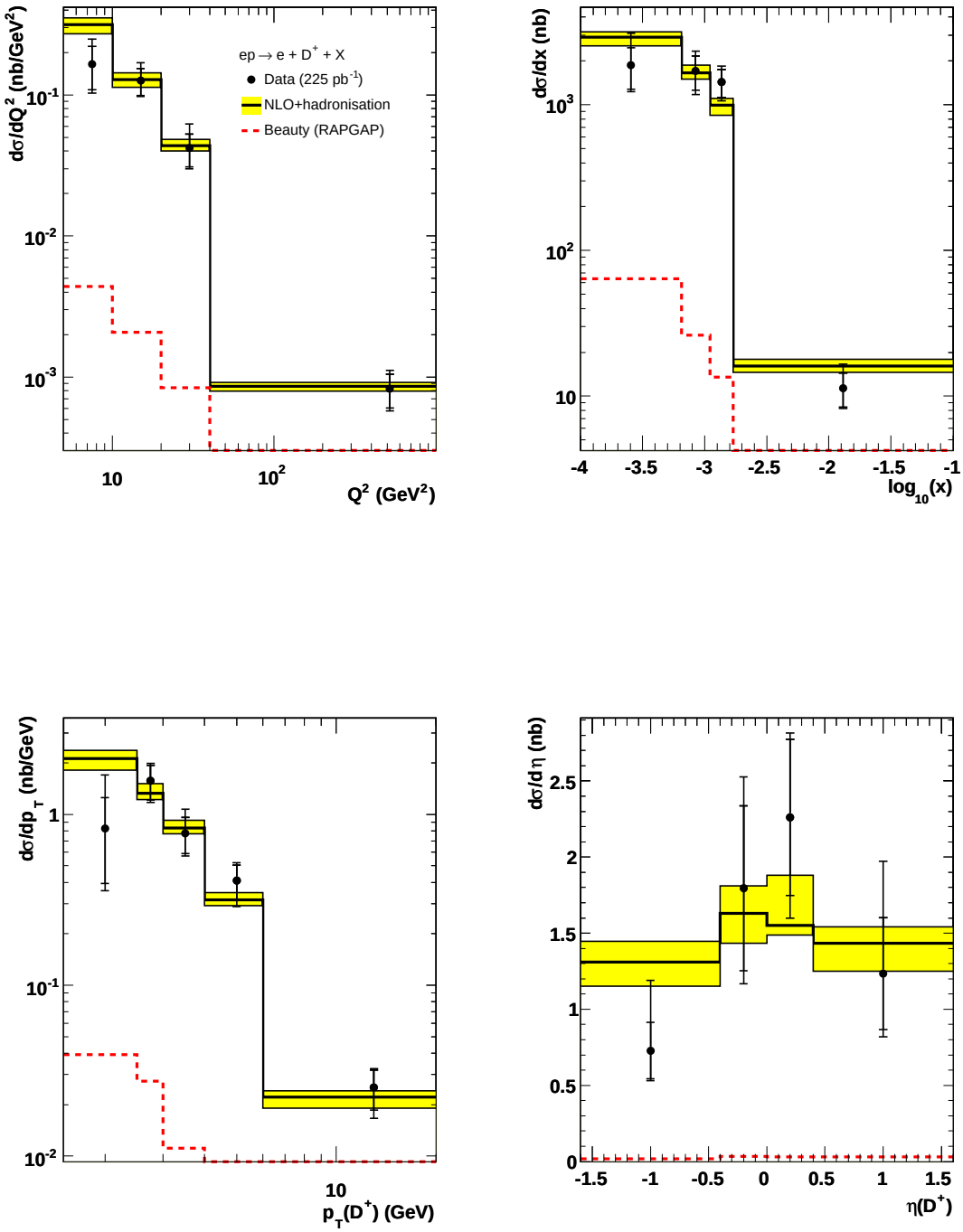


Figure 9.10: D^+ differential cross sections: $\mathrm{d}\sigma/\mathrm{d}Q^2$, $\mathrm{d}\sigma/\mathrm{d}x$, $\mathrm{d}\sigma/\mathrm{d}p_T(D^+)$, and $\mathrm{d}\sigma/\mathrm{d}\eta(D^+)$. The inner error bars are statistical only, the outer bars are the statistical and systematic errors added in quadrature. The solid band corresponds to the systematic uncertainties on the HVQDIS NLO prediction as described in Section 8.8.2. The dashed line indicates the contribution from beauty decays as predicted by RAPGAP Monte Carlo. Uncertainties on the luminosity measurement and branching ratio are not included.

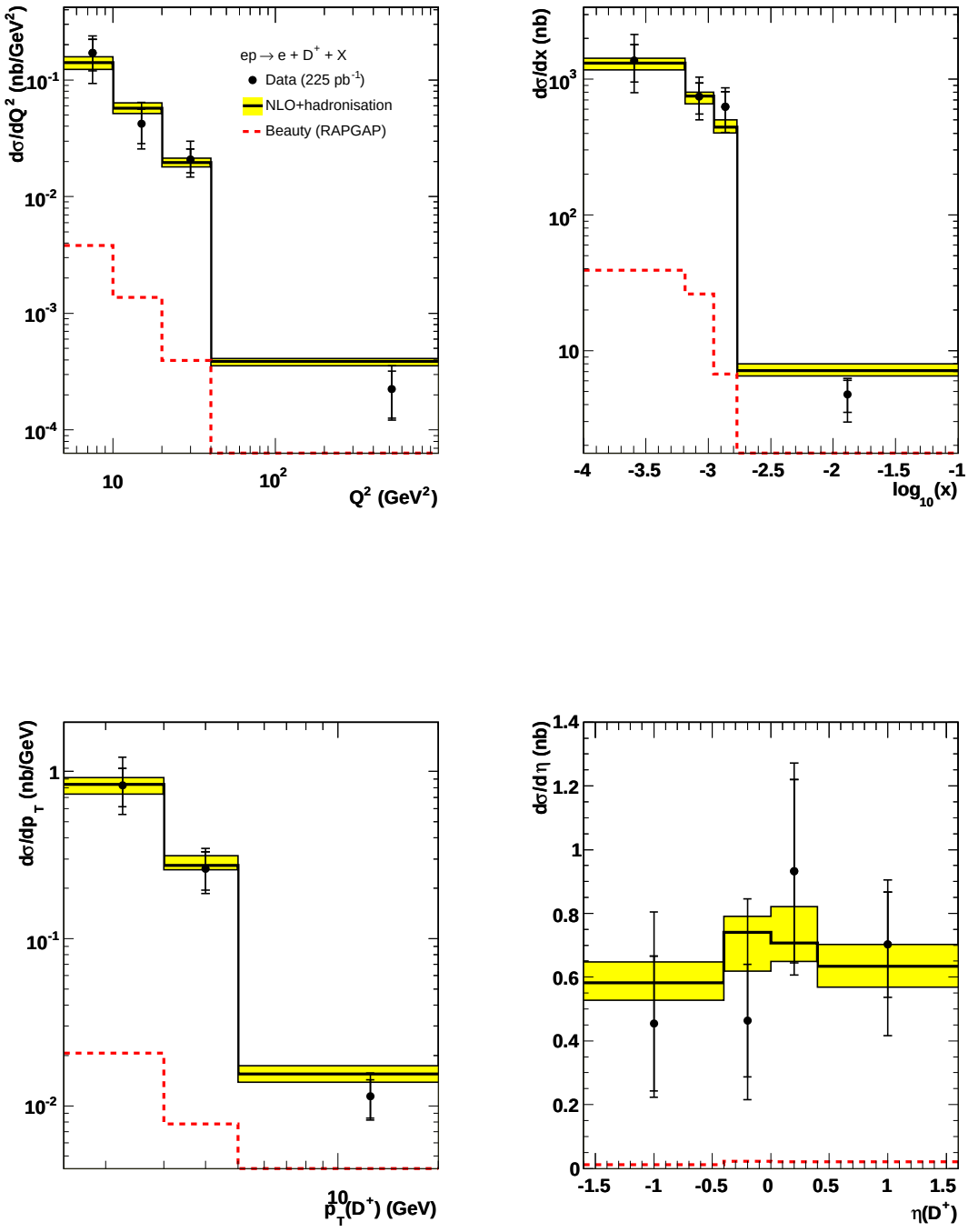


Figure 9.11: D_s differential cross sections: $\mathrm{d}\sigma/\mathrm{d}Q^2$, $\mathrm{d}\sigma/\mathrm{d}x$, $\mathrm{d}\sigma/\mathrm{d}p_T(D_s)$, and $\mathrm{d}\sigma/\mathrm{d}\eta(D_s)$. The inner error bars are statistical only, the outer bars are the statistical and systematic errors added in quadrature. The solid band corresponds to the systematic uncertainties on the HVQDIS NLO prediction as described in Section 8.8.2. The dashed line indicates the contribution from beauty decays as predicted by RAPGAP Monte Carlo. Uncertainties on the luminosity measurement and branching ratio are not included.

Q^2 bin (GeV^2)	$\mathrm{d}\sigma/\mathrm{d}Q^2$	Δ_{stat} ($\mathrm{nb}/\mathrm{GeV}^2$)	Δ_{syst}	$\mathrm{d}\sigma^{NLO}/\mathrm{d}Q^2$ ($\mathrm{nb}/\mathrm{GeV}^2$)	$\Delta^{NLO}_{\mathrm{syst}}$
5, 10	0.165	± 0.057	$^{+0.062}_{-0.026}$	0.317	$^{+0.036}_{-0.044}$
10, 20	0.127	± 0.028	$^{+0.033}_{-0.011}$	0.128	$^{+0.015}_{-0.015}$
20, 40	0.042	± 0.011	$^{+0.017}_{-0.0045}$	0.0436	$^{+0.0048}_{-0.0034}$
40, 1000	0.00082	± 0.00022	$^{+0.00018}_{-0.00011}$	0.000860	$^{+0.000053}_{-0.000063}$
x bin	$\mathrm{d}\sigma/\mathrm{d}x$	Δ_{stat} (nb)	Δ_{syst}	$\mathrm{d}\sigma^{NLO}/\mathrm{d}x$ (nb)	$\Delta^{NLO}_{\mathrm{syst}}$
0.0001, 0.00065	1877	± 596	$^{+1066}_{-240}$	2919	$^{+250}_{-374}$
0.00065, 0.0011	1713	± 451	$^{+422}_{-292}$	1655	$^{+224}_{-155}$
0.0011, 0.0017	1438	± 316	$^{+265}_{-193}$	995	$^{+113}_{-144}$
0.0017, 0.1	11.4	± 2.9	$^{+4.4}_{-1.1}$	16.1	$^{+1.8}_{-1.6}$
$p_T(D^+)$ bin (GeV)	$\mathrm{d}\sigma/\mathrm{d}p_T(D^+)$	Δ_{stat} (nb/GeV)	Δ_{syst}	$\mathrm{d}\sigma^{NLO}/\mathrm{d}p_T(D^+)$ (nb/GeV)	$\Delta^{NLO}_{\mathrm{syst}}$
1.5, 2.5	0.82	± 0.43	$^{+0.77}_{-0.18}$	2.13	$^{+0.24}_{-0.31}$
2.5, 3	1.57	± 0.36	$^{+0.20}_{-0.18}$	1.33	$^{+0.18}_{-0.11}$
3, 4	0.78	± 0.19	$^{+0.23}_{-0.084}$	0.83	$^{+0.091}_{-0.062}$
4, 6	0.411	± 0.092	$^{+0.060}_{-0.080}$	0.316	$^{+0.032}_{-0.024}$
6, 20	0.0252	± 0.0066	$^{+0.0029}_{-0.0055}$	0.0221	$^{+0.0020}_{-0.0031}$
$\eta(D^+)$ bin	$\mathrm{d}\sigma/\mathrm{d}\eta(D^+)$	Δ_{stat} (nb)	Δ_{syst}	$\mathrm{d}\sigma^{NLO}/\mathrm{d}\eta(D^+)$ (nb)	$\Delta^{NLO}_{\mathrm{syst}}$
-1.6, -0.4	0.73	± 0.18	$^{+0.42}_{-0.069}$	1.31	$^{+0.14}_{-0.16}$
-0.4, 0	1.80	± 0.54	$^{+0.49}_{-0.32}$	1.63	$^{+0.18}_{-0.20}$
0, 0.4	2.26	± 0.51	$^{+0.21}_{-0.42}$	1.55	$^{+0.33}_{-0.064}$
0.4, 1.6	1.23	± 0.37	$^{+0.64}_{-0.20}$	1.43	$^{+0.11}_{-0.18}$

Table 9.2: Values of D^+ differential cross sections. The lefthand column gives the binning, the middle three columns are the measured values with their associated uncertainties, the rightmost two columns are the NLO predictions from HVQDIS, with their uncertainties. Uncertainties on the luminosity and branching ratio (for data) and the hadronisation fraction (for NLO) are not included.

Q^2 bin (GeV^2)	$\mathrm{d}\sigma/\mathrm{d}Q^2$	Δ_{stat} ($\mathrm{nb}/\mathrm{GeV}^2$)	Δ_{syst}	$\mathrm{d}\sigma^{NLO}/\mathrm{d}Q^2$ ($\mathrm{nb}/\mathrm{GeV}^2$)	$\Delta^{NLO}_{\mathrm{syst}}$
5, 10	0.170	± 0.051	$^{+0.044}_{-0.058}$	0.141	$^{+0.017}_{-0.018}$
10, 20	0.042	± 0.014	$^{+0.017}_{-0.0094}$	0.0572	$^{+0.0064}_{-0.0057}$
20, 40	0.0208	± 0.0048	$^{+0.0075}_{-0.0038}$	0.0195	$^{+0.0019}_{-0.0015}$
40, 1000	0.000224	± 0.000098	$^{+0.000088}_{-0.000031}$	0.000386	$^{+0.000023}_{-0.000030}$
x bin	$\mathrm{d}\sigma/\mathrm{d}x$	Δ_{stat} (nb)	Δ_{syst}	$\mathrm{d}\sigma^{NLO}/\mathrm{d}x$ (nb)	$\Delta^{NLO}_{\mathrm{syst}}$
0.0001, 0.00065	1372	± 418	$^{+639}_{-392}$	1309	$^{+120}_{-143}$
0.00065, 0.0011	746	± 191	$^{+211}_{-151}$	753	$^{+49}_{-93}$
0.0011, 0.0017	626	± 183	$^{+151}_{-124}$	445	$^{+59}_{-42}$
0.0017, 0.1	4.77	± 1.27	$^{+0.75}_{-1.28}$	7.15	$^{+0.84}_{-0.64}$
$p_T(D_s)$ bin (GeV)	$\mathrm{d}\sigma/\mathrm{d}p_T(D^s)$	Δ_{stat} (nb/GeV)	Δ_{syst}	$\mathrm{d}\sigma^{NLO}/\mathrm{d}p_T(D^s)$ (nb/GeV)	$\Delta^{NLO}_{\mathrm{syst}}$
1.5, 3.0	0.83	± 0.21	$^{+0.32}_{-0.17}$	0.84	$^{+0.080}_{-0.11}$
3.0, 5.0	0.262	± 0.067	$^{+0.051}_{-0.037}$	0.274	$^{+0.040}_{-0.016}$
5.0, 20.0	0.0114	± 0.0029	$^{+0.0031}_{-0.0012}$	0.0156	$^{+0.0019}_{-0.0017}$
$\eta(D_s)$ bin	$\mathrm{d}\sigma/\mathrm{d}\eta(D_s)$	Δ_{stat} (nb)	Δ_{syst}	$\mathrm{d}\sigma^{NLO}/\mathrm{d}\eta(D_s)$ (nb)	$\Delta^{NLO}_{\mathrm{syst}}$
-1.6, -0.4	0.45	± 0.21	$^{+0.28}_{-0.093}$	0.58	$^{+0.065}_{-0.056}$
-0.4, 0.0	0.46	± 0.18	$^{+0.34}_{-0.18}$	0.74	$^{+0.049}_{-0.12}$
0.0, 0.4	0.93	± 0.29	$^{+0.18}_{-0.15}$	0.71	$^{+0.11}_{-0.058}$
0.4, 1.6	0.71	± 0.17	$^{+0.12}_{-0.23}$	0.63	$^{+0.069}_{-0.066}$

Table 9.3: Values of D_s differential cross sections. The lefthand column gives the binning, the middle three columns are the measured values with their associated uncertainties, the rightmost two columns are the NLO predictions from HVQDIS, with their uncertainties. Uncertainties on the luminosity and branching ratio (for data) and the hadronisation fraction (for NLO) are not included.

9.7 Strangeness-Suppression Factor

Having measured cross sections for D^0, D^+ and D_s it is possible to determine the strangeness-suppression factor, γ_s. This is the ratio of the probability for getting a strange quark from the vacuum to that of getting an up or down quark. In boson–gluon fusion the charm quark is produced in the hard scatter, and forms a meson by picking up a light quark ('$\overline{u}$', '$\overline{d}$' or '$\overline{s}$') from the sea, i.e. the vacuum fluctuations of $q\bar{q}$ pairs. Thus the strangeness-suppression factor can be calculated in the charm sector from the production rate of charm-strange mesons divided by half the production rate of non-strange charm mesons, where the factor of one half comes from averaging over the u and d quarks. Thus γ_s may be defined as

$$\gamma_s = \frac{2(N^{dir}(D_s^{\pm}) + N^{exc}(D_s^{\pm}))}{N^{dir}(D^{\pm}) + N^{exc}(D^{\pm}) + N^{dir}(D^0) + N^{exc}(D^0)}, \tag{9.7}$$

where $N^{dir}(D_s^{\pm})$ denotes the number of D_s mesons directly produced from the fragmentation of the charm quark, i.e. excluding those from decays of excited states, $N^{exc}(D_s^{\pm})$ is the number of excited charm-strange mesons, i.e. $D_s^{*\pm}$ and higher excited states, and likewise for $N^{dir,exc}(D^{\pm})$ and $N^{dir,exc}(D^0)$. The numbers of events are corrected for the acceptance and branching ratio. However all $D_s^{*\pm}$ decay to $D_s^{\pm}$, and all $D^{*\pm}$ and D^{*0} to $D^{\pm}$ or D^0; the higher excitations also follow similar trends. Since we have not considered the source of the mesons when measuring them in this thesis the expression for γ_s reduces to

$$\gamma_s = \frac{2N(D_s)}{N(D^{\pm}) + N(D^0)}. \tag{9.8}$$

This neglects any decays of excited charm-strange mesons to non-strange charm mesons, following the procedure of the analyses quoted in Table 9.5. Such decays occur for $D_{s1}(2536)^{\pm}$ and $D_{s2}(2573)^{\pm}$ which decay only to non-strange charm mesons (with the exception of a '*possibly seen*' $D_s^{*+}\gamma$ decay for the D_{s1}) [1]. The hadronisation fractions $f(c \to D_{s1})$ and $f(c \to D_{s2})$ have been measured at LEP in 2002 to be $(0.94 \pm 0.22\,(\text{stat}) \pm 0.07(\text{syst}))$ % and $(1.14 \pm 0.59\,(\text{stat})^{+0.11}_{-0.20}\,(\text{syst}))$% respectively [57].

Systematic No.	D^0 systematic	D^+, D_s systematic
1 – 33	as in Table 8.1	as in Table 9.1
34 – 41	as in Table 8.1	nominal value
42	as in Table 8.1	systematic 43 from Table 9.1
43 – 51	nominal value	systematics 34 – 42 from Table 9.1
52	nominal value	systematic 44 from Table 9.1

Table 9.4: Key to systematics used for γ_s measurement.

Given that the hadronisation fraction $f(c \to D_s)$ is $(10.1 \pm 0.09)\%$, this suggests neglecting such decays could have a $\sim 10\%$ effect. This level of disagreement is within the experimental error for all of the quoted measurements however.

The value of γ_s determined from the numbers of events measured in this thesis, neglecting the $D_{s1}(2536)^{\pm}$ and $D_{s2}(2573)^{\pm}$, is

$$\gamma_s = 0.244 \pm 0.054\,(\text{stat.})^{+0.039}_{-0.052}\,(\text{syst.})^{+0.034}_{-0.030}(\text{BR})$$

where the D^0 cross section has been restricted to the same kinematic region as the D_s and D^+ cross sections.

The upper and lower systematic uncertainties were not taken from the systematic errors given above for each individual cross section, but recalculated. This has the advantage that errors in quantities contributing in the same way to both the numerator and denominator (e.g. luminosity) cancel, giving a more precise result. The upper (lower) systematic error is found by adding in quadrature the positive (negative) differences of the ratio from the nominal value for each of the systematic checks. Where a systematic check for the D^0 did not correspond directly to a systematic check for the D_s and D^+ the value used for the D^0 cross section in the ratio was set to the nominal value, and vice versa. This is summarised in Table 9.4. The percentage differences with respect to the nominal value are shown in Figure 9.12.

The upper (lower) uncertainty for the branching ratio was obtained by increasing (decreasing) the number of D_s by the percentage error on the branching ratio while decreasing (increasing) the numbers of D^+ and D^0 by the errors on their branching

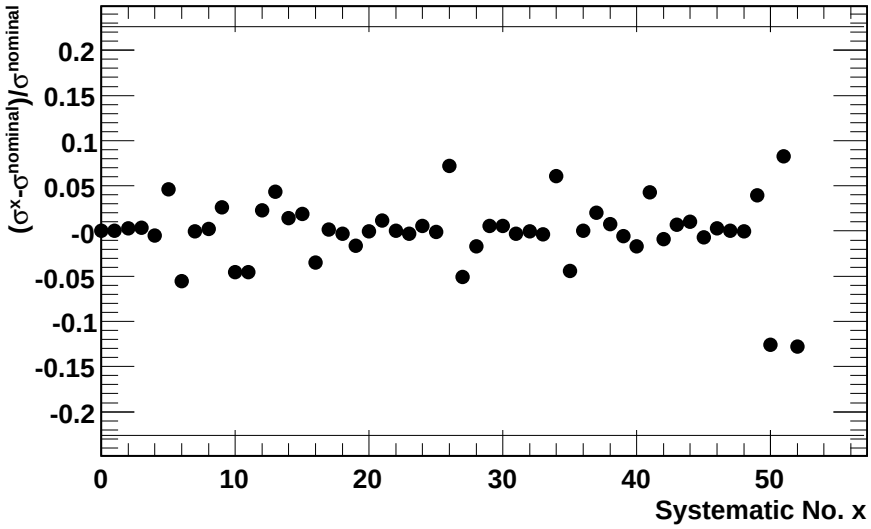


Figure 9.12: Percentage differences in the value of γ_s caused by each systematic check. The horizontal lines correspond to the statistical error on the nominal value.

ratios.

Values for γ_s were also calculated from the number of true decays in the Monte Carlo. DJANGOH gave a value of $\gamma_s = 0.208$, while RAPGAP gave 0.210, both of which are slightly below the measured value, although consistent within errors. Both of these Monte Carlo programs use the Lund model for fragmentation, which has γ_s as a free parameter. The default value of 0.3 was used.

Previous measurements of γ_s at ZEUS and other experiments using charm meson cross sections are presented in Table 9.5. All results including that of this thesis agree within errors.

	γ_s
ZEUS (DIS) [36]	$0.225 \pm 0.030(\text{stat.})^{+0.018}_{-0.007}(\text{syst.})^{+0.034}_{-0.026}(\text{br.})$
ZEUS (γp) [37]	$0.257 \pm 0.024(\text{stat.})^{+0.013}_{-0.016}(\text{syst.})^{+0.078}_{-0.049}(\text{br.})$
ZEUS (γp) [58]	$0.27 \pm 0.04(\text{stat.})^{+0.02}_{-0.03}(\text{syst.}) \pm 0.07(\text{br.})$
combined e^+e^- data	$0.259 \pm 0.023(\text{stat.} \oplus \text{syst.})^{+0.087}_{-0.052}(\text{br.})$
H1 (DIS) [59]	$0.36 \pm 0.10(\text{stat.}) \pm 0.01(\text{syst.}) \pm 0.08(\text{br.} \oplus \text{theory})$

Table 9.5: Experimental values for the strangeness-suppression factor in charm fragmentation, γ_s. (Taken from [36].)

Chapter 10

$\Lambda_c \to \Lambda^0\pi$ Decay Channel

10.1 Introduction

While a signal for the Λ_c could not be seen in the $K^0_s p$ decay channel, this was not the only channel in which it was sought. The decay

$$\Lambda_c^{\pm} \to \Lambda^0\pi^{\pm} \to p^{\pm}\pi^{\mp}\pi^{\pm} \tag{10.1}$$

which has the same topology (i.e. a two-track vertex plus another track), and results in the same three particles, two pions and a proton, was also investigated. This channel turned out to be more fruitful, and a Λ_c signal was obtained.

This channel also offers other advantages over the $K^0_s p$ channel. Because of the kinematic cuts used the proton from the Λ^0 decay will have the larger momentum of the two daughter tracks. This allows us to identify which of the tracks is the proton. Furthermore, in the parity-violating decay $\overleftarrow{\Lambda^0} \to \overleftarrow{p}\pi^{\pm}$ the proton direction is correlated with the Λ^0 spin direction. This then allows for two polarisation measurements - first the weak decay-asymmetry parameter for the $\Lambda_c \to \Lambda^0\pi$ decay, and second a possible measurement of the spin transfer from the polarised lepton beam to the $\Lambda_c^{\pm}$. Unfortunately in this analysis there were insufficient events to make these measurements.

10.2 $\Lambda_c^{\pm}$ Reconstruction

DIS events are selected in the manner described in sections 8.2 and 8.3. The Λ^0 or $\overline{\Lambda^0}$ in the final state is reconstructed using the same procedure as for the K_s^0 (Section 8.4), except that the track with the larger momentum of the two is assigned the proton mass. Because of the much greater mass of the proton compared to the pion, and the kinematic cuts made on the reconstructed tracks, this assignment will always be correct for reconstructed true lambdas whose momentum is above $\sim 0.3\,\mathrm{GeV}$. The charge of the proton therefore determines whether the candidate is a Λ^0 or $\overline{\Lambda^0}$, however they are not treated separately. The invariant-mass requirements for the track pair are

- $1.11 < M(p\pi) < 1.121\,\mathrm{GeV}$
- $M(\pi\pi) < 0.47\,\mathrm{GeV}$
- $M(ee) > 0.05\,\mathrm{GeV}$.

The Λ_s^0 mass distribution obtained after these cuts is shown in Figure 10.1. The data are fitted with the sum of two gaussians and a first order polynomial, where the functional form is chosen for the same reason as the K_s^0 case (Section 8.4). From the fit there are $107\,000 \pm 3100$ events in the peak, which is located at $(1.11506 \pm 0.00001)\,\mathrm{GeV}$ with a width of $(0.00167 \pm 0.00003)\,\mathrm{GeV}$, The mass agrees with the PDG value of $(1.115683 \pm 0.000006)\,\mathrm{GeV}$, within the 0.3% uncertainty from the magnetic field.

The $\Lambda_c^{\pm}$ candidates are formed by successively combining the Λ^0 candidate with all other tracks in the event which satisfy the same criteria as the X track in Section 9.2, with the additional requirement that the charge of the pion be opposite to that of the (anti-) proton. The discriminant method, with the same variables as for the $K_s^0 X$ case (except for $p(K_s^0)/p(D)$ which becomes $p(\Lambda)/p(\Lambda_c)$), is then used. Due to the comparatively small number of Λ_c's in the existing Monte Carlo samples a further one million events were generated in the channel $\Lambda_c^{\pm} \to \Lambda^0\pi^{\pm}$ for use in the signal distributions of the discriminant; of these approximately 12 000 passed all event and track cuts.

A comparison of the discriminant distribution for signal and background events for $\Lambda_c^{\pm}$ in the Monte Carlo is shown in Figure 10.2. The signal distribution exhibits a peak at

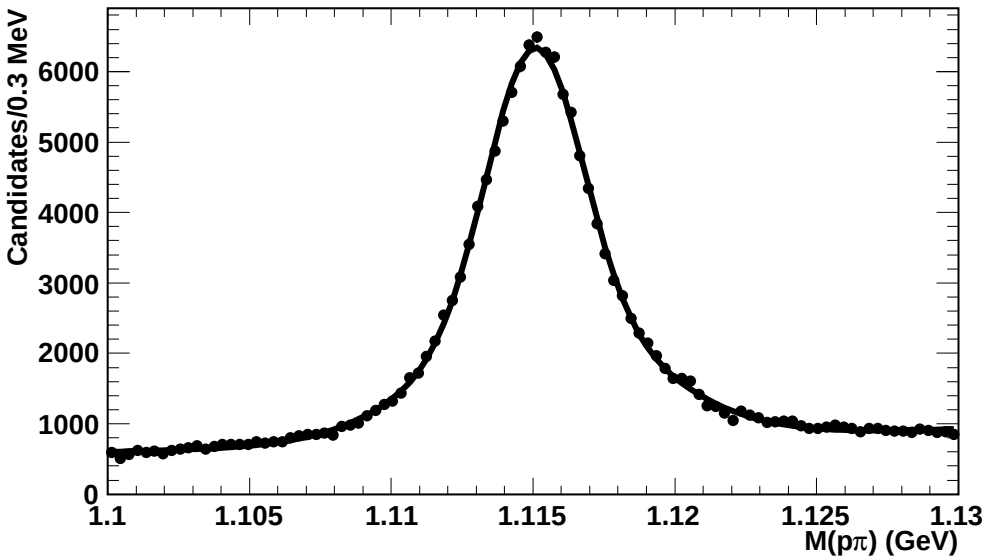


Figure 10.1: Λ^0 mass peak. The points are the data, the solid line is a fit to the sum of two gaussians and a first order polynomial.

1 while the background distribution is flatter. The discriminant cut used for the $\Lambda_c^{\pm}$ was chosen to be 0.75. From looking at where the signal distribution crosses the background distribution on the plot a higher cut might be recommended, however due to the small cross section for the decay a lower cut was needed to improve the efficiency. The value of 0.75 was chosen because this is point where the signal distribution starts rising.

10.3 Integrated Cross Section

The integrated cross section for $\Lambda_c^{\pm}$ in the kinematic region $5 < Q^2 < 1000\,\mathrm{GeV}^2$, $0.02 < y < 0.7$, $1.5 < p_T(\Lambda_c^{\pm}) < 20.0\,\mathrm{GeV}$, $|\eta(\Lambda_c^{\pm})| < 1.6$ was determined using the same unfolding procedure as described in section 8.6 to be

$$\sigma(\Lambda_c) = 0.92 \pm 0.39\,(\mathrm{stat.})^{+0.49}_{-0.27}\,(\mathrm{syst.}) \pm 0.26(\mathrm{BR})\ \mathrm{nb}$$

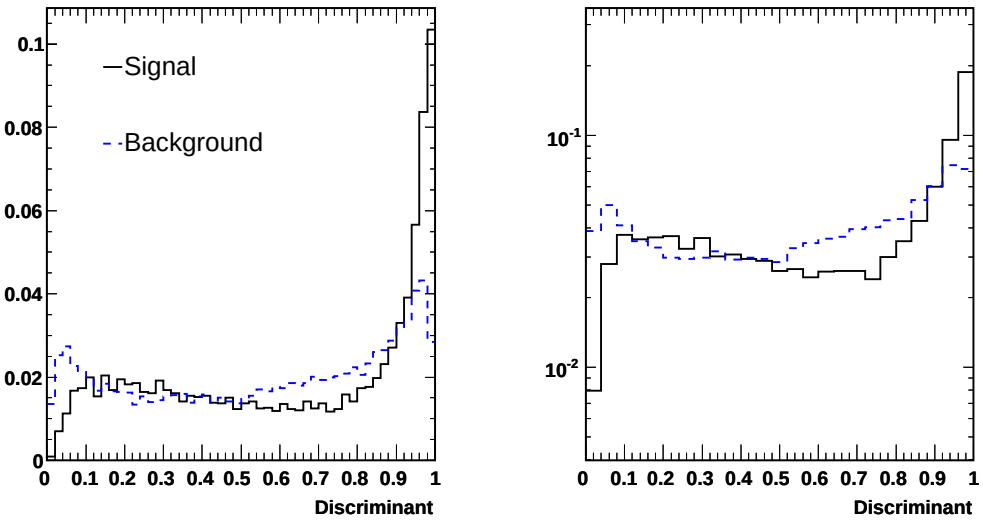


Figure 10.2: Plots comparing the discriminant distributions for true decays of Λ_c (solid lines) and background candidates (dashed lines) in MC. The left hand plot uses a linear scale, the right hand plot a logarithmic scale. The signal and background distributions are normalised to the same area.

The NLO prediction from HVQDIS for the cross section in the same kinematic region is

$$\sigma^{NLO}(\Lambda_c) = 1.57\,^{+0.24}_{-0.19}\,(\text{syst.})\ \text{nb}$$

The central value for the data is lower than the HVQDIS prediction, but agrees within the rather large experimental errors.

The total efficiency was 5.6%, the purity 100% and the acceptance 5.6%.

The branching ratio used was

$$\begin{aligned} B(\Lambda_c^+ \to \Lambda^0\pi^+ \to p\pi^-\pi^+) &= B(\Lambda_c^+ \to \Lambda^0\pi^+) \times B(\Lambda^0 \to p\pi^-) \\ &= (0.65 \pm 0.18)\% \end{aligned} \tag{10.2}$$

There were insufficient events to be able to measure differential cross sections.

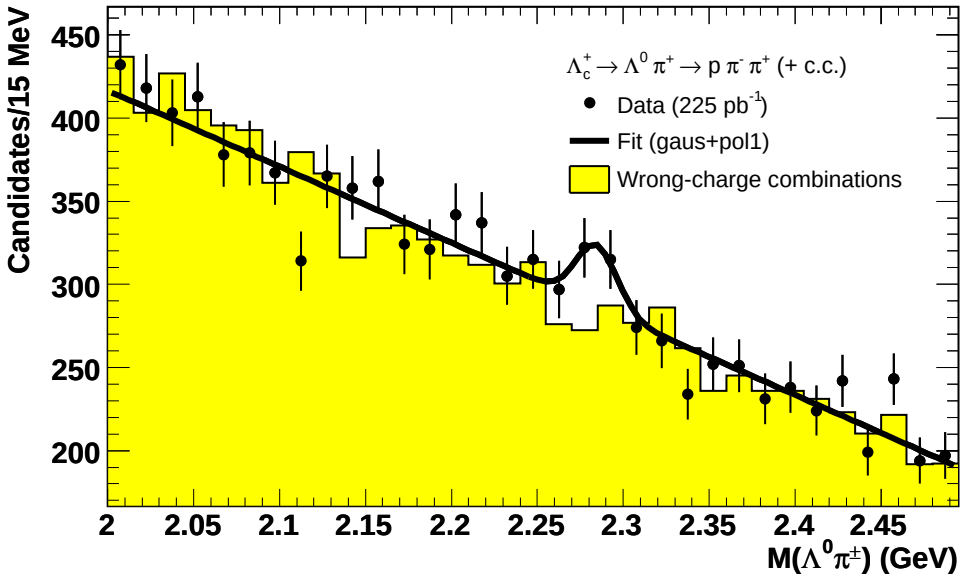


Figure 10.3: Λ_c mass spectra obtained with a discriminant cut of 0.75. The points are the measured data. The solid line corresponds to a gaussian plus first-order-polynomial fit. The histogram is the mass distribution for wrong-charge candidates, i.e those for which the two pions have the same charge, normalised to the data distribution in the region $(2.33, 2.50)$ GeV.

10.3.1 Fit to Mass Distribution

The central value together with the statistical error for the cross section was determined from a fit to the mass spectrum shown in Figure 10.3, where the fitting function had the form

$$f(x) = p_1 \exp\left(-\frac{1}{2}\left(\frac{x - p_2}{p_3}\right)^2\right) + p_4 + p_5 x, \tag{10.3}$$

with $p_1 - p_5$ being free parameters. The Λ_c mass peak is located at (2.285 ± 0.006) GeV, with a width of (0.012 ± 0.008) GeV and contains 75 ± 31 events. However, because of the small number of events in the peak it was often difficult to get the fit to converge with all parameters free. Therefore when fitting the mass peaks for the various systematics the width of the gaussian (p_3) was fixed to the value obtained from the fit to the nominal distribution.

Other analyses which have measured the Λ_c in this channel (e.g.[60]) take into account when performing the fit the presence of other decay modes which can mimic the same topology. The decays

$$\Lambda_c^{\pm} \rightarrow \Sigma^0 \pi^{\pm} \rightarrow \Lambda^0 \gamma \pi^{\pm}, \tag{10.4}$$

and

$$\Lambda_c^{\pm} \rightarrow \Lambda^0 \pi^{\pm} \pi^0, \tag{10.5}$$

where the γ and the π^0 respectively are not observed will contribute to the measured $\Lambda^0\pi^{\pm}$ mass distribution.

Figure 10.4 shows the $\Lambda\pi$ invariant mass distribution from Monte Carlo for true decays of Λ_c in the $\Lambda\pi$, $\Sigma\pi$ channel and $\Lambda\pi\pi^0$ channels which have passed all the analysis cuts. This suggests that the $\Lambda\pi\pi^0$ channel may give a small change in slope at lower invariant mass (although given the size of this relative to the $\Lambda\pi$ peak and the size of this peak relative to the background this effect is likely to be negligible in our case), and that the $\Sigma\pi$ channel should give a peak of the same order of magnitude as the $\Lambda\pi$ channel.

A small peak can indeed be seen at around 2.2 GeV in the measured distribution. Attempts were made to fit the whole $\Lambda\pi$ invariant mass distribution with the sum of a first-order polynomial and two gaussians. This would not converge with all parameters free. Each of the two peaks was then fit with a first-order polynomial plus a single gaussian, and with careful choice of parameters these were successful. The whole distribution could be fit with a first-order polynomial and two gaussians if the widths of the gaussians were fixed to the values obtained from the separate fits (which were 0.0091 GeV for the $\Sigma\pi$ channel and 0.0113 GeV for the $\Lambda\pi$ channel). The result of such a fit is shown in Figure 10.5. Since the widths had to be constrained the number of events in the $\Lambda\pi$ peak when fitting both peaks is the same as when just fitting the one peak. Thus given the statistical limitations there does not appear to be any advantage in attempting to include the $\Sigma\pi$ peak in the fit. It may also be noted in passing that the width obtained for the $\Sigma\pi$ peak from the fit is narrower than for the $\Lambda\pi$ peak, while Figure 10.4 suggests

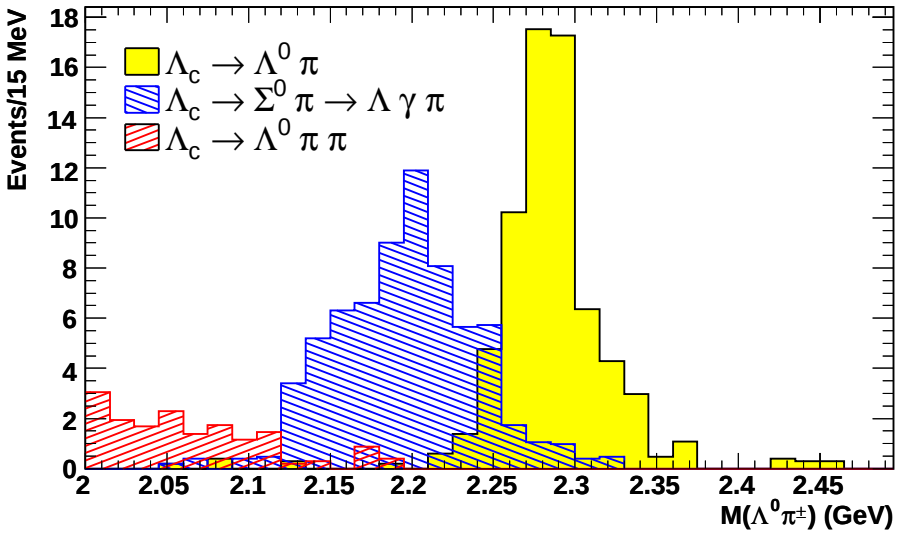


Figure 10.4: The $\Lambda\pi$ invariant mass distribution from Monte Carlo for true decays of Λ_c in the $\Lambda\pi$ channel (solid histogram), $\Sigma\pi$ channel (\\ hatching) and $\Lambda\pi\pi^0$ channel (// hatching). The latter two modes may need to be taken into account when trying to extract the $\Lambda_c \to \Lambda\pi$ peak from the $\Lambda\pi$ mass distribution.

it should be broader. This raises the question of whether what we have been trying to fit is in fact the expected peak.

10.3.2 Wrong-Charge Background

Since the daughters of the Λ^0 are not of the same species and since the $\Lambda/\overline{\Lambda}$ ambiguity is resolved by assigning the proton mass to the highest momentum track, it is possible to create *wrong-charge candidates* which pass all the selection cuts as for Λ_c candidates, differing only in the sign of the charge of one of the tracks. Since these candidates cannot correspond to real Λ_c decays they can be used to estimate the background. The wrong-charge combinations are shown as the solid histogram in Figure 10.3 where they have been normalised to the data in the interval $(2.33, 2.5)$ GeV. The reason for not normalising the distribution in the region below the Λ_c peak is the presence of background from other decay modes as mentioned in the previous section, however if one does so the results are

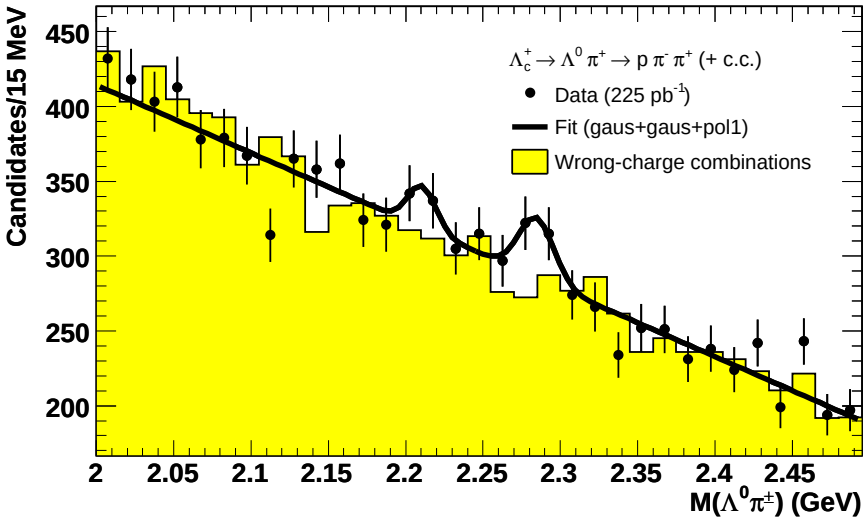


Figure 10.5: Plot of the $\Lambda\pi$ invariant mass distribution. The fit is the sum of two gaussians and a first order polynomial. The widths of the gaussians were fixed at 0.0091 GeV for the peak at 2.21 GeV ($\Sigma\pi$ channel) and 0.0113 GeV for the peak at 2.28 GeV ($\Lambda\pi$ channel).

essentially identical.

A clear peak in the data over the wrong-charge combinations can be seen at the Λ_c mass. Subtracting the normalised wrong-charge histogram from the right-charge histogram in the peak region provides an alternative means of estimating the number of Λ_c's in the sample. Because of the small number of bins in which the peak is contained in this particular case, wrong-charge subtraction is highly sensitive to the bins used. Taking bins 18 – 21 in Figure 10.3, which more or less cover the full extent of the peak, gives a value of 95 ± 48 Λ_c's in the peak, where the errors are Poissonian. This is consistent with the value obtained from the fit of 75 ± 31.

10.4 Systematic Errors

The experimental systematic errors for the Λ_c were evaluated in the same way as for the $D \rightarrow K^0_s$ channel, with the exceptions that the K^0_s and Λ^0 masses were interchanged,

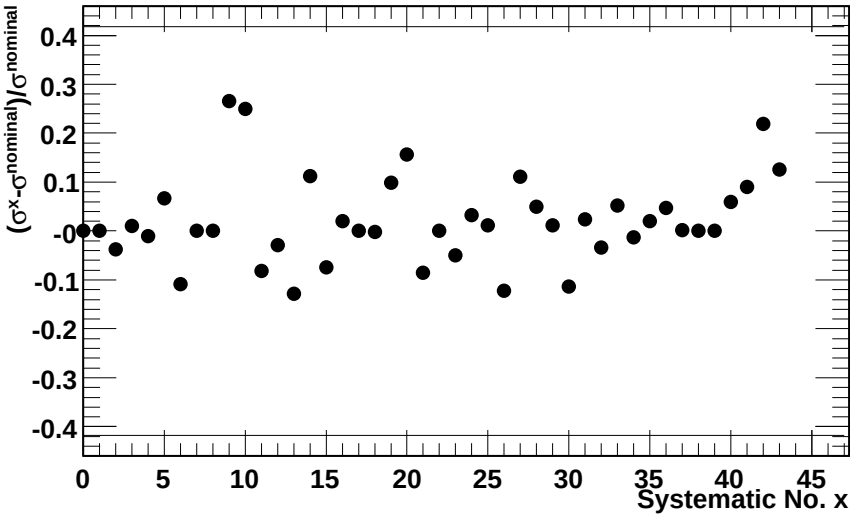


Figure 10.6: Percentage differences in the Λ_c cross section caused by each systematic check. See Table 10.1 for the key. The horizontal lines correspond to the statistical error on the nominal cross section.

and no error was added for reflections from $D^{\pm}$ or $D_s^{\pm}$ as Monte Carlo studies showed that there were none. For completeness the table of systematic checks is listed below. The results of these checks can be seen in Figure 10.6.

The theoretical systematics follow the same prescription as in the previous two chapters. The hadronisation fraction used was 0.076 ± 0.007. The effects of these systematic checks are shown in Figure 10.7.

10.5 Baryon-to-Meson Ratio

Having measured the Λ_c cross section it is now possible to calculate the charm baryon-to-meson ratio. This quantity may provide used to investigate the production mechanisms for charmed hadrons, and can be defined as[1]

$$\mathcal{R} = \frac{N(\Lambda_c)}{N(D^{\pm}) + N(D^0)}. \tag{10.6}$$

[1]The D_s meson is excluded so that we are only comparing particles with the same quark flavours.

#	**Nominal value**	**Variation**
1	$y_{electron} < 0.95$	$y_{el} < 0.90$
2	$y_{JB} > 0.02$	$y_{JB} > 0.03$
3	$40 < E - p_z < 70\,\text{GeV}$	$42 < E - pz < 65\,\text{GeV}$
4	$\lvert Z_{vtx}\rvert < 50\,\text{cm}$	$\lvert Z_{vtx}\rvert < 45\,\text{cm}$
5	$E_e > 10\,\text{GeV}$	$E_e > 11\,\text{GeV}$
6	Boxcut 15 cm	Boxcut 16 cm
7	Electron energy scale (MC only)	$E_e \times 0.98$
8	Electron energy scale (MC only)	$E_e \times 1.02$
9	Hadronic energy scale (MC only)	Energy$\times$0.97
10	Hadronic energy scale (MC only)	Energy$\times$1.03
11	$1.110 < M(\Lambda) < 1.121\,\text{GeV}$	$1.109 < M(\Lambda) < 1.122\,\text{GeV}$
12	$1.110 < M(\Lambda) < 1.121\,\text{GeV}$	$1.111 < M(\Lambda) < 1.120\,\text{GeV}$
13	Impact parameter $> 0.05\,\text{cm}$	Imp par $> 0.04\,\text{cm}$
14	Impact parameter $> 0.05\,\text{cm}$	Imp par > 0.06 cm
15	Λ vertex: $x^2 + y^2 < 400\,\text{cm}^2$	$x^2 + y^2 < 361\,\text{cm}^2$
16	Λ vertex: $x^2 + y^2 < 400\,\text{cm}^2$	$x^2 + y^2 < 441\,\text{cm}^2$
17	Λ 3D collinearity $coll_{3D} < 0.3\,\text{rad}$	$coll_{3D} < 0.35\,\text{rad}$
18	Λ 3D collinearity $coll_{3D} < 0.3\,\text{rad}$	$coll_{3D} < 0.25\,\text{rad}$
19	Λ 2D collinearity: $\cos(coll_{2D}) > 0.995$	$\cos(coll_{2D}) > 0.99$
20	Λ 2D collinearity: $\cos(coll_{2D}) > 0.995$	$\cos(coll_{2D}) > 0.999$
21	Λ tracks:$DCA < 0.4\,\text{cm}$	DCA$< 0.3\,\text{cm}$
22	Λ tracks:$DCA < 0.4\,\text{cm}$	DCA$< 0.5\,\text{cm}$
23	Λ vertex: $\chi^2 < 5$	$\chi^2 < 4$
24	Λ 2D distance to beamspot: $d > 0.2\,\text{cm}$	$d > 0.15\,\text{cm}$
25	Λ 2D distance to beamspot: $d > 0.2\,\text{cm}$	$d > 0.25\,\text{cm}$
26	p_T of π, p from $\Lambda > 0.15\,\text{GeV}$	$p_T > 0.175\,\text{GeV}$
27	$\lvert\eta\rvert$ of π, p from $\Lambda < 1.75$	$\lvert\eta\rvert < 1.6$
28	Λ: $\lvert\eta\rvert < 1.6$	$\lvert\eta\rvert < 1.5$
29	Λ: $\lvert\eta\rvert < 1.6$	$\lvert\eta\rvert < 1.75$
30	K^0_s exclusion for $\Lambda : M(\pi\pi) < 0.47\,\text{GeV}$	$M(\pi\pi) < 0.48\,\text{GeV}$
31	K^0_s exclusion for $\Lambda : M(\pi\pi) < 0.47\,\text{GeV}$	$M(\pi\pi) < 0.46\,\text{GeV}$
32	Conversions: $M(e^+e^-) > 0.05\,\text{GeV}$	$M(e^+e^-) > 0.04\,\text{GeV}$
33	Conversions: $M(e^+e^-) > 0.05\,\text{GeV}$	$M(e^+e^-) > 0.06\,\text{GeV}$
34	Distance from Λ^0 trajectory to X track: $0 < \text{dca} < 2\,\text{cm}$	$0 < \text{dca} < 2.5\,\text{cm}$
35	Distance from Λ^0 trajectory to X track: $0 < \text{dca} < 2\,\text{cm}$	$0 < \text{dca} < 1.5\,\text{cm}$
36	Impact parameter of X track $< 0.4\,\text{cm}$	Imp par $< 0.35\,\text{cm}$
37	Impact parameter of X track $< 0.4\,\text{cm}$	Imp par$< 0.45\,\text{cm}$
38	$p_T(X\text{track}) > 0.15\,\text{GeV}$	$p_T(X) > 0.125\,\text{GeV}$
39	$p_T(X\text{track}) > 0.15\,\text{GeV}$	$pT(X) > 0.175\,\text{GeV}$
40	$\lvert\eta\rvert$ of X track< 1.75	$\lvert\eta\rvert < 1.6$
41	Discriminant cut 0.75	0.70
42	Discriminant cut 0.75	0.80
43	MC used for extraction: DJANGOH	RAPGAP
44	Luminosity	3.5% error

Table 10.1: List of variations of selection cuts used to estimate systematic uncertainty

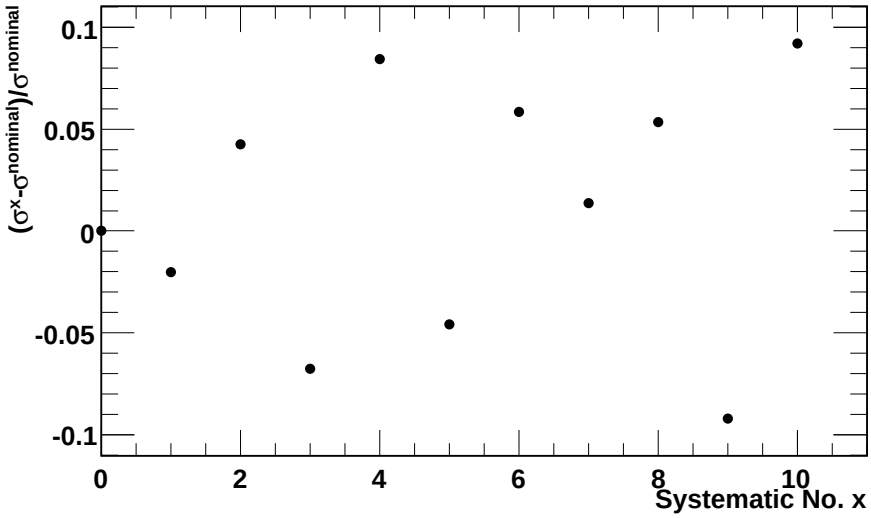


Figure 10.7: Percentage differences in the NLO prediction for the $\Lambda_c^{\pm}$ cross section caused by changing the input parameters. See Table 8.2 for the key.

The baryon-to-meson ratio was measured in the same kinematic region as the $D^{\pm}$ and Λ_c cross sections, thus the D^0 cross section was restricted to this region (i.e. the lower bound in p_T increased to 1.5 GeV). The value obtained for $\mathcal{R}$ was

$$\mathcal{R} = 0.061 \pm 0.027\,(\text{stat.}) \pm 0.029\,(\text{syst.})^{+0.022}_{-0.019}(\text{BR})$$

Values for $\mathcal{R}$ were also calculated from the number of true decays in the Monte Carlo. DJANGOH gave a value of $\mathcal{R} = 0.059$, while RAPGAP gave $\mathcal{R} = 0.060$, both of which are consistent with the measured value within errors.

The systematic and branching-ratio uncertainties are treated as in Section 9.7.

Chapter 11

Conclusions and Outlook

11.1 Conclusions

In this thesis charmed hadron production has been studied in $225\,\mathrm{pb}^{-1}$ of data collected with the ZEUS detector in the HERA-II running period.

Studies of the $D^{*\pm} \to D^0\pi$ channel, in which a clear charm signal had already been obtained, demonstrated that use of the recently-installed microvertex detector in track and vertex reconstruction allowed the displaced secondary vertex due to the D^0 decay to be resolved. The signal-to-background ratio for the mass peak could be improved by cutting on the distance of this vertex from the *ep* interaction point. This approach however required *a priori* knowledge of which tracks belonged on the secondary vertex, and therefore required repeating the vertex fit for each D^0 candidate. In order to be able to profit from the improved resolution from the MVD and at the same time not be overwhelmed by the need for CPU-intensive revertexing of a large combinatorial background, charmed hadron decay modes involving some additional constraint on the particles involved were sought.

This additional constraint was chosen to be the presence of a K^0_s or Λ in the decay chain. These particles travel several centimetres before decaying so are easily reconstructed. The MVD has also improved the efficiency for reconstruction of K^0_s and Λ by allowing them be be reconstructed closer to the *ep* vertex than before the up-

Decay Channel	Integrated Cross Section (nb)
$D^0 \to K^0_s\pi^+\pi^- \to \pi^+\pi^-\pi^+\pi^-$ $(p_T(D^0) > 1.0\,\text{GeV})$	$14.34 \pm 1.41\,(\text{stat.})^{+1.52}_{-2.65}\,(\text{syst.}) \pm 0.94(\text{BR})$
$D^0 \to K^0_s\pi^+\pi^- \to \pi^+\pi^-\pi^+\pi^-$ $(p_T(D^0) > 1.5\,\text{GeV})$	$11.38 \pm 0.95\,(\text{stat.})^{+1.05}_{-1.62}\,(\text{syst.}) \pm 0.75(\text{BR})$
$D^\pm \to K^0_s\pi^\pm \to \pi^+\pi^-\pi^\pm$	$3.90 \pm 0.54\,(\text{stat.})^{+0.97}_{-0.61}\,(\text{syst.}) \pm 0.16(\text{BR})$
$D^\pm_s \to K^0_s K^\pm \to \pi^+\pi^- K^\pm$	$1.86 \pm 0.30\,(\text{stat.})^{+0.43}_{-0.42}\,(\text{syst.}) \pm 0.38(\text{BR})$
$\Lambda^\pm_c \to \Lambda^0\pi^\pm \to \overline{p}\pi^\mp\pi^\pm$	$0.92 \pm 0.39\,(\text{stat.})^{+0.49}_{-0.27}\,(\text{syst.}) \pm 0.26(\text{BR})$

Table 11.1: Summary of integrated cross sections measured in this thesis.

grade, (0.5 cm compared to 3 cm [11]). Cross sections were measured for the channels $D^0 \to K^0_s\pi^+\pi^-$, $D^\pm \to K^0_s\pi^\pm$, $D^\pm_s \to K^0_s K^\pm$ and $\Lambda^\pm_c \to \Lambda^0\pi^\pm$ in the kinematic region $5 < Q^2 < 1000\,\text{GeV}^2$, $0.02 < y < 0.7$, $1.5 < p_T(D, \Lambda_c) < 20.0\,\text{GeV}$, $|\eta(D, \Lambda_c)| < 1.6$. The D^0 cross section was additionally measured down to $p_T(D^0) > 1.0\,\text{GeV}$. In the D^0 channel a secondary vertex is reconstructed and used to improve the signal, however for the other three channels there is only one charged track coming from the charmed hadron decay which makes it impossible to determine the vertex precisely. A discriminant method was developed in order to obtain a signal.

The integrated cross sections are summarised in Table 11.1. Differential cross sections as a function of Q^2, x, $p_T(D, \Lambda_c)$ and $\eta(D, \Lambda_c)$ were measured for each channel except Λ_c where there were insufficient events, and are summarised in Tables 8.3, 9.2, and 9.3. This is the first time these channels have been measured in HERA-II data, and the first time that D_s and Λ_c have been measured in any channel at HERA-II. In addition the kinematic region over which the cross sections are measured extends further in p_T than for previous measurements, which typically use $1.5 < p_T(D^0) < 15\,\text{GeV}$ [61], and $3 < p_T(D^+, D_s) < 20\,\text{GeV}$ [36, 56].

The NLO calculations provided by HVQDIS are in good agreement with the data both for the integrated cross sections, and for the differential cross sections across the whole range measured for each variable.

It is difficult to compare the results of this thesis directly to previous ZEUS results as they are determined in a different kinematic region (for example HERA-I results use

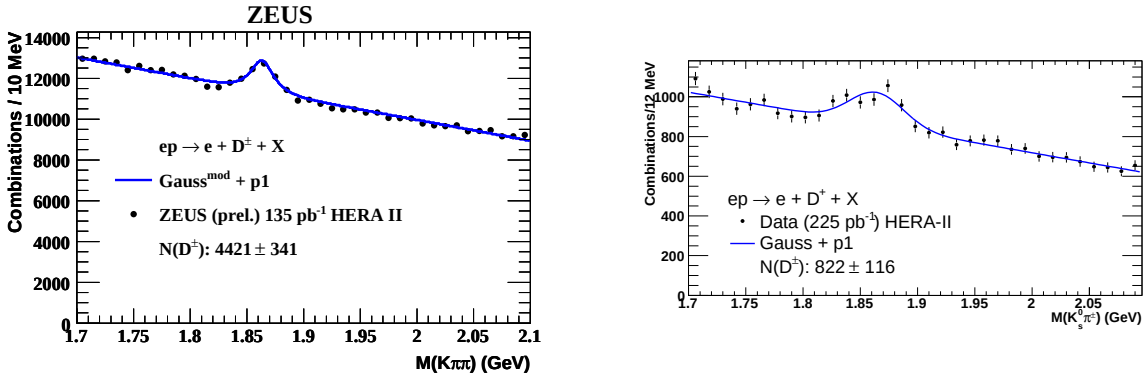


Figure 11.1: (left) $D^{\pm}$ mass spectrum from [56] before decay length significance cut. (right) $D^{\pm}$ mass spectrum from this thesis with lower p_T limit raised to $p_T(D^{\pm}) > 3\,\text{GeV}$

a lower minimum Q^2 and a higher minimum p_T). However a preliminary result for $D^{\pm} \to K^{\mp}\pi^{\pm}\pi^{\pm}$ decays in $135\,\text{pb}^{-1}$ of HERA-II data has recently been released [56], which uses the same kinematic region as this thesis, apart from a increased lower limit for p_T of 3.0 GeV. The differential cross section for p_T can then be directly compared to that obtained in this thesis; this comparison is shown in Figure 9.9. The results for the two channels are in good agreement.

The signal to background ratio for the two results can also be compared, to see if requiring a K^0_s improves it. For a fair comparison we need to consider the preliminary result before the application of a cut on the decay length significance which gives a large improvement in the signal-to-background ratio, and which does not have a direct analogue in our method. The left-hand plot in Figure 11.1 shows the D^+ mass spectrum for the preliminary result before the decay length significance cut. (It is worth remembering that the branching ratio for this channel is 9.51% compared to 1.02% for $D^{\pm} \to K^0_s\pi^{\pm}$.) The background under the peak is approximately 80 000 events, giving a signal/background ratio of $\sim 5.5\%$. The right-hand plot shows the corresponding plot for this analysis, where the lower bound for $p_T(D^+)$ has been increased to 3.0 GeV so as to use the same kinematic region. This has a background of approximately 8500 events under the peak, giving a signal-to-background ratio of $\sim 9.5\%$. Thus requiring a K^0_s tag does seem to increase the signal-to-background ratio, although the peak for the $D^{\pm} \to K^{\mp}\pi^{\pm}\pi^{\pm}$ channel is broader.

The strangeness-suppression factor γ_s, determined from the ratio of the number of charmed mesons to the number of non-charmed mesons, was measured to be

$$\gamma_s = 0.244 \pm 0.054\,(\text{stat.})^{+0.039}_{-0.052}\,(\text{syst.})^{+0.034}_{-0.030}(\text{BR})$$

This is in good agreement with the values previously measured at HERA and elsewhere, as well as those from the DJANGOH and RAPGAP Monte Carlo.

The ratio of the number of charmed baryons (Λ_c) to mesons ($D^{\pm}$, D^0), $\mathcal{R}$ was measured to be

$$\mathcal{R} = 0.061 \pm 0.027\,(\text{stat.}) \pm 0.029\,(\text{syst.})^{+0.022}_{-0.019}(\text{BR})$$

This was in good agreement with DJANGOH and RAPGAP Monte Carlo. The analogous quantity in the strange sector, $\sigma(\overleftrightarrow{\Lambda^0})/\sigma(K^0_s)$ was recently measured at ZEUS [62]. Good agreement was found with ARIADNE Monte Carlo for DIS and direct photoproduction, but an enhancement in the number of baryons in resolved photoproduction was observed in the data. It would be interesting to see whether the same effect occurs in the charm sector.

11.2 Future Work

Although the full HERA-II dataset had been collected at the time of writing of this thesis (with the exception of the low-energy run for the F_L measurement), the full luminosity could not be used in this analysis. This is because the data need to be reprocessed to incorporate calibrations, alignment corrections etc. The alignment of the MVD and the calculation of the beamspot were the main reasons why the data could not be used for this thesis. A further $140\,\text{pb}^{-1}$ of data will therefore become available in the coming months, which would improve the statistical precision of this analysis, were it incorporated. The number of events could also be increased by including photoproduction in addition to DIS.

With the increased numbers of events the differential cross sections could be measured

in more bins, or in the case of Λ_c, be measured. As mentioned in Section 10.1 the $\Lambda_c \to \Lambda^0\pi$ channel offers the possibility of making two interesting measurements – the weak decay-asymmetry parameter of the decay, and the correlation between the lepton beam polarisation and the Λ_c polarisation.

The weak decay-asymmetry parameter of a parity-violating decay is defined as [60]

$$\alpha \equiv \frac{2\mathcal{R}e(A_+^* A_-)}{|A_+|^2 + |A_-|^2} \tag{11.1}$$

where A_+ and A_- are the amplitudes for the parity-even and parity-odd mode. In the case of the decay of a spin-$\frac{1}{2}$ baryon into another spin-$\frac{1}{2}$ baryon and a pseudoscalar meson, e.g. $\Lambda_c^\pm \to \overset{\leftarrow}{\Lambda}{}^0\pi^\pm$ this can be determined experimentally from the angular distribution of the second baryon in the rest frame of the first. For example, in the case of $\Lambda_c^\pm \to \overset{\leftarrow}{\Lambda}{}^0\pi^\pm$, θ is the angle of the Λ^0 in the Λ_c rest frame, so

$$\frac{\mathrm{d}N}{\mathrm{d}\cos(\theta)} = \frac{1}{2}(1 + P\alpha\cos(\theta)) \tag{11.2}$$

where P is the polarisation of the Λ^0 along the z direction. Since $\overset{\leftarrow}{\Lambda}{}^0 \to \overset{\leftarrow}{p}\pi^\pm$ is the same type of decay the above expression can be generalised to

$$\frac{\mathrm{d}N}{\mathrm{d}\cos(\theta)} = \frac{1}{2}(1 + \alpha_{\Lambda_c}\alpha_\Lambda\cos(\theta)) \tag{11.3}$$

where α_{Λ_c} and α_Λ are the decay-asymmetry parameters for the respective decays, and θ is now the helicity angle of the proton, and it is assumed the initial Λ_c is unpolarised. Using the measured value for α_Λ allows α_{Λ_c} to be extracted from the slope of the angular distribution.

The most recent Review of Particle Physics from the Particle Data Group [1] uses only four measurements to determine the world-average value for α_{Λ_c}. Some of these have a similar number of Λ_c's to that reconstructed in this thesis (although their backgrounds are much lower), so it should be feasible for a measurement of the decay-asymmetry parameter with HERA-II data to contribute to the world average.

In addition, since the lepton beam at HERA has been longitudinally polarised since the upgrade it would also be possible to investigate whether there is any correlation between the lepton beam polarisation and the Λ_c polarisation. The Λ_c is arguably a better choice than Λ^0 for this sort of polarisation measurement at HERA-II since there are a number of possible sources for Λ^0 which can dilute the polarisation transfer, but Λ_c's at ZEUS are produced only in the hard interaction (ignoring the contributions from beauty decays or other heavier charmed baryons, which should be small), therefore any correlation with the lepton polarisation should be stronger.

One final extension which could be contemplated to the work presented in this thesis is the calculation of the charm structure function $F_2^{c\bar{c}}$. This requires the measured cross sections to be extrapolated to the full kinematic phase space. Since charm production at ZEUS is dominated by boson–gluon fusion, $F_2^{c\bar{c}}$ provides information on the gluon density of the proton, and can therefore be used as input for fits to determine the proton PDFs.

Appendix A

Additional Plots

A.1 D^0 Systematics Plots

Figures A.1 – A.4 show the effects of the systematic checks in each bin of the D^0 differential cross sections.

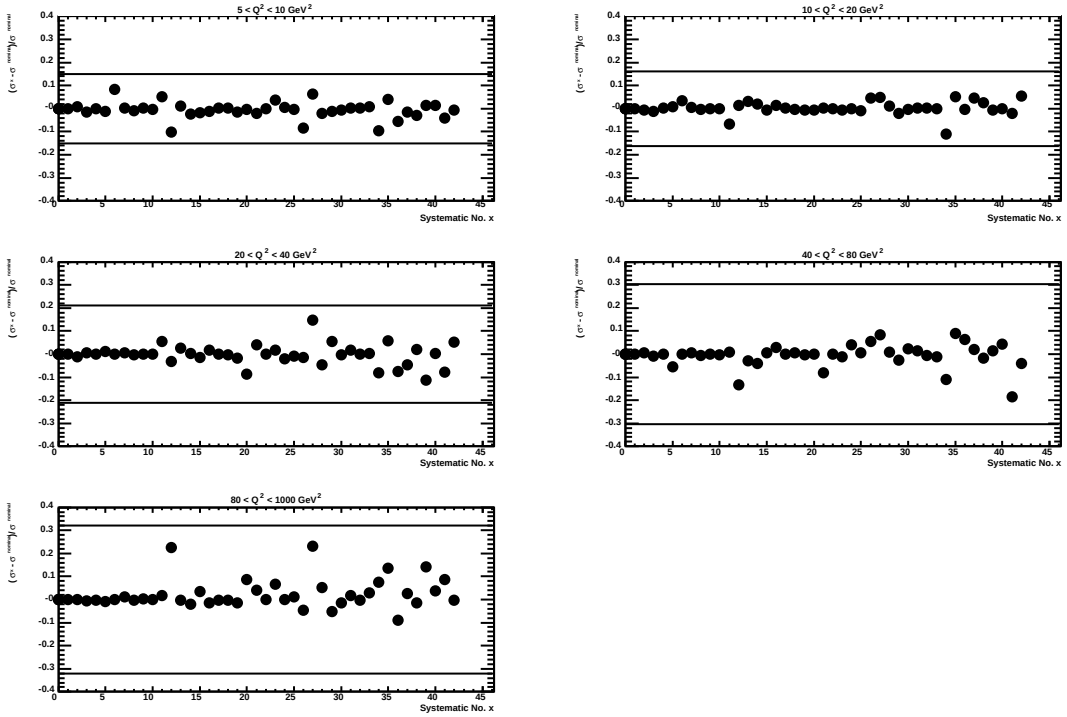


Figure A.1: Percentage differences in the D^0 cross section in bins of Q^2 resulting from each systematic check (see Table 8.1 for the key). The horizontal lines correspond to the statistical error on the nominal cross section.

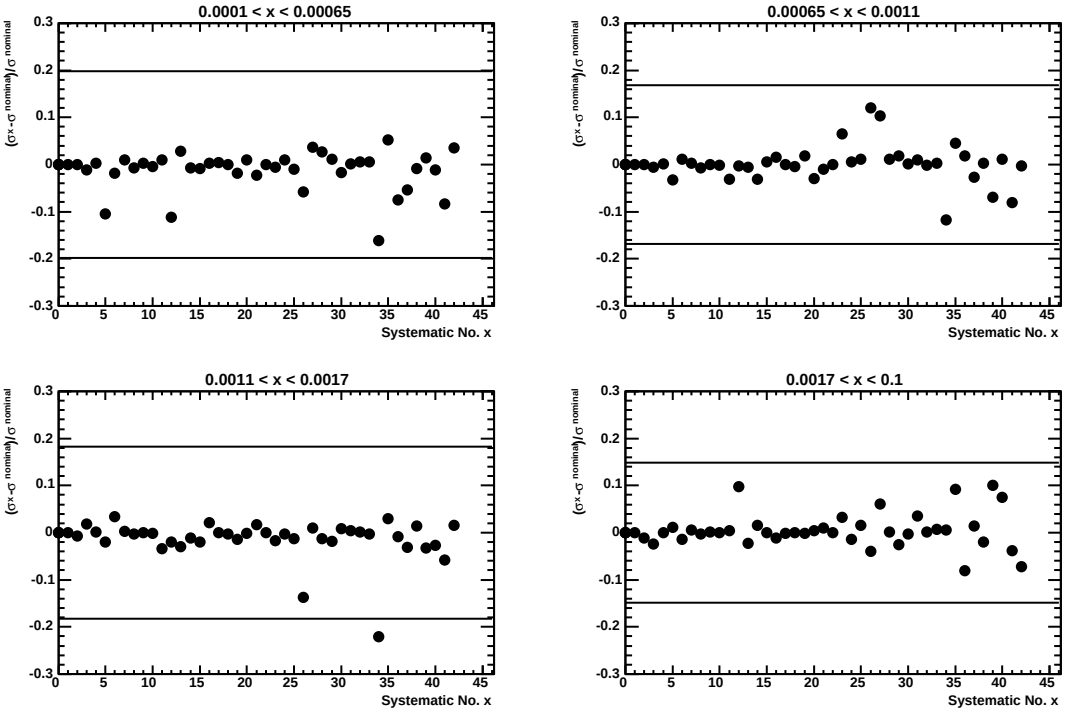


Figure A.2: Percentage differences in the D^0 cross section in bins of x resulting from each systematic check (see Table 8.1 for the key). The horizontal lines correspond to the statistical error on the nominal cross section.

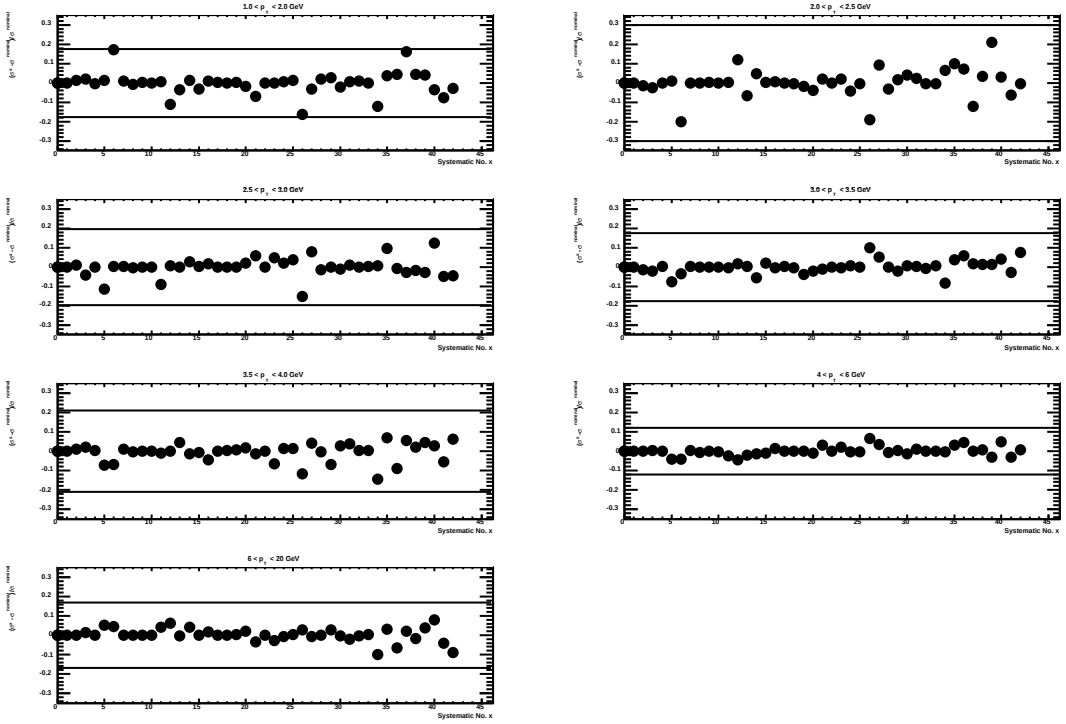


Figure A.3: Percentage differences in the D^0 cross section in bins of $p_T(D^0)$ resulting from each systematic check (see Table 8.1 for the key). The horizontal lines correspond to the statistical error on the nominal cross section.

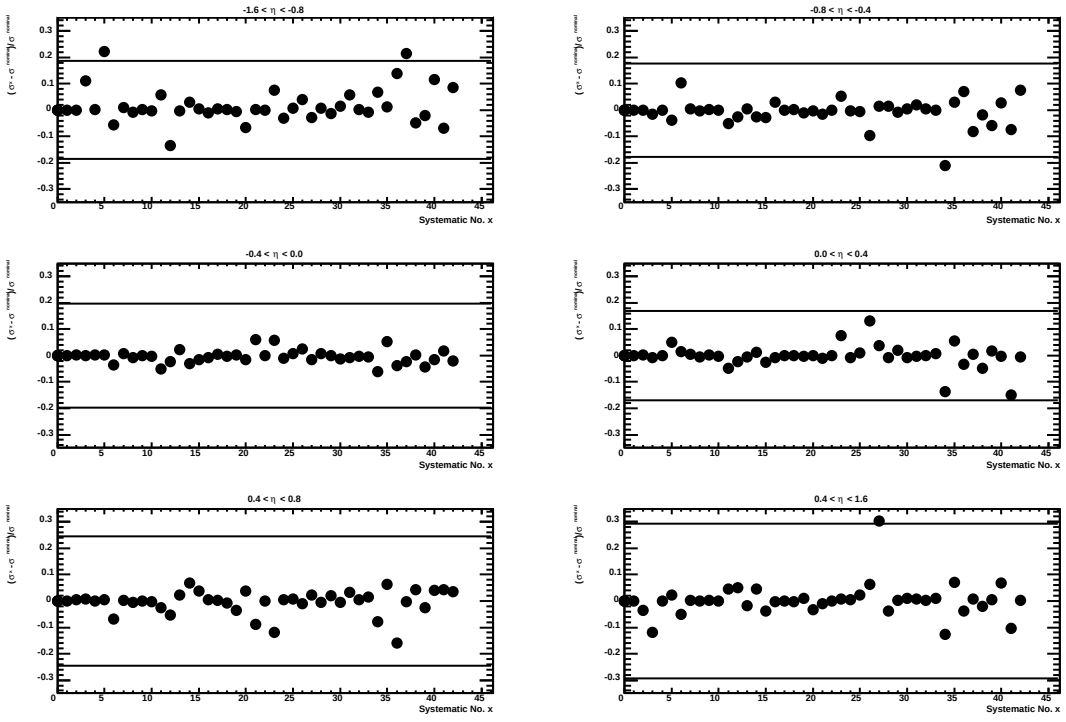


Figure A.4: Percentage differences in the D^0 cross section in bins of $\eta(D^0)$ resulting from each systematic check (see Table 8.1 for the key). The horizontal lines correspond to the statistical error on the nominal cross section.

A.2 $D \to K^0_s X$ Acceptance Plots

Figures A.5 – A.8 show the efficiency, purity and acceptance in the bins used for the differential cross sections for the D^+. Figures A.9 – A.12 show the corresponding quantities for the D_s.

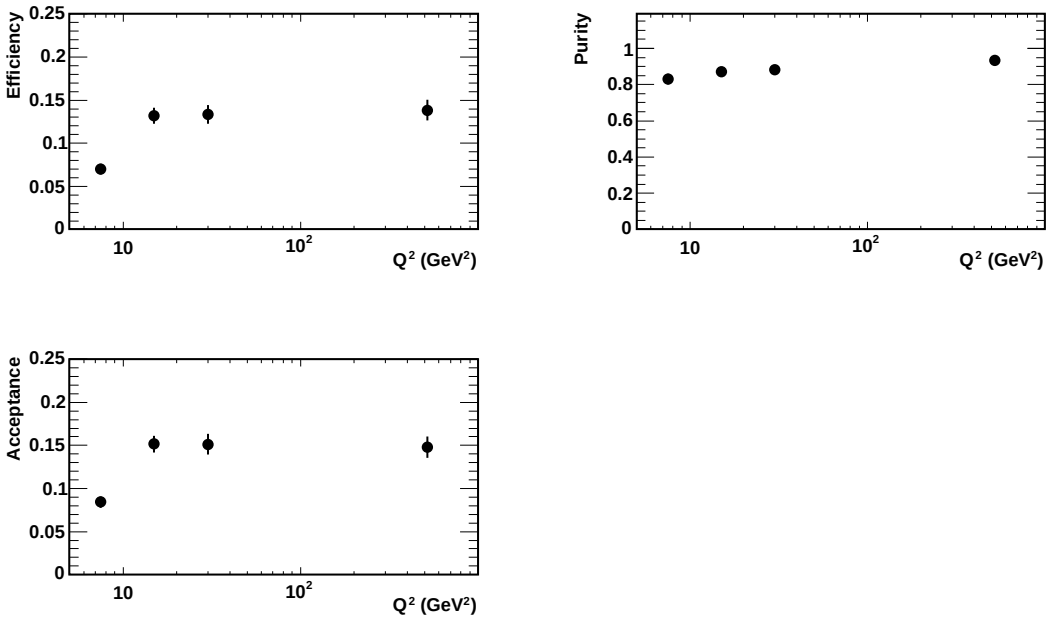


Figure A.5: Plots showing the efficiency, purity and acceptance for reconstructing $D^+ \to K^0_s \pi^+$ in bins of Q^2

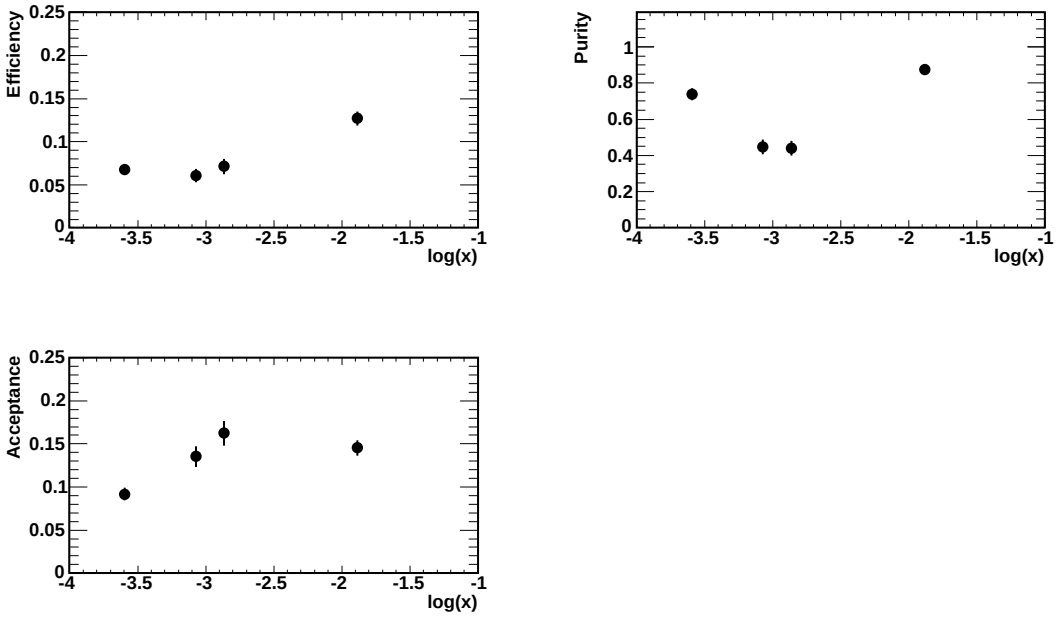


Figure A.6: Plots showing the efficiency, purity and acceptance for reconstructing $D^+ \to K^0_s \pi^+$ in bins of x

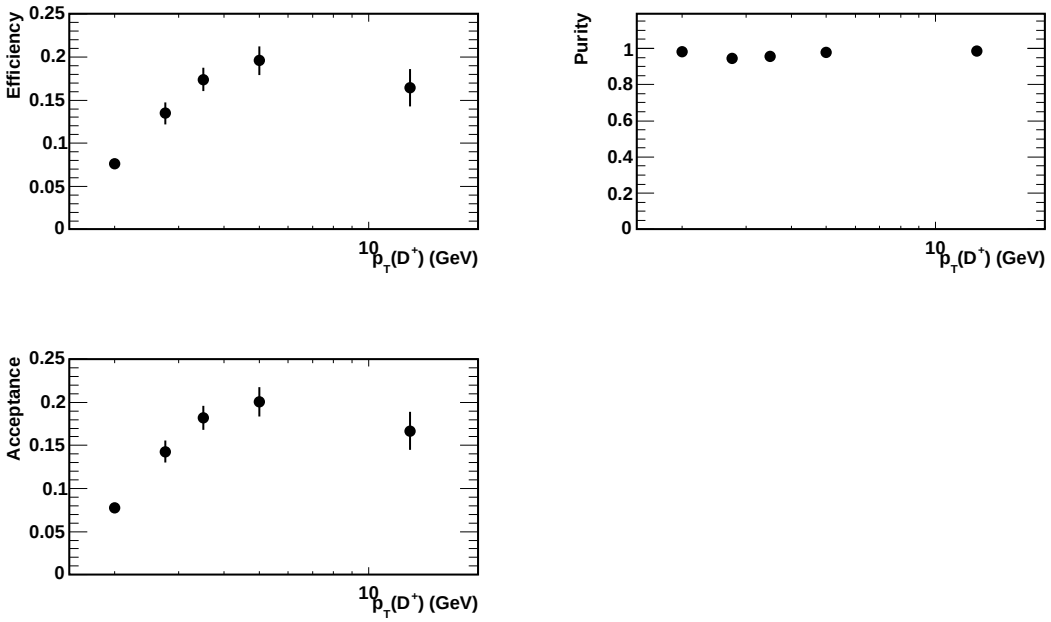


Figure A.7: Plots showing the efficiency, purity and acceptance for reconstructing $D^+ \to K^0_s \pi^+$ in bins of p_T

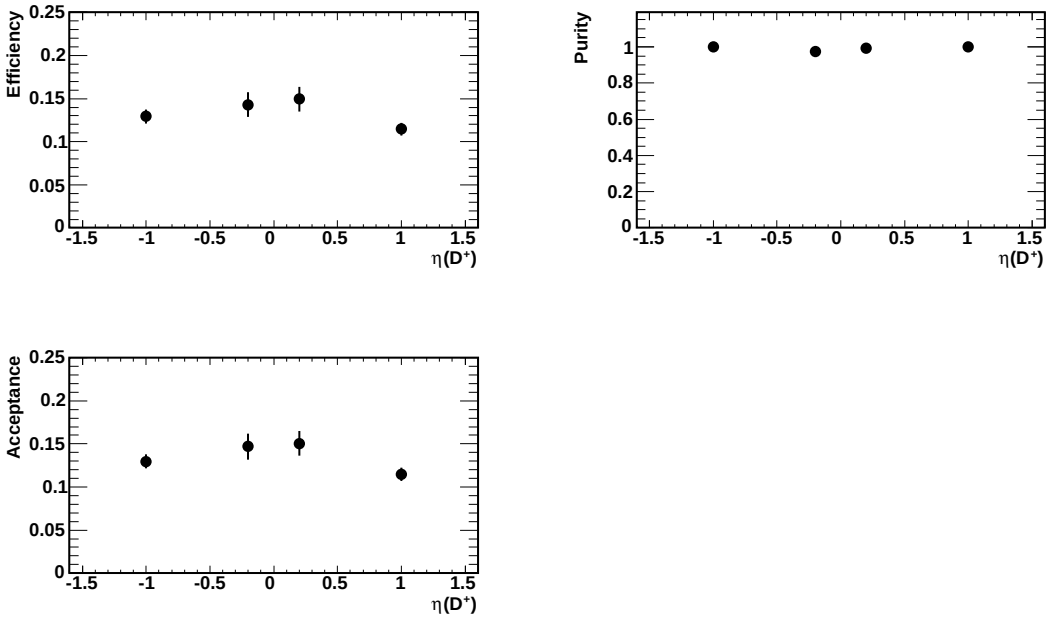


Figure A.8: Plots showing the efficiency, purity and acceptance for reconstructing $D^+ \to K^0_s \pi^+$ in bins of η

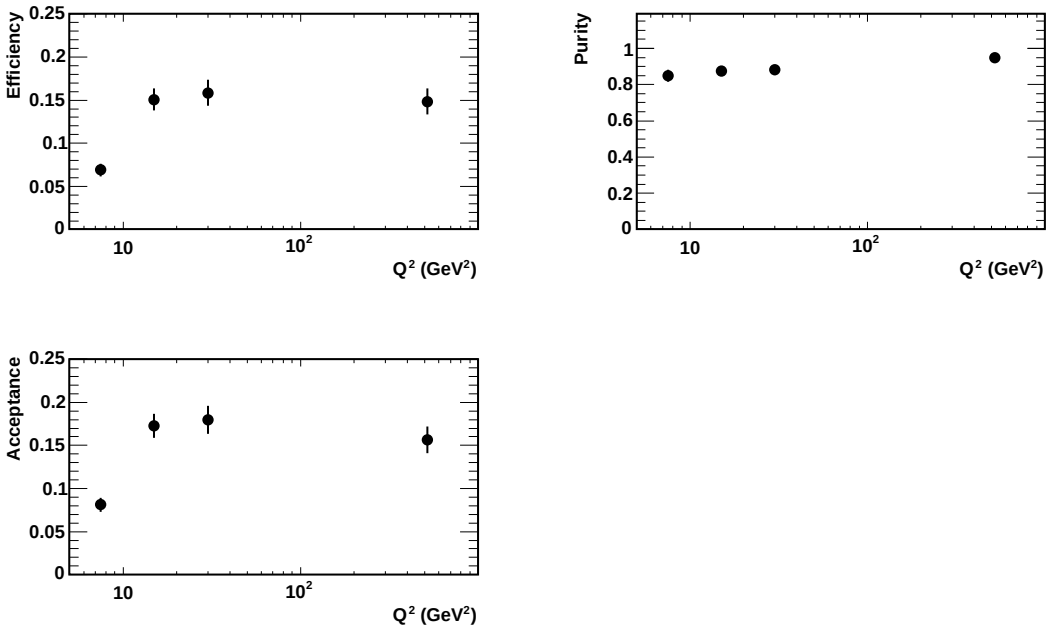


Figure A.9: Plots showing the efficiency, purity and acceptance for reconstructing $D^+_s \to K^0_s K^+$ in bins of Q^2

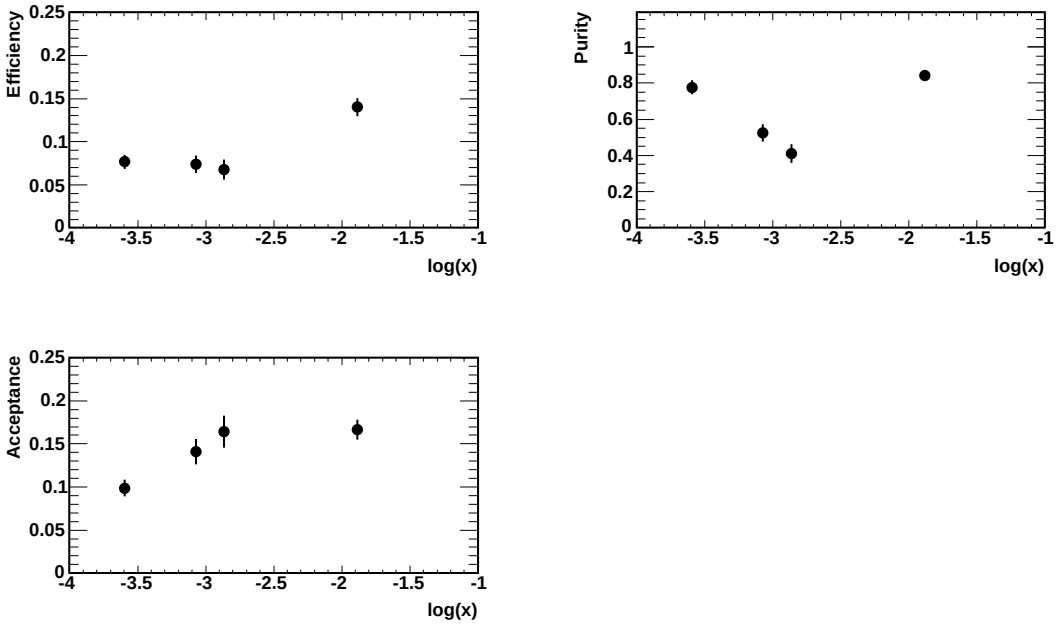


Figure A.10: Plots showing the efficiency, purity and acceptance for reconstructing $D^+_s \to K^0_s K^+$ in bins of x

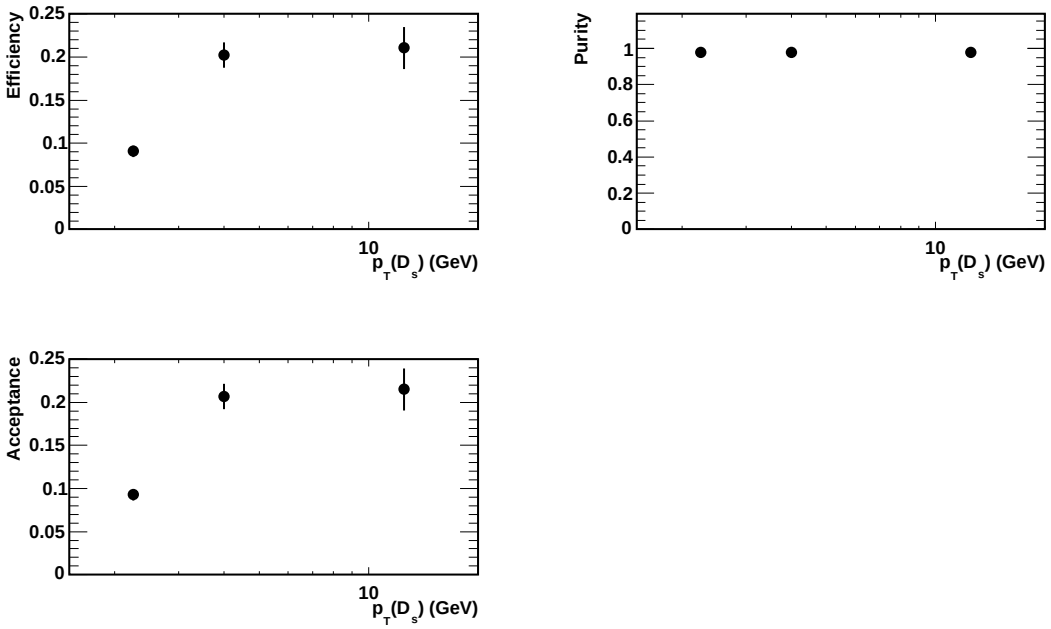


Figure A.11: Plots showing the efficiency, purity and acceptance for reconstructing $D_s^+ \to K_s^0 K^+$ in bins of p_T

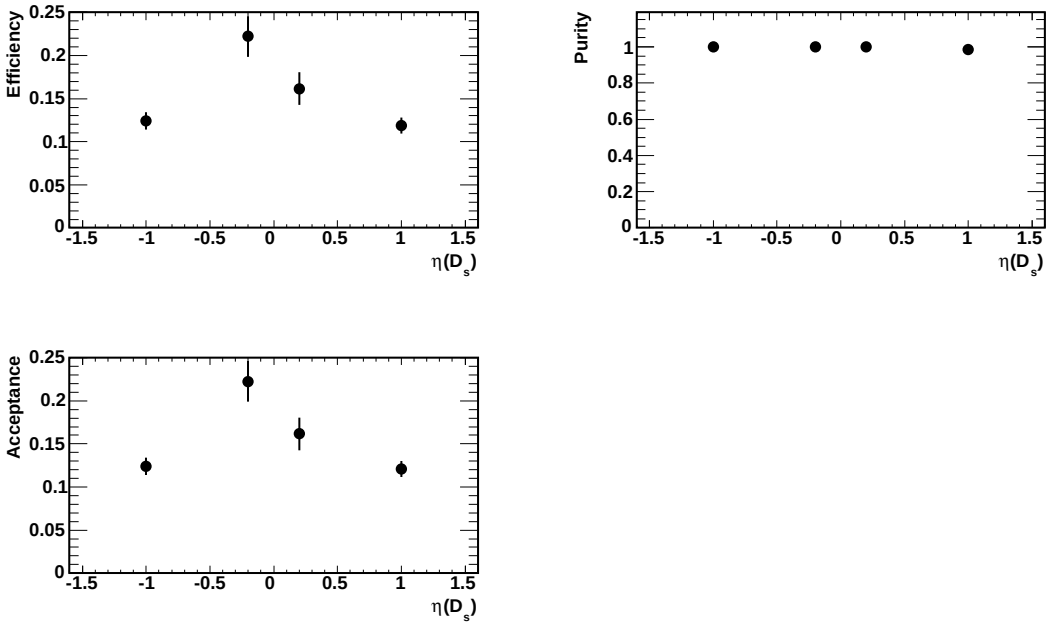


Figure A.12: Plots showing the efficiency, purity and acceptance for reconstructing $D_s^+ \to K_s^0 K^+$ in bins of η

A.3 $D \to K^0_s X$ Systematics Plots

Figures A.13 – A.17 show the effects of the systematic checks in each bin of the D^+ differential cross sections. Figures A.16 – A.20 show the same for the D_s.

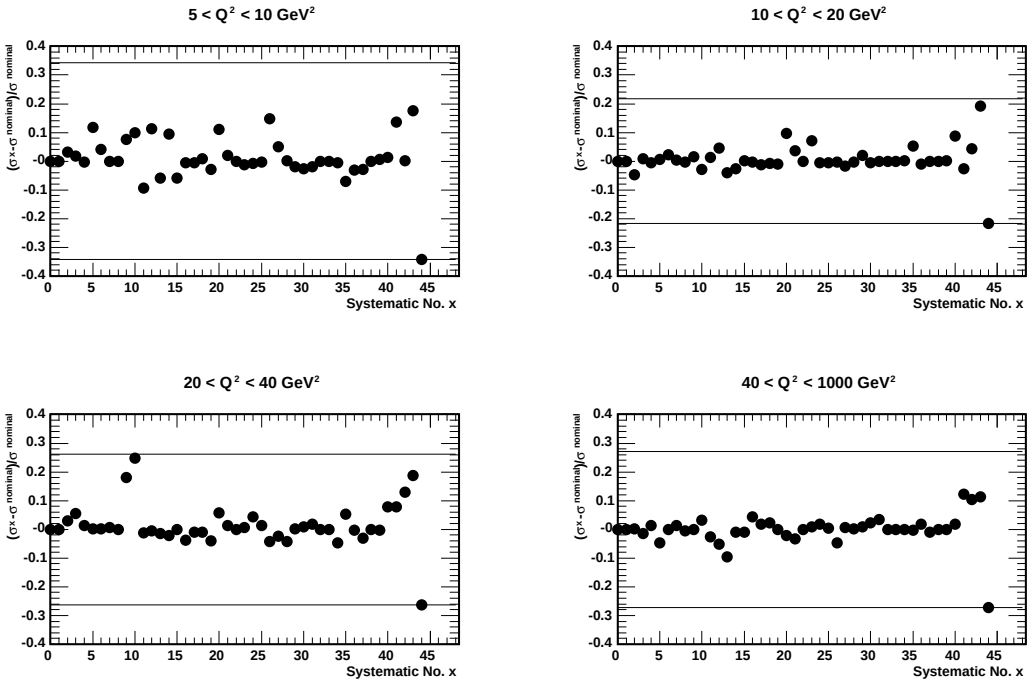


Figure A.13: Percentage differences in the D^+ cross section in bins of Q^2 resulting from each systematic check (see Table 9.1 for the key). The horizontal lines correspond to the statistical error on the nominal cross section.

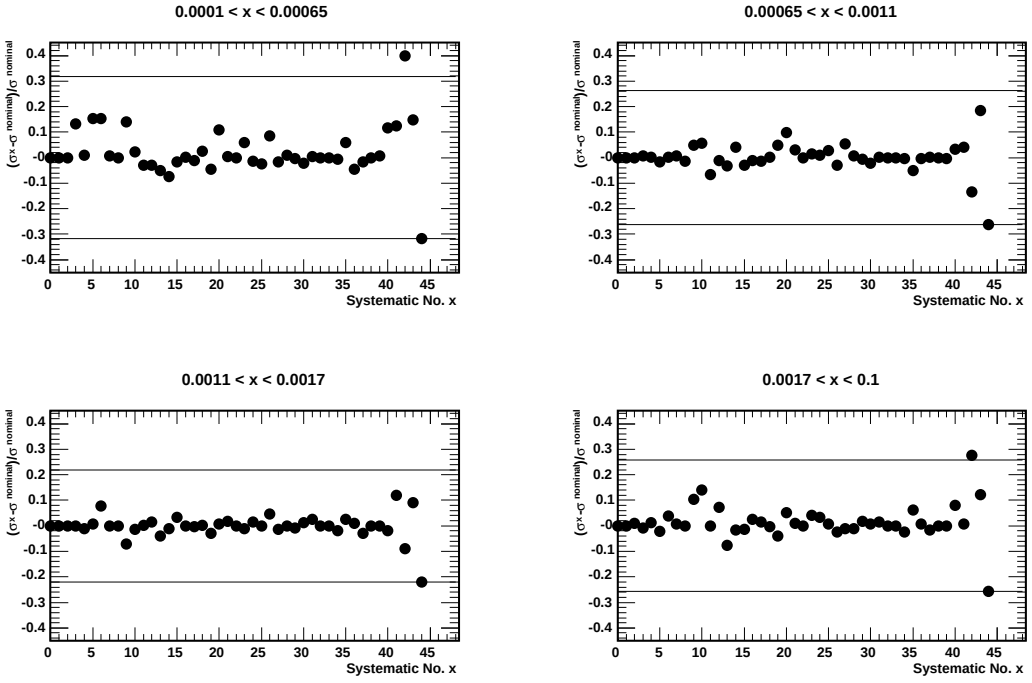


Figure A.14: Percentage differences in the D^+ cross section in bins of x resulting from each systematic check (see Table 9.1 for the key). The horizontal lines correspond to the statistical error on the nominal cross section.

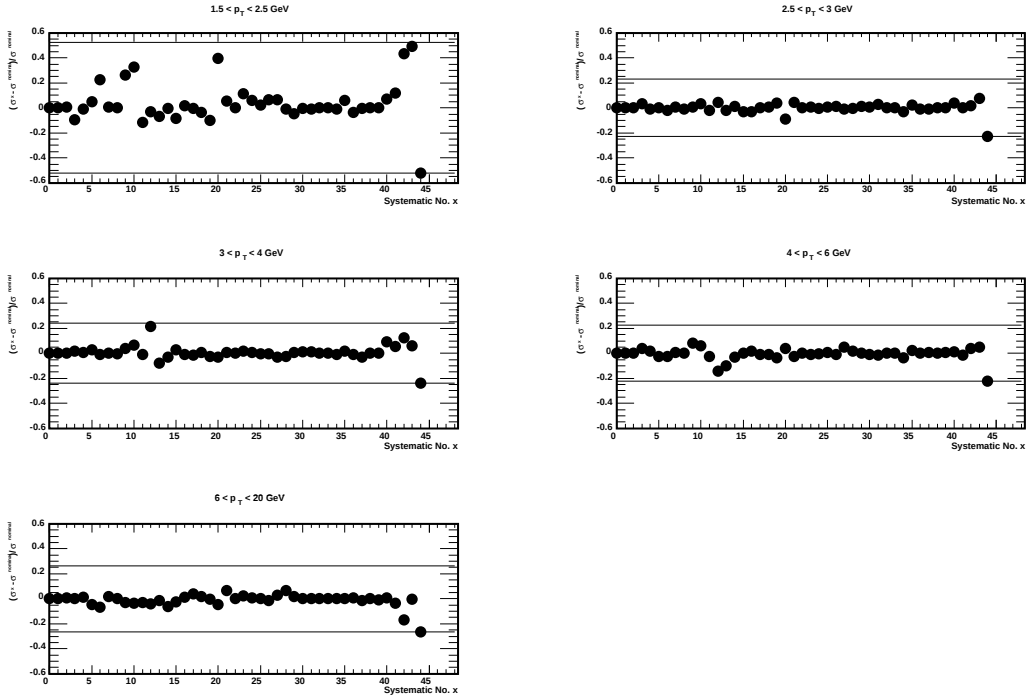


Figure A.15: Percentage differences in the D^+ cross section in bins of $p_T(D^+)$ resulting from each systematic check (see Table 9.1 for the key). The horizontal lines correspond to the statistical error on the nominal cross section.

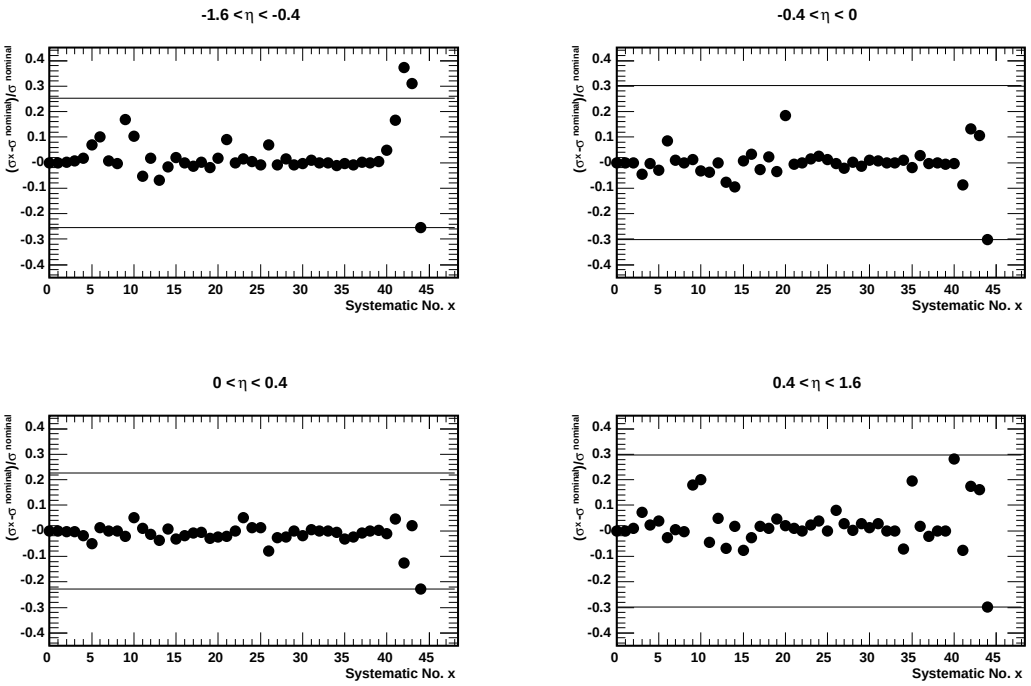


Figure A.16: Percentage differences in the D^+ cross section in bins of $\eta(D^+)$ resulting from each systematic check (see Table 9.1 for the key). The horizontal lines correspond to the statistical error on the nominal cross section.

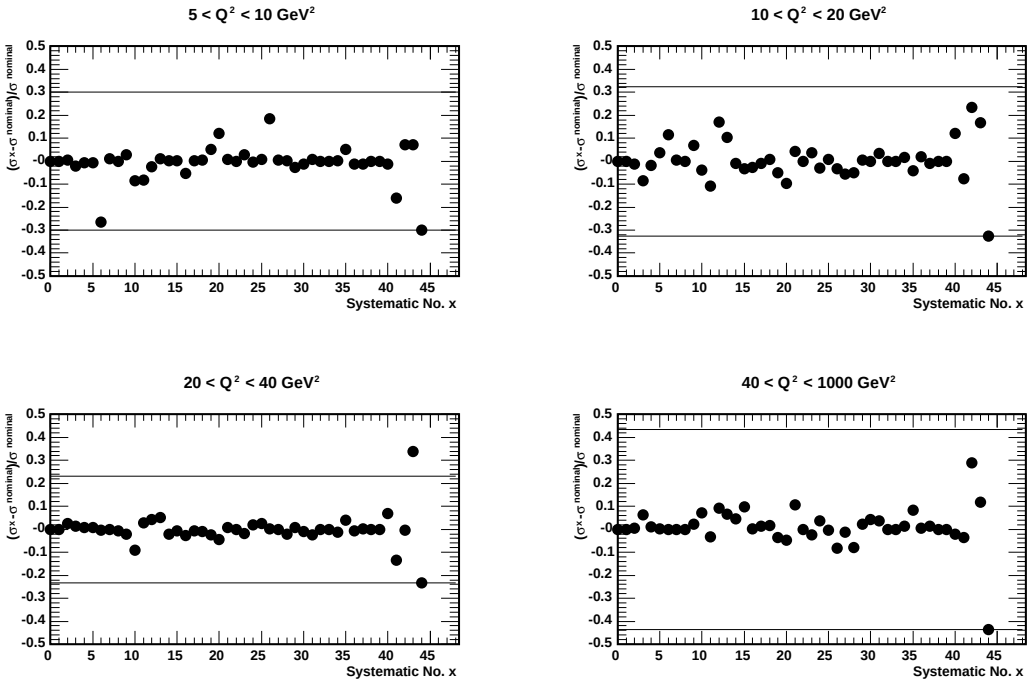


Figure A.17: Percentage differences in the D_s cross section in bins of Q^2 resulting from each systematic check (see Table 9.1 for the key). The horizontal lines correspond to the statistical error on the nominal cross section.

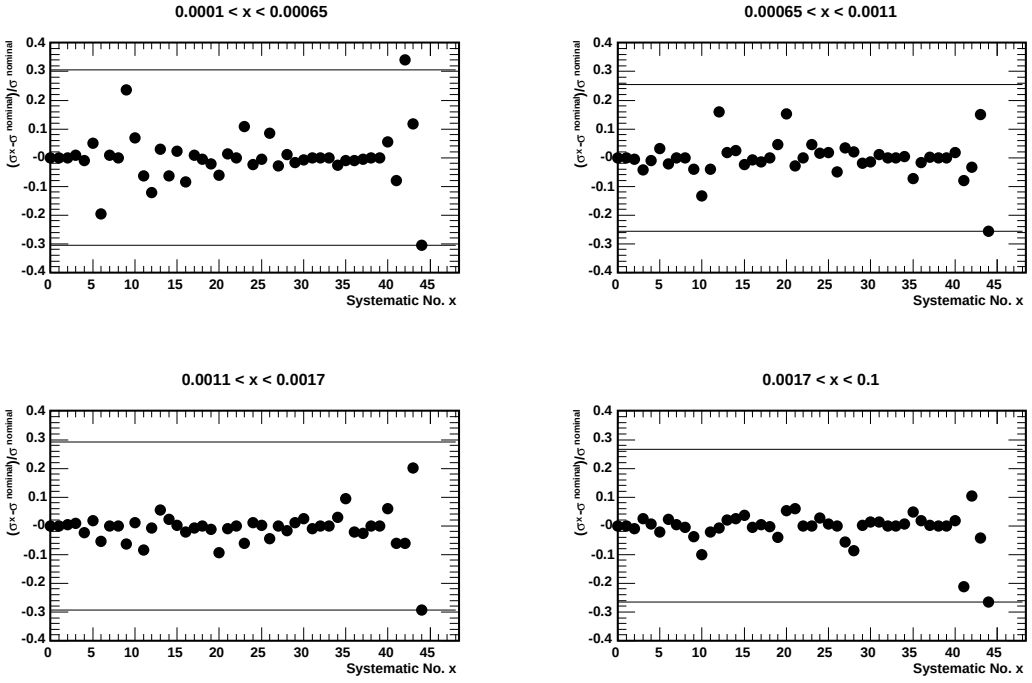


Figure A.18: Percentage differences in the D_s cross section in bins of x resulting from each systematic check (see Table 9.1 for the key). The horizontal lines correspond to the statistical error on the nominal cross section.

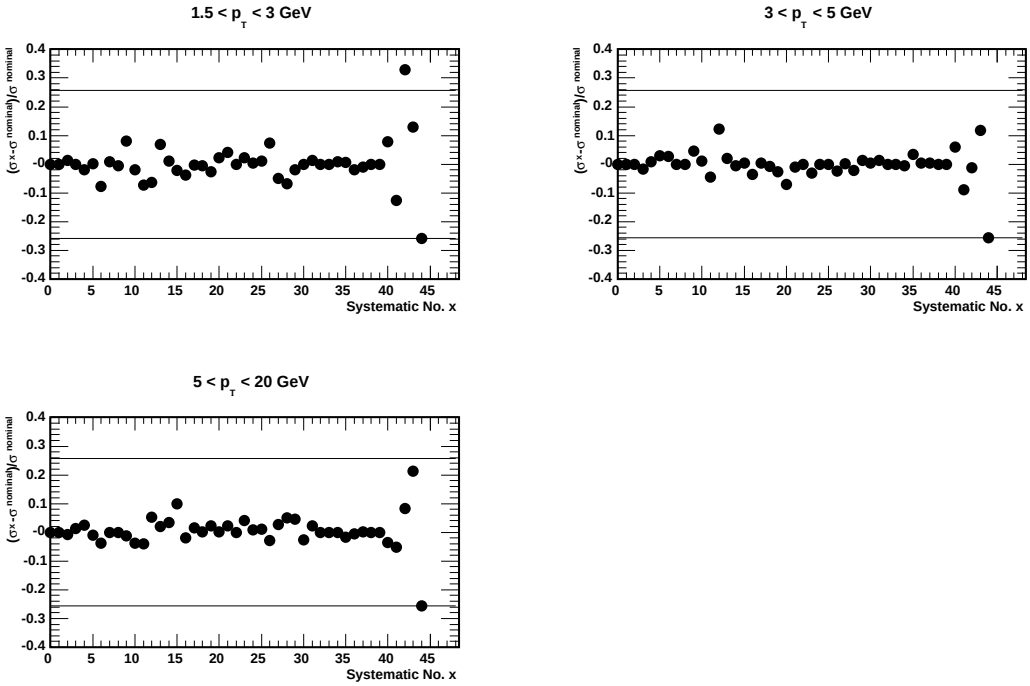


Figure A.19: Percentage differences in the D_s cross section in bins of $p_T(D_s)$ resulting from each systematic check (see Table 9.1 for the key). The horizontal lines correspond to the statistical error on the nominal cross section.

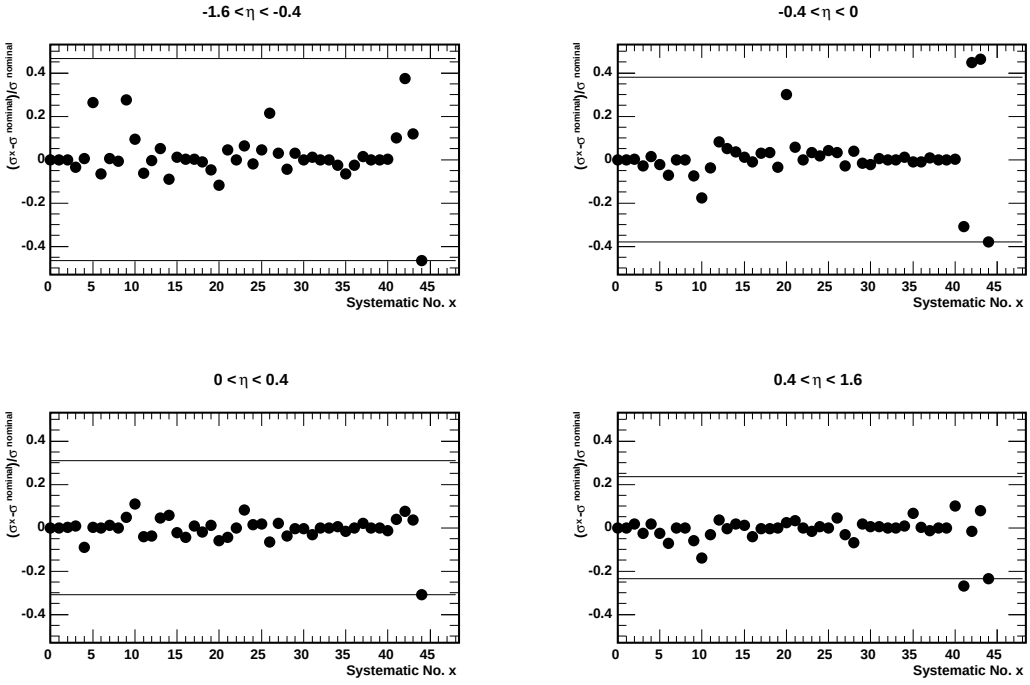


Figure A.20: Percentage differences in the D_s cross section in bins of $\eta(D_s)$ resulting from each systematic check (see Table 9.1 for the key). The horizontal lines correspond to the statistical error on the nominal cross section.

References

[1] Particle Data Group, W.-M. Yao et al., J. Phys. **G 33**, 1 (2006).

[2] G.A. Voss and B.H. Wiik, Ann. Rev. Nucl. Part. Sci. **44**, 413 (1994).

[3] H1 Coll., I. Abt et al., Nucl. Inst. Meth. **A 386**, 310 (1997).

[4] ZEUS Coll., U. Holm (ed.), *The ZEUS Detector*. Status Report (unpublished), DESY (1993), available on `http://www-zeus.desy.de/bluebook/bluebook.html`.

[5] K. Ackerstaff et al., Nucl. Inst. Meth. **A 417**, 230 (1998).

[6] HERA-B Coll., *HERA–B: An Experiment to Study CP Violation in the B System Using an Internal Target at the HERA Proton Ring*, Design Report DESY-PRC 95/01, DESY, 1995.

[7] A.A. Sokolov and I.M. Ternov, Sov. Phys. Dokl. **8**, 1203 (1964).

[8] G.Z.M. Berglund, *Spin-Orbit Maps and Electron Spin Dynamics for the Luminosity Upgrade Project at HERA*. Ph.D. Thesis, Royal Institute of Technology, Stockholm, Sweden, Report DESY-THESIS-2001-044, 2001.

[9] N. Harnew et al., Nucl. Inst. Meth. **A 279**, 290 (1989);
B. Foster et al., Nucl. Phys. Proc. Suppl. **B 32**, 181 (1993);
B. Foster et al., Nucl. Inst. Meth. **A 338**, 254 (1994).

[10] R. Hall-Wilton et al., *The CTD Tracking Resolution* (unpublished). ZEUS-99-024, internal ZEUS-note, 1999.

[11] E. Maddox, *Study of Heavy Quark Production at HERA using the ZEUS Microvertex Detector*. Ph.D. Thesis, Universiteit van Amsterdam, 2004.

[12] E.N. Koffeman, for the ZEUS MVD group, Nucl. Inst. Meth. **A 453**, 89 (2000); D. Dannheim et al., Nucl. Inst. Meth. **A 505**, 663 (2003).

[13] U. Kotz et al., Nucl. Inst. Meth. **A 235**, 481 (1985).

[14] M. Derrick et al., Nucl. Inst. Meth. **A 309**, 77 (1991);
A. Andresen et al., Nucl. Inst. Meth. **A 309**, 101 (1991);
A. Caldwell et al., Nucl. Inst. Meth. **A 321**, 356 (1992);
A. Bernstein et al., Nucl. Inst. Meth. **A 336**, 23 (1993).

[15] H. Bethe and W. Heitler, Proc. Roy. Soc. Lond. **A 146**, 83 (1934).

[16] ZEUS Coll., R. Carlin et al., Nucl. Inst. Meth. **A 379**, 542 (1996).

[17] S.M. Fisher and P. Palazzi, *ADAMO Reference Manual – Version 3.3*. CERN, 1993, available on `http://adamo.web.cern.ch/Adamo/refmanual/Document.html`.

[18] P.D. Allfrey et al., *The design and performance of the ZEUS Global Tracking Trigger* (unpublished). ZEUS-07-001, internal ZEUS Note. Subm. to NIM A., 2007.

[19] A. Bodek et al., Phys. Rev. Lett. **30**, 1087 (1973).

[20] J.D. Bjorken, Phys. Rev. **179**, 1547 (1969).

[21] E.D. Bloom et al., Phys. Rev. Lett. **23**, 930 (1969).

[22] R.P. Feynman, Phys. Rev. Lett. **23**, 1415 (1969).

[23] C.G. Callan and D.J. Gross, Phys. Rev. Lett. **22**, 156 (1969).

[24] G. Miller et al., Phys. Rev. **D 5**, 528 (1972).

[25] R. Brandelik et al., Phys. Lett. **B 86**, 243 (1979).

[26] H1 Coll., C. Adloff et al., Z. Phys. **C 72**, 593 (1996).

[27] ZEUS Coll., J. Breitweg et al., Eur. Phys. J. **C 12**, 35 (2000).

[28] OPAL Coll., R. Akers et al., Phys. Lett. **B 353**, 595 (1995).

[29] G.P. Heath, Nucl. Phys. Proc. Suppl. **65**, 225 (1998).

[30] M.A.G. Aivazis et al., Phys. Rev. **D 50**, 3085 (1994);
M.A.G. Aivazis et al., Phys. Rev. **D 50**, 3102 (1994).

[31] R.G. Roberts and R.S. Thorne, Eur. Phys. J. **C 19**, 339 (2001).

[32] R. Devenish and A. Cooper-Sarkar, *Deep Inelastic Scattering*. Oxford University Press, 2003.

[33] C. Peterson et al., Phys. Rev. **D 27**, 105 (1983).

[34] S. Fang and M. Wing, *Charm Fragmentation Function at HERA*, 2007, available on `http://www-zeus.desy.de/physics/hfla/public/PublicPlots/Zeus-prel-07-010/`. ZEUS-prel-07-010.

[35] P. Nason and C. Oleari, Nucl. Phys. **B 565**, 245 (2000).

[36] ZEUS Coll., S. Chekanov et al., Preprint DESY-07-052, 2007. Submitted to JHEP.

[37] ZEUS Coll., S. Chekanov et al., Eur. Phys. J. **C 44**, 351 (2005).

[38] R. Brun et al., GEANT3, Technical Report CERN-DD/EE/84-1, CERN, 1987.

[39] B.W. Harris and J. Smith, Phys. Rev. **D 57**, 2806 (1998).

[40] I. Bloch, *Measurement of Beauty Production from Dimuon Events at HERA / ZEUS*. Ph.D. Thesis, Hamburg University, Report DESY-THESIS-2005-034, 2005.

[41] H. Spiesberger, HERACLES *and* DJANGOH*: Event Generation for ep Interactions at HERA Including Radiative Processes*, 1998, available on `http://www.desy.de/~hspiesb/djangoh.html`.

[42] G. Ingelman, A. Edin and J. Rathsman, Comp. Phys. Comm. **101**, 108 (1997).

[43] H. Spiesberger, *An Event Generator for ep Interactions at HERA Including Radiative Processes (Version 4.6)*, 1996, available on `http://www.desy.de/~hspiesb/heracles.html`.

[44] L. Lönnblad, Comp. Phys. Comm. **71**, 15 (1992).

[45] B. Andersson et al., Phys. Rep. **97**, 31 (1983).

[46] T. Sjöstrand et al., Comp. Phys. Comm. **135**, 238 (2001).

[47] H. Jung, Comp. Phys. Comm. **86**, 147 (1995).

[48] CTEQ Coll., H.L. Lai et al., Eur. Phys. J. **C 12**, 375 (2000).

[49] S. Bentvelsen, J. Engelen and P. Kooijman, *Proc. Workshop on Physics at HERA*, W. Buchmüller and G. Ingelman (eds.), Vol. 1, p. 23. Hamburg, Germany, DESY (1992).

[50] F. Jacquet and A. Blondel, *Proceedings of the Study for an ep Facility for Europe*, U. Amaldi (ed.), p. 391. Hamburg, Germany (1979). Also in preprint DESY 79/48.

[51] B. Straub, *The `em` Electron Finder* (unpublished), 1998, available on `http://www-zeus.desy.de/~straub/ZEUS_ONLY/doc/em.ps`.

[52] G.F. Hartner et al., *VCTRAK(3.07/04): Offline Output Information* (unpublished). ZEUS-97-064, internal ZEUS Note, 1997;
G.F. Hartner, *VCTRAK Briefing: Program and Math* (unpublished). ZEUS-98-058, internal ZEUS Note, 1998;
E. Maddox, *A Kalman Filter Track Fit for the ZEUS Microvertex Detector* (unpublished). ZEUS-03-008, internal ZEUS note, 2003.

[53] R. Frühwirth and A. Strandlie, Comp. Phys. Comm. **120**, 197 (1999).

[54] P. Billoir, R. Frühwirth and M. Regler, Nucl. Inst. Meth. **A 241**, 115 (1985).

[55] DELPHI Coll., P. Abreu et al., Eur. Phys. J. **C 16**, 555 (2000).

[56] D. Nicholass
and J. Loizides, *F^2_{cc} from $D^{\pm}$ Mesons in DIS using 2005 e^-p Data*, 2007, available on
`http://www-zeus.desy.de/physics/hfla/public/PublicPlots/Zeus-prel-07-009/`.
ZEUS-prel-07-010.

[57] ALEPH Coll., A. Heister et al., Phys. Lett. **B 526**, 34 (2002).

[58] ZEUS Coll., J. Breitweg et al., Phys. Lett. **B 481**, 213 (2000).

[59] H1 Coll., A. Aktas et al., Eur. Phys. J. **C 38**, 447 (2005).

[60] FOCUS Coll., J.M. Link et al., Phys. Lett. **B 634**, 165 (2006).

[61] ZEUS Coll., S. Chekanov et al., Phys. Rev. **D 69**, 012004 (2004).

[62] ZEUS Coll., S. Chekanov et al., Eur. Phys. J. **C 51**, 1 (2007).